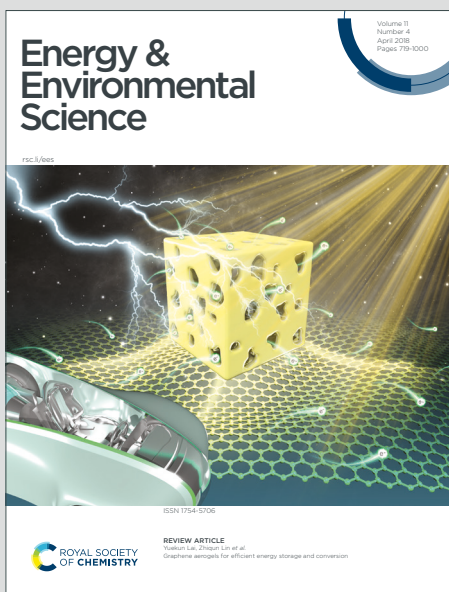


Energy & Environmental Science

Accepted Manuscript

This article can be cited before page numbers have been issued, to do this please use: Z. Guo, A. K. Jena, G. Kim and T. Miyasaka, *Energy Environ. Sci.*, 2022, DOI: 10.1039/D2EE00663D.



This is an Accepted Manuscript, which has been through the Royal Society of Chemistry peer review process and has been accepted for publication.

Accepted Manuscripts are published online shortly after acceptance, before technical editing, formatting and proof reading. Using this free service, authors can make their results available to the community, in citable form, before we publish the edited article. We will replace this Accepted Manuscript with the edited and formatted Advance Article as soon as it is available.

You can find more information about Accepted Manuscripts in the [Information for Authors](#).

Please note that technical editing may introduce minor changes to the text and/or graphics, which may alter content. The journal's standard [Terms & Conditions](#) and the [Ethical guidelines](#) still apply. In no event shall the Royal Society of Chemistry be held responsible for any errors or omissions in this Accepted Manuscript or any consequences arising from the use of any information it contains.

Perovskite solar cells (PSCs) have experienced a high-speed development in the past decade, establishing themselves as a leading photovoltaic technology with high efficiency and low cost. The high open-circuit voltage (V_{oc}) is one of the characteristics that distinguish them from other photovoltaics. PSCs have low V_{oc} loss than other solution-processed photovoltaics such as organic and dye-sensitized solar cells, as well as vacuum-processed CdTe and CIGS solar cells. While in most cases, the V_{oc} of PSCs still has room to improve. Given that the photocurrent is approaching the theoretical limit and the fill factor is often quite high, increasing V_{oc} is crucial for further enhancing the efficiency. Here we provide a comprehensive review of strategies for improving V_{oc} by dividing our discussion into four parts depending on the light absorbers; organic-inorganic hybrid perovskites, all-inorganic perovskites, tin-based perovskites, and bismuth-based perovskites (analogs). We also present a summary with an outlook on how minimizing perovskite film defects and developing more suitable charge transport materials can further increase the V_{oc} and therefore expand the application perspective of PSCs. This review will help the researchers better understand how V_{oc} loss generates and provide suggestions for designing efficient PSCs with improved V_{oc} and efficiency.

High Open-circuit Voltage of Perovskite Solar Cells: A Review

Zhanglin Guo*,¹ Ajay Kumar Jena,¹ Gyu Min Kim,² Tsutomu Miyasaka*,¹

¹ Graduate School of Engineering, Toin University of Yokohama, 1614 Kuroganecho, Aoba, Yokohama, Kanagawa 225-8503, Japan

² Faculty of Food Biotechnology and Chemical Engineering, Hankyong National University, Anseong, Gyeonggi-Do 17579, Republic of Korea

E-mail: guo_zhanglin@outlook.com; miyasaka@toin.ac.jp

Abstract

Perovskite solar cells (PSCs) have made incredibly fast progress in past years, pushing the efficiency approaching 26%, which is comparable to the best silicon solar cells. One of the features of PSCs that make them stand out among all photovoltaics (PVs) is high open-circuit voltage (V_{OC}) although they are made by solution processes. Compared to other solution-processed PVs such as organic photovoltaics and dye-sensitized solar cells, and vacuum-processed PVs like CdTe, CIGS, the loss in V_{OC} caused by non-radiative recombination in the case of PSCs is considerably low, which is even as low as observed for vacuum-processed Si. The defects-tolerance nature of perovskites helps to prevent non-radiative recombination and therefore yields high V_{OC} in PSCs. By comparing the achieved performance with the Shockley-Queisser (S-Q) limits, it can be made out that while the photocurrent of PSCs reaches almost the theoretical limit, there is still room to improve the V_{OC} , especially in the case of all-inorganic and tin-based perovskites. Hence, improving the V_{OC} becomes critical for promoting device efficiency further. In this review paper, we focus our discussion on the recent development of V_{OC} of PSCs by beginning with a theoretical review highlighting the critical role of V_{OC} enhancement and the necessity of non-radiative recombination suppression for device performance improvement. As the recombination both in the bulk of perovskite and on the surface/interfaces with charge transport layers are important, different methods depending on the perovskite composition and the nature of electron transport layer (ETL) and hole transport material (HTM), have been developed to minimize recombination in perovskite and at the interfaces. We provide a comprehensive review of different reported strategies for reducing the undesirable recombination in the perovskite film and at the interfaces, by dividing our discussion into four parts based on the light absorbers; organic-inorganic hybrid perovskites, all-inorganic perovskites, tin-based perovskites, and bismuth-based perovskites (analogs). Finally, a summary with an outlook on how reducing perovskite film defects and developing more suitable charge transport layers can further promote the V_{OC} and expand the practical application perspective of PSCs is presented.

Contents

1	Introduction	4
1.1	Theoretical background of V_{OC}	5
1.2	Defects and non-radiative loss.....	10
1.3	Quantifying non-radiative loss	13
1.4	Defect-tolerance property	14
2	Organic-inorganic hybrid perovskite solar cells	17
2.1	Optimizing hybrid perovskite film preparation.....	18
2.1.1	Anti-solvent method for hybrid perovskites.....	18
2.1.2	Additives to hybrid perovskites.....	19
2.2	Improving ETL and interface	23
2.3	Improving HTM and interface	28
2.3.1	Modification of Spiro-OMeTAD HTM	28
2.3.2	Modification of perovskite/HTM interface	31
3	All-inorganic perovskite solar cells	35
3.1	Reducing bulk recombination.....	36
3.1.1	Controlling $CsPbX_3$ perovskite film growth	36
3.1.2	Metal doping to $CsPbX_3$ perovskite.....	39
3.1.3	Constructing 2D/3D heterostructure	42
3.2	Minimizing perovskite surface and interface recombination.....	45
3.3	Tuning charge transport layers	51
3.3.1	Improving ETL and energy alignment	51

3.3.2 Improving HTM and energy alignment	54
3.3.3 Improving inverted structure CsPbX_3 solar cells.....	57
4 Tin perovskite solar cells.....	58
4.1 Improving tin perovskite film quality	58
4.1.1 Controlling tin perovskite film growth.....	58
4.1.2 Preventing Sn^{2+} oxidation.....	61
4.2 Minimizing interface recombination	64
4.2.1 Tuning energy alignment in inverted structure	64
4.2.2 Tuning energy alignment in normal structure.....	66
5 Bismuth perovskite (analogs) solar cells	69
5.1 Low-dimensional $\text{A}_3\text{Bi}_2\text{X}_9$ solar cells	69
5.2 A_2AgBiX_6 double perovskite solar cells	70
5.3 3D $\text{Ag}_a\text{Bi}_b\text{X}_{a+3b}$ perovskite solar cells	71
5.3.1 Making high-quality $\text{Ag}_a\text{Bi}_b\text{X}_{a+3b}$ film	71
5.3.2 Tuning energy alignment with CTLs.....	72
6 Summary and outlook.....	74
6.1 Current research summary	74
6.2 Future outlook.....	78

1 Introduction

Since the demonstration of the first silicon solar cell, only a limited number of single-junction photovoltaic (PV) technologies could reach power conversion efficiency (PCE) of over 20%.¹ Among these technologies, the halide perovskite solar cells (PSCs) are considered to have the potential to approach the Shockley-Queisser (S-Q) limit of efficiency. Since the first report by Prof. Miyasaka and co-workers,² the PSCs have been attracting extensive attention, which can be witnessed from the numerous publications in this field, and over 15000 citations for the pioneering article. Now, the record efficiency of PSCs (25.7%, certified by NREL) is approaching that of the best silicon solar cells (26.7%). The noteworthy fact is that a PCE of above 25% was achieved only in ~10 years while silicon solar cells took about four decades to reach the PCE above 26%.¹ On one hand, this amazing progress of PSCs is a result of the “magic” properties of perovskites, such as high light absorption coefficient ($\sim 10^5 \text{ cm}^{-1}$) backed by direct bandgap, easy bandgap tunability, long carrier diffusion lengths even in polycrystalline films ($>1 \mu\text{m}$), and the generation of free charges by photoexcitation, defect-tolerance nature, etc.³ On the other hand, it should be attributed to the lessons learned from other solution-processable photovoltaic technologies including dye-sensitized solar cell (DSSC) and organic photovoltaics (OPV). As a result of their impressive development, the perovskite-based single junction or perovskite-involved tandem cells such as perovskite/Si and perovskite/perovskite are regarded to have a great possibility to be commercialized. Several companies such as Oxford PV (UK), Microquanta (China), UtmoLight (China), Saule Tech (Poland), and Toshiba (Japan), with the support of huge investment, are already on their way to exploring commercialization by manufacturing and testing large-area PSC single-junction (rigid or flexible) or perovskite/Si tandem photovoltaic panels.

The PSCs have several attributes that give them an edge over other PVs. One of such traits of PSCs is their relatively high open-circuit voltage (V_{OC}) achieved despite the solution process. Like in most cases of solution-processed materials, it is anticipated that perovskites prepared by the solution processes should end up with a large number of defects, structural disorders, and chemical inhomogeneity. And, these defects must cause a great loss in performance, apparently through a significant drop in V_{OC} and FF. However, in reality, V_{OC} demonstrated by PSCs, especially hybrid perovskites, are reaching almost the theoretical limit. For instance, a PSC working with a PCE of 25.2% shows a V_{OC} of 1.193 V for a perovskite absorber with a bandgap of 1.56 eV, showing only 0.367 eV loss from the bandgap and only 0.034 V loss from the radiative V_{OC} limit (i.e. S-Q limit) of 1.270 V.⁴ Moreover, the cells, when measured without an aperture mask at open circuit condition for about 15 seconds, show a steady state maximum V_{OC} of 1.225 V, against radiative V_{OC} limit of 1.227 V. As another example, Kirchartz et al. promoted the V_{OC} to 1.26 V for a 1.60 eV perovskite-based solar cell, by suppressing the defects in both perovskite bulk and surface.⁵ Our group reported a hybrid perovskite cell with a 1.51 eV bandgap yielding V_{OC} of 1.19 V and energy loss as small as 0.32 eV.⁶ In general, in terms of V_{OC} loss, in comparison to other PVs, PSCs (hybrid perovskites) stand matching with Si (0.3-0.4 eV loss from E_g) and far ahead of solution-processed PVs like OPV (about 0.6 eV loss) and DSSC (about 0.7 eV loss). There is increasing evidence that such high V_{OC} , especially in the case of hybrid perovskites, results from the “defect-tolerance” nature of perovskites, which is discussed in

the latter part of this section. It must be noted that the “defect-tolerance” property, which essentially refers to the crystal defects or chemical inhomogeneity, is intrinsic property but E_{loss} in a device can also come from imperfections in the device; poor perovskite film, or the carrier transport layers (CTLs) in contact, or physical and electrical imperfections at the interfaces. Hence, immense efforts have been made to improve the quality of the films and interfaces to eventually minimize energy loss and achieve high V_{OC} . All the major methods/approaches toward this goal of achieving high V_{OC} are discussed in detail in the sections of organic-inorganic hybrid perovskites, all-inorganic perovskites, tin perovskites, and bismuth perovskites (analog).

1.1 Theoretical background of V_{OC}

Although the PCE of PSCs has surpassed 25%, the record efficiency is still behind the theoretical limit (33% for a 1.4 eV perovskite) estimated by the Shockley-Queisser (S-Q) theory (also called detailed balance limit of efficiency) for single-junction solar cells.⁷ As photovoltaic panels of the entire PV system constitute only a small portion of the total cost, reducing the cost of solar cells has little impact on the installation cost while raising the efficiency has a tremendous impact on the cost per kilowatt-hour.⁸ PCE of solar cells is determined by the recombination process of photoexcited charge carriers. The charge carriers can recombine radiatively or non-radiatively, where the energy of recombined excess electrons and holes is eventually transferred as either a photon or phonon, respectively.⁹ In the S-Q theory, an ideal case is assumed that the only recombination mechanism in a solar cell is radiative, without any non-radiative recombination. It is this radiative recombination that determines the detailed balance limit for efficiency. The theoretical limitations of the efficiency of solar cells concerning the bandgap of light absorbers (PSCs and other PVs) are shown in Figure 1a. Though the highest PCE (over 25%) of PSCs is surpassing most PVs, the efficiencies of other PSCs are not so outstanding and also have a big room to improve compared with the S-Q limits. For achieving higher efficiency in approaching the S-Q limits, understanding the loss in each parameter of PSCs and what causes the loss are necessary.

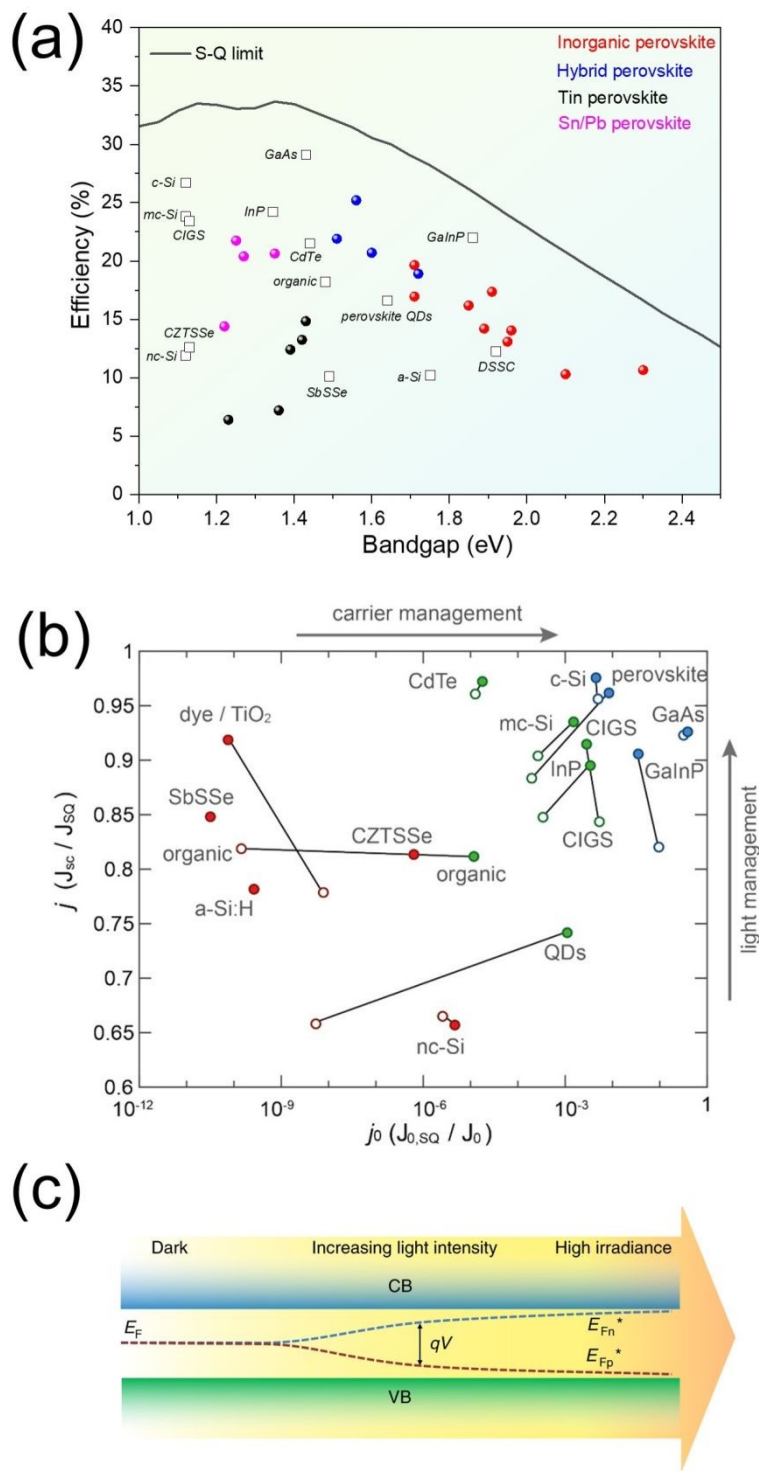


Figure 1 (a) Efficiencies of various photovoltaics relatives to the S-Q limit under standardized AM1.5 illumination conditions. (b) Current density relative to the maximum possible current density, under standardized AM1.5 illumination conditions, versus minimum dark recombination current density relative to the recombination current derived for the record cells.¹⁰ Copyright 2020, American Chemical Society. (c) Schematic illustration of the Fermi level splitting in a solar absorber material with increasing light

intensity. E_F represents the intrinsic Fermi level. E_{Fn}^* and E_{Fp}^* are the quasi-Fermi levels for electrons and holes respectively, where light absorption results in electrons populating the conduction band (CB) and holes populating the valence band (VB).¹¹ Reprinted with permission from Nature Publishing Group (2018).

Essentially, the total loss in the solar cell is composed of loss in the light (inefficient light management) and loss in the carriers (poor carrier management). A comparison between the short-circuit current density (J_{SC}) (i.e. measured short circuit current of the cell) and maximum possible current J_{SQ} (by S-Q limit) can quantify the photocurrent loss, which is mainly from the photon trapped inside the cell and light absorption by inactive regions of the cell.¹⁰ The value of j , calculated by $j = J_{SC}/J_{SQ}$, represents light management and a larger value means better light management, e.g., lower photocurrent loss. As shown in Figure 1b, the j value of PSCs is over 0.95, meaning close-to-perfect light management and a little room for improvement. The carrier recombination losses of a photovoltaic cell can be confirmed by the ratio of the lowest possible recombination current at the material's bandgap (i.e. the radiative limit), $J_{0,SQ}$, to the dark recombination current, J_0 .¹⁰ A low $j_0 = J_{0,SQ}/J_0$ indicates that better carrier management by reducing bulk and surface recombination is necessary. Figure 1b shows that j_0 for PSCs lies in the range of $10^{-3} \sim 10^{-2}$, which is lower than other solar cells such as GaAs ($10^{-1} \sim 1$).

Fill factor (FF) is defined as the ratio of the maximum power from the solar cell to the product of V_{OC} and J_{SC} . An empirical expression for FF is:¹²

$$FF = \frac{\frac{qV_{OC}}{nkT} - \ln\left(\frac{qV_{OC}}{nkT} + 0.72\right)}{\frac{qV_{OC}}{nkT} + 1}$$

Here, n is the ideality factor, k is Boltzmann's constant, T is the temperature, and q is the elementary charge. The n value is a measure of the junction quality and the type of recombination in a solar cell, which will be introduced in the following part. This equation demonstrates the importance of the n of a solar cell: the lower n gives a higher FF and vice-versa. Note that, this equation represents the maximum possible FF, and the actual FF is also affected by the parasitic resistive loss. From the above discussion, it's clear that the non-radiative recombination in PSCs is particularly important in determining photovoltaic performance. Thus, understanding and suppressing the non-radiative recombination in solar cells is the key to enhancing efficiency.

According to the basic physical process of photovoltaic technology, under sunlight illumination, electrons are excited from the valance band (VB) of a semiconductor to its conduction band (CB), leaving holes in the former. In this case, the Fermi level of the semiconductor in the thermal equilibrium state is not suitable anymore and will be split into quasi-Fermi levels of electrons (E_{Fn}) and holes (E_{Fp}), as shown in Figure 1c. In the S-Q limit theory, the difference between quasi-Fermi levels for electrons and holes sets the achievable value of V_{OC} for a solar cell. That is to say, ideally, quasi-Fermi level splitting (QFLS) and V_{OC} are two interchangeable quantities that are considered equal to each other. The V_{OC} of a solar cell in terms of the

classical diode equation can be written as:¹³

$$V_{OC} = \frac{n k T}{q} \cdot \ln \left(\frac{J_{SC}}{J_0} + 1 \right)$$

It can also be transformed into the following equation:

$$J_{SC} = J_0 \cdot \left(e^{\frac{q V_{OC}}{n k T}} - 1 \right)$$

The above equations show that V_{OC} depends on the dark saturation current of the solar cell and the light-generated current. J_{SC} of PSCs has a small variation because of the almost-perfect light management and fixed light intensity. Whereas, the dark saturation current depending on the non-radiative recombination in the solar cell may vary by order of magnitude. Therefore, any non-radiative recombination of the carrier could reduce the QFLS and contribute to the V_{OC} reduction.¹⁴ The equation also indicates the logarithmical dependence of V_{OC} on the light intensity. For comparing solar cells with different light absorbers (different E_g), a prefactor, diode ideality factor n was introduced, which can be determined from a measurement of V_{OC} as a function of light intensity I :

$$q V_{OC} = E_g - n k T \ln \frac{I_0}{I}$$

Here, I_0 is a constant with the same unit as I . The experimentally determined n is now popularly used directly to identify the non-radiative recombination properties in solar cells.¹⁵

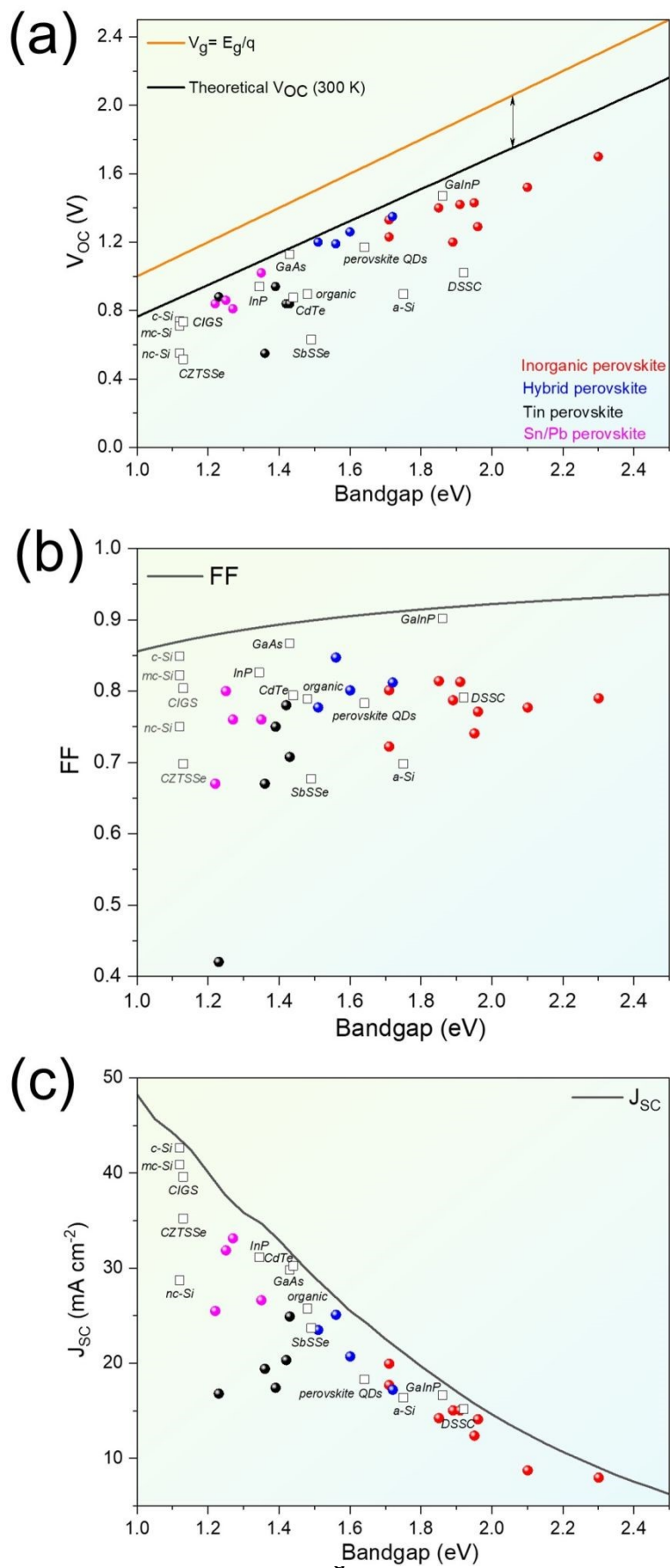


Figure 2 (a) V_{OC} , (b) FF, and (c) J_{SC} of various photovoltaics relative to the S-Q limits under standardized AM1.5 illumination conditions. The values are derived from the cells with record V_{OC} .

From the above discussion, we can find that non-radiative recombination is a decisive factor in the photovoltaic parameters and the final efficiency of a solar cell. Among three parameters, V_{OC} is most heavily affected by non-radiative recombination. Though extremely high V_{OC} of 1.18 V has been achieved in the high efficiency (25.2%) PSCs,⁴ the V_{OC} in most cases is not so satisfactory. A summary of champion V_{OC} values for PSCs employing different perovskites and the champion V_{OC} of other PVs is shown in Figure 2a. Here, the achieved V_{OC} of PSCs, especially the hybrid ones, are closer to the theoretical values compared with other PVs, which makes PSCs produce high performances. While the V_{OC} values for wide-bandgap and narrow-bandgap perovskites diverge from the line of theoretical V_{OC} . For example, using the wide-bandgap (1.91 eV) CsPbI₂Br perovskite, we achieved an unprecedented V_{OC} of 1.43 V, which still has an energy loss ($E_{loss} = E_g - eV_{OC}$) of 0.48 eV.¹⁶ Highest V_{OC} of 1.33 V for CsPbI₃ ($E_g = 1.71$ eV) was obtained, showing an E_{loss} of 0.38 eV.¹⁷ For narrow-bandgap tin-based PSCs, the champion V_{OC} is 0.94 V using a tin perovskite with an E_g of 1.39 eV, exhibiting an E_{loss} of 0.45 eV.¹⁸ For further boosting the performance of PSCs toward the S-Q limit, it is essential to understand the non-radiative recombination types and minimize the recombination for achieving a better V_{OC} output.^{19, 20} We also summarized the FF and J_{SC} of the devices with the best V_{OC} (Figure 2b and c) and found that for all PSCs, the FF is lower than the theoretical value while most J_{SC} except tin-based PSCs is approaching J_{SQ} . It means for solar cells already with high V_{OC} , improving the FF is regarded as an effective way to further promote efficiency.⁵ As discussed above, FF is affected by the resistance and the non-radiative recombination in the solar cells. Therefore, if a high V_{OC} with low recombination is achievable, a good FF and high efficiency are also expected to get.

1.2 Defects and non-radiative loss

The non-radiative recombination limiting the V_{OC} occurs at both the intragap recombination centers (defects and traps) of a single perovskite layer and the heterojunctions between perovskite and the transport layers. It can be divided into several types including defect-assisted recombination (Shockley-Read-Hall, SRH recombination), Auger recombination, band-tail recombination, and interface recombination.²¹⁻²³ The recombination processes are depicted in Figure 3a. Defect-assisted recombination depends on the energy depths and the density of defects in perovskite film. Auger recombination is a process of thermal dissipation where the excess energy from the electron-hole recombination is transferred to electrons or holes that are subsequently excited to higher energy states within the same band instead of giving off photons (radiative recombination). Therefore, the same as radiative recombination, Auger recombination is also an intrinsic recombination process.²⁴ Auger recombination mainly occurs for perovskite film with high carrier concentration ($>10^{17}$ cm⁻³),³ while might not be a major process in perovskite with low carrier concentration (under the AM 1.5G illumination, carrier concentration $\sim 10^{13}$ to 10^{15} cm⁻³).²⁵ Therefore, it is believed that Auger non-radiative recombination has a negligible influence on the photovoltaic performance of the final device.²⁴ Band-tail states arise from continuous energetic disorder, caused by rotational freedom of the

polar organic cations in perovskite, such as formamidinium (FA) and methylammonium (MA).^{26, 27} They are in an energetic distribution in energy-band edges rather than well-defined defect levels in energy-band of perovskite. Band-tail recombination is associated with charge-carrier relaxation from the energy-band edges to the band-tail states via the release of photons, which results in a loss of V_{OC} output.^{21, 28} These band-tail states appear to be shallow trap states, which are possible to be reduced by increasing the crystallinity of perovskite and tuning the degree of the energetic disorder by substitution of the organic cation with inorganic Cs^+ or Rb^+ .^{28, 29} Therefore, Auger recombination and band-tail recombination are less important and not universal for all type PSCs. In this review paper, we will mainly focus on the SRH recombination in perovskite and interface recombination since they are significantly and universally affecting the E_{loss} and V_{OC} output,²² as shown in Figure 3b.

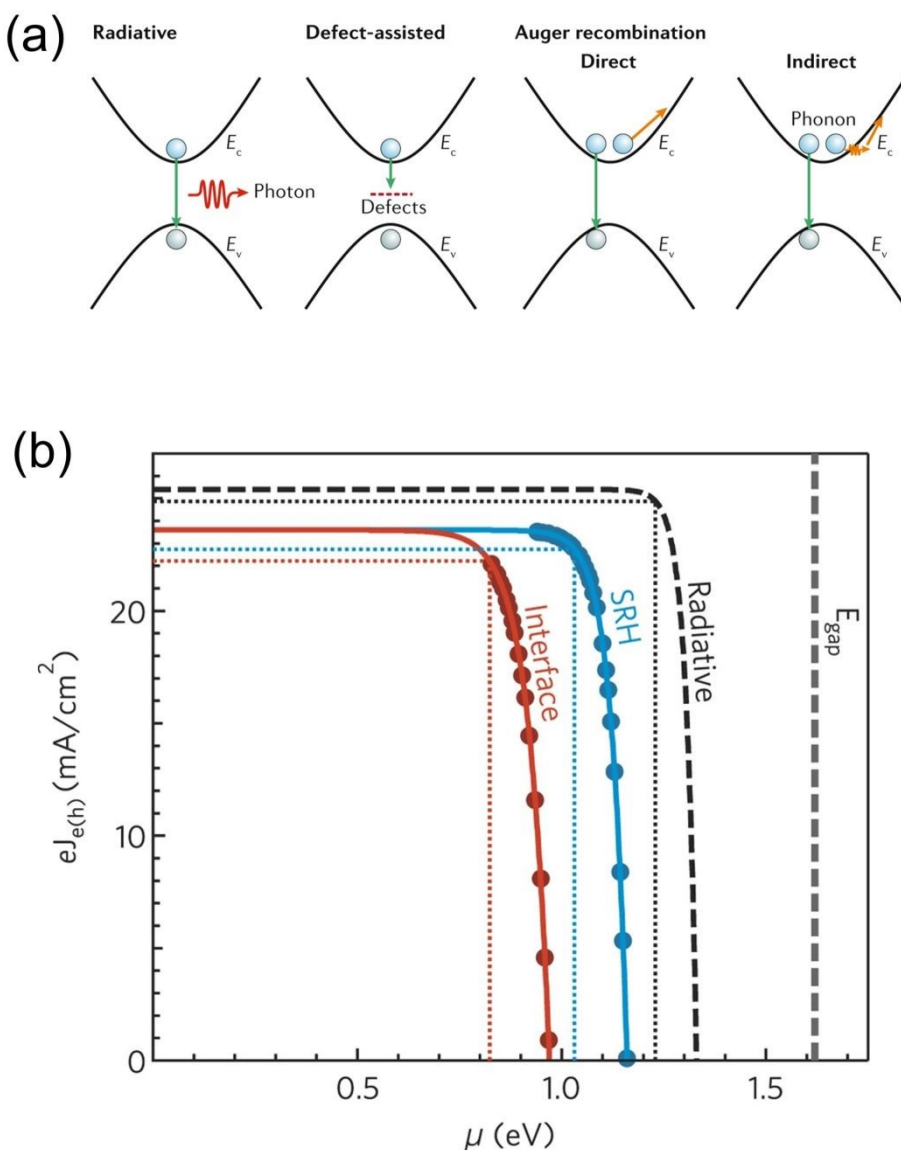


Figure 3 (a) Generalized recombination dynamics of the photo-generated carriers, including radiative, defect-assisted, and direct and indirect Auger recombination. E_c is the conduction band minimum and E_v is

the valence band maximum.²¹ Reprinted with permission from Nature Publishing Group (2020). (b) Electron (hole) charge current density as a function of the free energy. Solid lines represent the electron (hole) current $J_{e(h)}(\mu) = J_{\text{sun}} - J_{\text{rec}}$. The dotted lines mark the point of maximum extraction of electrical power. Red curves and circles: electron (hole) current density in the double heterojunction; recombination is dominated by interface electron and hole annihilations. Cyan curves and circles: electron (hole) current density in the single hybrid perovskite layer; recombination is due to electron and hole SRH annihilations alone. Dashed line: $J_{e(h)}(\mu)$ in the S-Q limit.²³ Reprinted with permission from Nature Publishing Group (2020).

In PSCs, the photogenerated electrons and holes must be sufficiently collected by the n-type electron transport layer (ETL) and p-type hole transport material (HTM), respectively, before being trapped by defects in perovskite, e.g., SRH recombination.³⁰ The mainly studied defects are point defects including interstitials,³¹ vacancies,³² and antisites³³ in perovskite. They are almost-positive or almost-negative charged and holes or electrons can be localized near the defects. Some of the defects have high forming energy (deep-level defects) and work as deep-level recombination centers, which are the predominant sources of non-radiative recombination losses. In contrast, shallow-level defects with low forming energy have a negligible impact on non-radiative decays.³⁴ As a solution-processed film with a variety of compositions and fabrication processes, the defects in perovskite are quite a complex topic. For example, electron-phonon interaction popularly appears in perovskite materials and it is also a source of non-radiative recombination loss.²² However, the working mechanism and the role of this interaction in determining the final V_{OC} output are still unclear. Though the defect physics is quite complex, researchers have proved some helpful strategies for minimizing the SRH non-radiative recombination. For instance, improving the perovskite film quality, enlarging the crystal size, and passivating the defects in both bulk and surface have been widely studied.³⁵⁻³⁷

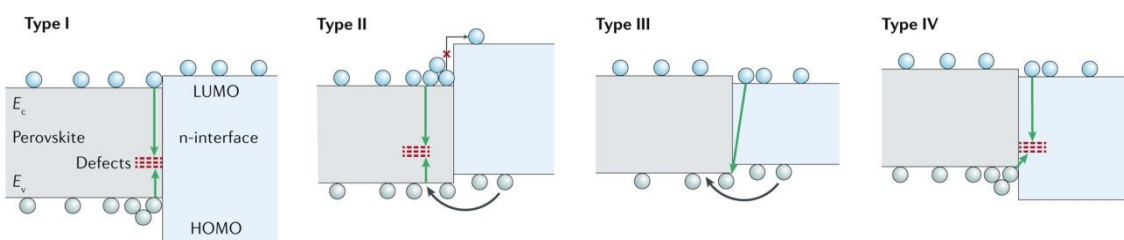


Figure 4 Diagrams showing the origins of interface-induced recombination losses, including deep-level defects within the perovskite absorber (type I), unfavorable band alignment at the interface and defects in the perovskite (type II), back-transfer-induced recombination (type III), and defect-assisted recombination in the ETL (type IV). The recombination processes occur similarly at the perovskite/HTM interface. HOMO, highest occupied molecular orbital; LUMO, lowest unoccupied molecular orbital.²¹ Reprinted with permission from Nature Publishing Group (2020).

Interface recombination is the non-radiative recombination caused by mismatched energy level alignment, surface defects, and carrier back transfer.^{14, 38-40} In general, in a perovskite photovoltaic device, the photo-

generated electrons should be selectively extracted by ETL, which also blocks the holes through a large Schottky barrier at the perovskite/ETL interface. At the same time, the holes should be extracted by HTM, which also blocks electrons. Hence, the imperfect charge transfer and blocking will cause charge recombination at the interface, resulting in energy loss. For example, QFLS of perovskite continuously increases with increasing the light intensity while V_{OC} shows a saturation.^{11, 41} A possible reason is the reduced selectivity of the hole-extracting contact that gives rise to the interface recombination. Hence perovskite/transport layer interface non-radiative recombination also plays an extremely important role in governing E_{loss} in PSCs. As shown in Figure 4, there are four types of recombination at the interface.²¹ In the first type, the lowest unoccupied molecular orbital (LUMO) or CB of ETL is a little higher than that of perovskite, which associates with charge recombination within the perovskite layer. In the second type, the LUMO of ETL is much higher than that of perovskite, resulting in electron accumulation at the interface and recombination in the perovskite layer. When the energy barrier at the interface is over 0.2 eV, the electron extraction will be blocked.⁴² The third and fourth types represent the situation where the LUMO of ETL is lower than that of perovskite, resulting in good energy alignment and charge extraction efficiency. While the electrons injected into ETL can recombine with holes at the VB of perovskite (back transferred from ETL) because of the small difference between these energy levels. This is quite popular in the normal structure (n-i-p) of tin-based PSCs. In addition, the undesirable surface defect in ETL could also cause electron recombination (fourth type). More importantly, too low CB of ETL, meaning large energy offset at the perovskite/ETL interface, will lower the quasi-Fermi level of electrons, resulting into low V_{OC} output. Similar recombination processes occur at the perovskite/HTM interface. The recombination processes at both perovskite/ETL and perovskite/HTM interface significantly contribute to the external V_{OC} deviation from the internal QFLS of perovskite.

1.3 Quantifying non-radiative loss

Using optoelectronic measurements to quantify the non-radiative V_{OC} loss can help us better understand the energy loss of a complete device. Electroluminescence (EL), photoluminescence (PL), transient photoluminescence (TRPL), photoluminescence quantum yield (PLQY), electrochemical impedance spectroscopy (EIS), transient photovoltage (TPV), and space charge-limited currents (SCLC) have been used to evaluate defects and the non-radiative recombination. While knowing the contribution of each layer and interface to the total non-radiative V_{OC} loss ($\Delta V_{OC, nrad}$) is more significant than knowing the general information on defect level and the loss of the whole device. This is because by figuring out the origin of non-radiative V_{OC} loss, we can design tailored strategies to suppress the recombination and boost the V_{OC} output. PLQY has proven to be useful in estimating the $\Delta V_{OC, nrad}$ of each layer and interface.⁴³

The maximum V_{OC} calculated using the S-Q theory ($V_{OC, S-Q}$) is based on the assumptions that 1) all the photons with energy greater than the E_g of the light absorber can be absorbed and 2) radiative recombination is the only recombination type. Because of the materials finiteness, not all the photons can be absorbed in a real light absorber, which reduces the $V_{OC, S-Q}$ to its radiative limit ($V_{OC, rad}$). Due to the existence of non-

radiative loss, the measured V_{OC} is smaller than $V_{OC,rad}$, and their relationship with $\Delta V_{OC,nrad}$ can be stated as:

$$V_{OC} = V_{OC,rad} - \Delta V_{OC,nrad}$$

Under an excitation intensity equivalent to one sun, a quantitative relationship between the PLQY and the $\Delta V_{OC,nrad}$ can be described with the formula:²⁴

$$\Delta V_{OC,nrad} = -\frac{kT}{q} \ln(PLQY)$$

Then the relationship between measure V_{OC} and the PLQY can be written as:

$$V_{OC} = V_{OC,rad} + \frac{kT}{q} \ln(PLQY)$$

PLQY of a PSC sample depends on the factors such as the quality of the perovskite film, the energy level of the CTls, and additional recombination pathways at the perovskite/CTL interfaces.²¹ The non-radiative loss in perovskite can be quantified by measuring the PLQY of an isolated perovskite film and when CTls contact the perovskite layer, the fall in PLQY reflects the recombination loss at the interfaces.

Hagfeldt et al. determined the contribution of different recombination processes to the total non-radiative loss.⁴⁴ In their research, a molecule was used to passivate the perovskite surface (the side contacting with HTM, top surface) defects. By measuring the PLQY of perovskite film on ETL and the complete device, the losses caused by different processes were calculated using the following equations: $\Delta V_{OC,nrad}$ (perovskite/ETL interface + bulk) = $V_{OC,rad}$ - $V_{OC,PLQY,film}$; $\Delta V_{OC,nrad}$ (perovskite/HTM interface) = $V_{OC,PLQY,film}$ - $V_{OC,PLQY,device}$; $\Delta V_{OC,nrad}$ (energetics, etc.) = $V_{OC,PLQY,device}$ - $V_{OC,measured}$. The $\Delta V_{OC,nrad}$ (perovskite/ETL interface + bulk) of both the control and target samples is 89 mV. The $\Delta V_{OC,nrad}$ (perovskite/HTM interface) in the control device is 44 mV, while surface passivation reduces it to 4 mV in the target device. The measured V_{OC} difference agrees with the value of 40 mV, indicating that the V_{OC} improvement is mostly due to a reduction in perovskite/HTM interface non-radiative loss, a result of the surface passivation.

1.4 Defect-tolerance property

As defects can cause a significant drop in the open-circuit voltage of solar cells, minimizing/eliminating defects is perhaps the only way to increase the V_{OC} of the cells. The solution-processed polycrystalline perovskite films, as expected, have quite a high density of defects ($10^{15-16} \text{ cm}^{-3}$) (defects density of silicon is in the order of 10^8 cm^{-3}) but fortunately, these defects do not do much damage to the performance. In other words, the defects in perovskites seem to be benign. Several studies have shown that the types of defects such as MA_i , V_{Pb} , MA_{Pb} , I_i , V_i , and V_{MA} which are most likely be present in the perovskite because of their low formation energy create only shallow trap states, about 0.05 eV above/below the VB/CB (Figure 5a and b) (or even within the bands), resulting in a subdued chance for carriers trapping.⁴⁵⁻⁴⁹ On the

other hand, the defects like I_{Pb} , I_{MA} , Pb_i , and Pb_l , which can form deep trap states and thus, cause carrier loss, have high energy of formation, and therefore, are not prevalent in the perovskite film. Another surprising fact about PSCs is that compositions including multiple cations and multiple halide ions, which must be prone to chemical inhomogeneity, often work with high performance. Recently, Stranks et al. found pieces of evidence supporting the fact that chemical heterogeneity in solution-processed mixed-cation, mixed-halide $FA_{0.79}MA_{0.16}Cs_{0.05}Pb(I_{0.83}Br_{0.17})_3$ perovskite rather helps in preventing the carriers from getting trapped.⁵⁰ The existence of Br and I induces the formation of beneficial local heterostructures that bestow enhanced defect tolerance on these materials. In these regions, charge-carrier generation and radiative recombination occur through a rapid wide-to-narrow bandgap funneling process (Figure 5c), which is more efficient than in the chemically homogeneous regions. The chemical disorder in these regions helps in the effective capture of diffusing carriers over micrometer-length scales to lead to radiative recombination, outcompeting the capture of carriers in more electronically disordered and trap-rich regions, thus resulting in strong luminescence and high performance. Studies authenticating defect tolerance of the perovskites with mixed B-cations are also coming out. For instance, from computational studies, Sargent et al. have recently identified a defect-tolerant region spanning a Sn content of 30-70% in mixed Pb-Sn perovskites and experimentally observed notably longer carrier lifetimes in 50% Sn mixed perovskite films than at other Sn contents. The composition $FA_{0.75}Cs_{0.25}Pb_{0.5}Sn_{0.5}(I_{0.9}Br_{0.1})_3$ achieves increased carrier lifetimes of $>1\ \mu s$ (Figure 5d).⁵¹ Although all-inorganic perovskites are lagging a bit behind the hybrid perovskites in achieving high V_{OC} with minimum E_{loss} , a recent theoretical study revealed that the $CsPbI_3$ can be more defect-tolerant than $MAPbI_3$.⁵² The V_{OC} loss in all-inorganic perovskites must be linked to the phase stability/impurity. Hence, it can be anticipated that the V_{OC} of all-inorganic perovskite solar cells can approach the theoretical limit by addressing the issues of phase stability/impurity at ambient conditions.

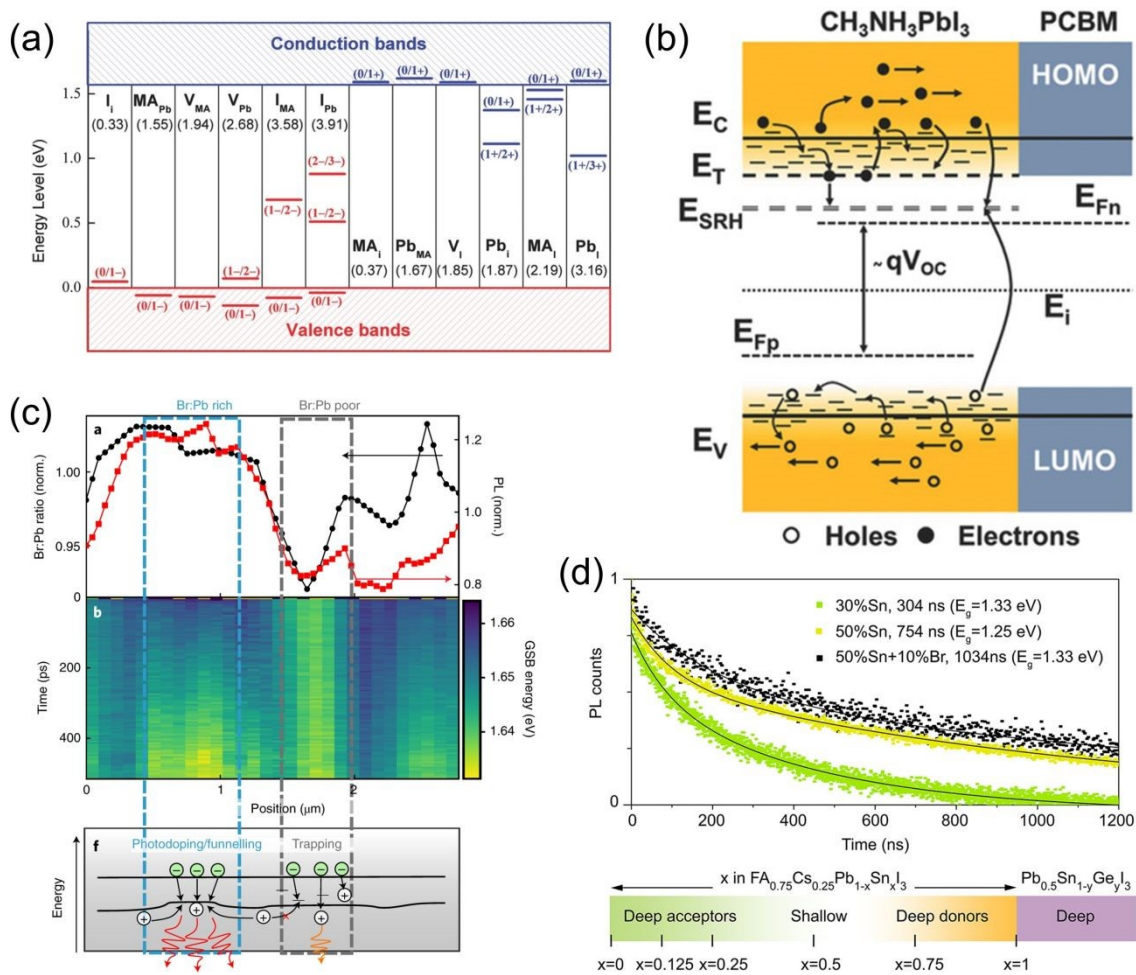


Figure 5 (a) Calculated transition energy levels of point defects in MAPbI_3 . The formation energies of neutral defects are shown in parentheses. The acceptors/donors are ordered by the formation energies (from left to right).⁴⁸ Copyright 2014, Wiley-VCH. (b) Energy-band diagram of the perovskite-based device representing the electronic transitions between the traps and the conduction and valence bands in a two-stage model for deep states.⁴⁹ Copyright 2017, Wiley-VCH. (c) Transient absorption microscopy of $\text{FA}_{0.79}\text{MA}_{0.16}\text{Cs}_{0.05}\text{Pb}(\text{I}_{0.83}\text{Br}_{0.17})_3$ perovskite films correlated with local chemical mapping. In the top, line scan of the Br: Pb nXRF intensity ratio (black dots) and normalized PL intensity (red squares) of the region used for correlation. In the middle, transient absorption microscopy line scan showing the center-of-mass value of the ground state bleaching as a function of time after excitation. The Br-rich and Br-poor regions are denoted with blue and grey rectangles, respectively. In the bottom, schematic of the proposed model showing carriers funnelling to highly emissive low bandgap regions in Br-rich regions, outcompeting carrier trapping in Br-poor regions.⁵⁰ Reprinted with permission from Nature Publishing Group (2021). (d) Time-resolved PL spectra of $\text{FA}_{0.75}\text{Cs}_{0.25}\text{Pb}_{(1-x)}\text{Sn}_x\text{I}_3$ perovskite films and schematic diagram of the defect tolerance behaviors in mixed Pb-Sn and mixed Pb-Sn-Ge alloys.⁵¹ Copyright 2021, American Chemical Society.

The above discussion presents the importance of V_{OC} output and E_{loss} in controlling the efficiency of PSCs.

By combining the mechanism and current development in V_{OC} of PSCs, we can deduce that there is still room for improving the V_{OC} output as well as the efficiency. In this review paper, we will discuss the current progress in V_{OC} enhancement for PSCs employing different light absorbers including organic-inorganic hybrid lead perovskites, all-inorganic lead perovskites, tin-based perovskites, and bismuth-based perovskites and their analogs. Through different strategies adopted in enhancing the V_{OC} , we can better understand how the imperfection in PSCs works and what methods can be used for further increasing the V_{OC} . It is apparent that in the current stage, the V_{OC} increment is a promising way to further promote the efficiency towards the S-Q limit, especially for PSCs employing all-inorganic lead perovskites, tin-based perovskites, and bismuth-based perovskites and its analogs as light absorbers. More importantly, higher V_{OC} is extremely desired for all-inorganic $CsPbX_3$ and tin-based PSCs, which are suffering from severe energy loss, because they can work as a top-cell or a bottom-cell in a perovskite/Si or perovskite/perovskite tandem solar cell, where V_{OC} is the sum of the top and bottom cell and low voltage of a single cell will limit the total voltage output. In addition, $CsPbX_3$ solar cells have the potential of working as indoor photovoltaics to power the Internet of Things (IoT) nodes because of their good matching with the indoor light spectra. In comparison with other indoor photovoltaics, such as DSSC, the remarkable advantage of PSCs is the expecting high V_{OC} output. While most indoor PSCs, even using wide-bandgap absorbers, hardly achieve V_{OC} over 1.0 V, which will lower their prospects for practical indoor application. In summary, the V_{OC} of PSCs still needs to be increased and the strategies summarized here in different systems could bring some ideas to researchers in designing more efficient PSCs with higher V_{OC} and efficiency.

2 Organic-inorganic hybrid perovskite solar cells

Despite the short history of PSCs, their PCEs have steadily increased recording over 25%. The high-efficiency PSCs (over 20%) are mostly based on organic-inorganic hybrid perovskites. In general, in all these cases, high PCEs mainly result from improved J_{SC} in addition to relatively higher FF while their V_{OCs} fall a little short of the limit estimated by the S-Q theory. At the early stages of research on hybrid PSCs, the perovskite layer itself was considered to be a primary factor to realize high V_{OC} . In the very first report by Miyasaka group, organic-inorganic hybrid PSCs consisting of methylammonium lead halides ($MAPbI_3$ or $MAPbBr_3$) in DSSC configuration, low PCE was mainly due to low V_{OC} . Extremely unstable perovskite in the liquid electrolyte environment prevented them from achieving high V_{OC} . After the development of solid-state PSCs based on solid hole transport materials, the processes to obtain high-quality perovskite films became the mainstream of PSC studies. V_{OC} over 1.0 V was easily obtained by using a 3:1 molar ratio of methylammonium iodide (MAI) and lead chloride ($PbCl_2$), recording over 19% of PCEs within a couple of years since the first solid-typed PSCs entered the stage.⁵³ Generally, among the photovoltaic parameters (J_{SC} , V_{OC} , FF), FF and J_{SC} are relatively consistent regardless of different batches with the same experimental conditions. The highest PCEs updated in the reports primarily result from the enhancement of V_{OC} . Although the importance of the realization of high V_{OC} has been emphasized, the exact mechanism to determine the V_{OC} in organic-inorganic PSCs has still not been fully uncovered.⁵⁴ A variety of methods

to obtain high-quality perovskite films have been developed including two-step spin coating, anti-solvent dripping, and additive-included perovskite precursors.⁵⁵⁻⁵⁸ Although those methods contributed to enhancing V_{OC} , the value saturated at some point lower than the S-Q limits.^{41, 59} Along with the circumstances where the anti-solvent method in which orthogonal solvents are dripped during the spin-coating is considered to be mature technology to minimize the defects of perovskite layers, the space to further enhance the quality of films has become limited. Also, the quality of perovskite films is adequate to draw potential performances from active layers even though they have slight defects, the mechanism of which is so-called defect-tolerant perovskites.^{60, 61} Faced with limitations of perovskite layers themselves, the study to maximize PCEs of organic-inorganic PSCs, has been shifted to interface engineering and charge transport layers. In this regard, we briefly review the recent methodologies followed to increase the V_{OC} of hybrid PSCs in the following sections categorized as (i) perovskite layer, (ii) ETL and interface, and (iii) HTM and interface.

2.1 Optimizing hybrid perovskite film preparation

2.1.1 Anti-solvent method for hybrid perovskites

Following the trend of anti-solvent dripping that has been a major stream of fabrication of high-quality perovskite films, many studies have been focused on the anti-solvent by either varying the kind of antisolvents, modifying the dripping condition, or using different additives to the antisolvents. While chlorobenzene is the most popular antisolvent, we found that diisopropyl ether is more effective in realizing high-quality hybrid $(\text{FAPbI}_3)_{0.85}(\text{CsPbBr}_3)_{0.15}$ perovskite films. As a result, it enhanced the V_{OC} output, in comparison to the former (i.e. chlorobenzene).⁶² It must be noted that although diverse anti-solvents have been attempted for hybrid perovskites, accurate classification of anti-solvents, depending on perovskite compositions, is still ambiguous. Indeed, most research groups recognized the importance of precise control of the dripping speed of anti-solvents as the quality of films strongly depends on the dripping speed, which is hard to control when done manually and differs by batches and persons. In addition, as the specific methodologies are not described accurately in most of the reports, other research groups often confront difficulties in reproducing the same performances. Very recently, Alexander et. al. provided a general approach to sorting anti-solvents by dividing them into fast and slow dripping.⁶³ In this report, three types of anti-solvents were suggested by the degree of solubility of perovskite components in the DMF/DMSO mixture. The optimized dispensing techniques of antisolvents improve the quality of polycrystalline perovskite film in terms of void-less dense morphology with a flatter surface and reduced grain boundary area with an array of large grains. Such high-quality film leads to enhancing performance, mostly resulting from the improved V_{OC} . While different antisolvents have been used to improve the film quality some studies also used additives in the antisolvent to control the crystallization. For instance, Xing et al. suggested regulating the kinetics of crystal growth of perovskite films by incorporation of n-type semiconductor, 1,3,5-Tris(1-phenyl-1H-benzimidazol-2-yl)benzene (TPBi) into the chlorobenzene anti-solvent.⁶⁴ The resultant high-quality $\text{Cs}_{0.05}\text{FAO}_{0.88}\text{MA}_{0.07}\text{PbI}_{2.79}\text{Br}_{0.21}$ perovskite film was considered to block possible hole movements toward ETL (Figure 6a), and the inverted PSCs (Figure 6b) based on this film recorded high

PCEs of 21.79%, which was mainly due to significant improvement in V_{OC} , from 1.03 to 1.15V (Figure 6c).

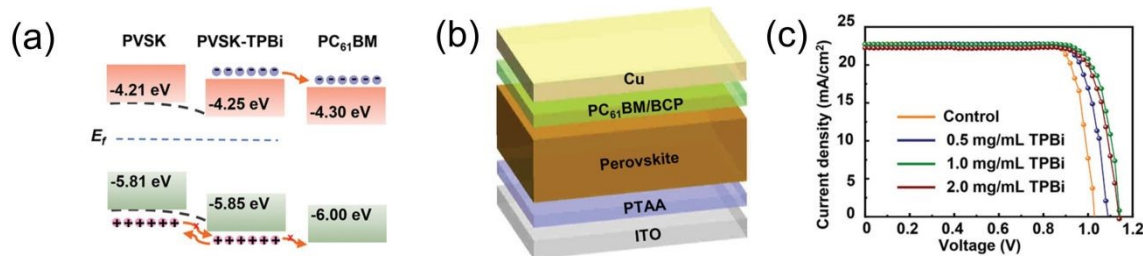


Figure 6 (a) Schematic illustration of energy levels of perovskite film with and without 1,3,5-Tris(1-phenyl-1H-benzimidazol-2-yl)benzene (TPBi), and PC₆₁BM film. (b) Schematic structure of inverted PSC. (c) J-V curves of various PSCs with different amounts of TPBi. (a)-(c),⁶⁴ Copyright 2021, Wiley-VCH.

2.1.2 Additives to hybrid perovskites

The additives added to perovskite precursor solutions are also another effective method for enhancing the quality of perovskite films. At the beginning of this additive-approach research, hydrochloric acid was incorporated into the perovskite precursors directly, smoothing the films.^{65, 66} Although there is no clear understanding that can help us to choose a suitable additive, a wide range of additives, such as organic or inorganic compounds, small and large molecules, and even polymers have been applied to improve grain growth, resulting in enhanced power conversion efficiency and stability as well in most cases.⁶⁷⁻⁶⁹ The interaction of the functional groups of the additives with the perovskites, and with the transport layers, has been considered to cause defect passivation and ion immobilization, improving the device performance and stability. As an example of a polymer additive, polyaniline has been found to result in outstanding performances. Here, the increase in V_{OC} was conspicuous, enhanced by 12%, compared to PSCs without additive.⁷⁰ The excessive amount of PbI₂ added to perovskite precursors have also been considered a possible approach for increasing V_{OC} , due to its passivation effect at grain boundaries.^{71, 72} This effect is also promising for inverted structure. Recently, Wu et al. added 5 mol% extra PbI₂ to the FAPbI₃ perovskite precursor, which resulted in better performance in the inverted structure owing to the increase in V_{OC} .⁷³ Moreover, they found the efficacy of excess PbI₂ depends on the HTM and the effect was more prominent on MeO-2PACz than on other HTMs including PEDOT:PSS, NiO_X, and PTAA. This demonstrates that inverted PSCs have a lot of potential for perovskite precursor engineering.

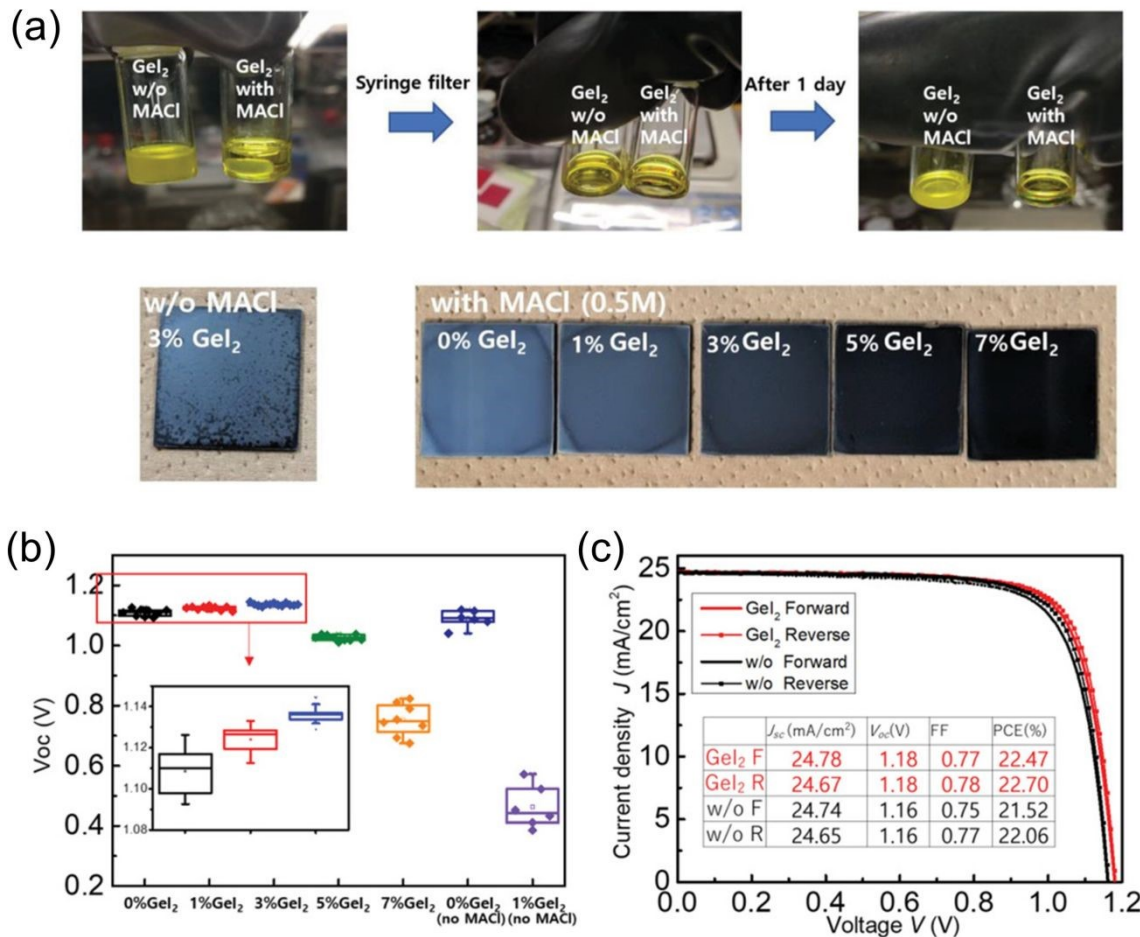


Figure 7 (a) Photographs of $\text{FA}_{0.83}\text{MA}_{0.17}\text{Ge}_x\text{Pb}_{1-x}(\text{I}_{0.9}\text{Br}_{0.1})_3$ ($x = 0.03$) precursor solution with and without MACl , and the resultant films with various concentration of GeI_2 ($x = 0-0.07$). (b) Box chart of V_{OC} for PSCs fabricated from MACl contained or not contained in precursor with various GeI_2 concentration. (c) J-V curves for the best performance cells with and without GeI_2 based on quadrupole cation-based perovskites (i.e. $\text{K}_{0.03}\text{Cs}_{0.05}(\text{FA}_{0.87}\text{MA}_{0.13})_{0.92}(\text{Ge}_{0.03}\text{Pb}_{0.97})(\text{I}_{0.9}\text{Br}_{0.1})_3$). (a)-(c),⁷⁴ Copyright 2020, Wiley-VCH.

Materials related to A-site cations in perovskites are also promising candidates as additives in precursors. Halides of methylammonium (MA), such as MAI and MACl have been confirmed by several independent studies to be effective when incorporated in precursor solutions with slightly excessive amounts.⁷⁵ Especially, MACl has been a prerequisite additive to most organic-inorganic-based perovskite precursors. The incorporation of MACl plays a critical role in making high-quality films, especially when FA is dominant in the precursors.⁷⁶ It has been also shown that MACl successfully induces the formation of an intermediate to the pure FAPbI_3 α -phase without annealing.⁷⁷ Most of the PSCs with the highest efficiencies have been based on perovskite precursors including MACl .⁷⁸ The major factor that enhances overall performances by incorporating MACl is the improved V_{OC} while the high value of J_{SC} is maintained. Before MACl was predominant, the addition of Br into precursors was the main concept to realize high V_{OC} .

because the band-gap of perovskites widens with a high ratio of Br to I in X site in perovskites. On the other hand, there is a trade-off between the increase in V_{OC} and the decrease in J_{SC} by the addition of Br, preventing PSCs from recording high efficiencies. However, MACl, which is eventually evaporated during annealing, hardly affects the bandgap of perovskites, and therefore, allows the accomplishment of high V_{OC} even though Br content is small. In fact, Seo et al. successfully achieved 25.2% PCE with extremely small amounts of Br (<1 mol%) in a mixed-halide-mixed-cation perovskite. The high V_{OC} of 1.198V was obtained with the composition of $(FAPbI_3)_{0.992}(MAPbBr_3)_{0.008}$ with the help of MACl.⁴ Different from the reports in which MACl is used as the only main additive that improves the film quality and hence the performance, in one of our studies, we found that MACl helped to incorporate Ge in a mixed-cation-mixed-halide perovskite.⁷⁴ Ge, one of the candidates for B site cations, was rarely used in organic-inorganic hybrid perovskites. Based on our experiments, we realized that one of the challenges to incorporating GeI_2 into perovskite precursors lies in the fact that GeI_2 is insoluble in standard perovskite precursor solutions (Figure 7a). Whereas, volatile MACl promotes non-volatile GeI_2 to be homogeneously dissolved in the precursors. These two volatile and non-volatile additives acted complementing each other, producing high-quality films and increased V_{OC} output (Figure 7b) caused by MACl and passivation effects caused by GeI_2 . A high PCE of over 22% was obtained using a $K_{0.03}Cs_{0.05}(FA_{0.87}MA_{0.13})_{0.92}(Ge_{0.03}Pb_{0.97})(I_{0.9}Br_{0.1})_3$ perovskite, and owing to significantly increased V_{OC} (1.18 V) (Figure 7c). Fully replacing I with Br (e.g., $MAPbBr_3$) has also been studied because of its extremely high V_{OC} potential ($E_g = 2.30$ eV, $V_{OC}^{SQ} = 1.98$ V) and semi-transparent property.^{79, 80} Sun and co-workers, for example, reported a high V_{OC} of 1.57 V (8.70% efficiency) for a pure $MAPbBr_3$ solar cell by using carbon as the electrode.⁸¹ Grätzel et al. recently enhanced this value to 1.65 V (10.33%) by employing a methylamine vapor treatment to eliminate the corrugations at the TiO_2 /perovskite interface.⁷⁹ A similar solvent annealing method was developed to improve the $MAPbBr_3$ /ICBA interface, which allows the ICBA to penetrate the $MAPbBr_3$ film's defects/voids, resulting in a high V_{OC} of 1.60 V.⁸⁰ The efficacy of dual additives was also reported very recently by In et. al. who used MACl and CsCl simultaneously.⁸² Here, although it is not explicitly stated that CsCl is non-volatile, it can be easily reckoned based on its high boiling points that Cs stays in the film while MACl is evaporated. Thus, in other words, volatile and non-volatile additives were also used in this study. The optimized ratio for device efficiency of MACl/CsCl in $(FAPbI_3)_{0.96}(MAPbBr_3)_{0.04}$ perovskite precursors was found to be 2:1, although the highest average V_{OC} was achieved when only CsCl severs as the additive (Figure 8a). In this optimum case, a high V_{OC} of 1.1726 V was obtained while keeping a high value of J_{SC} (24.91 mA/cm²), recording a PCE of 23.22% (Figure 8b). The incorporation of isopropyl ammonium chloride (iPAmHCl) into perovskite precursors has been also found effective.⁸³ The iPAmHCl as a Cl-contained additive works positively in PSCs due to its volatile properties during thermal treatments after spin coating thereby not affecting final perovskite compositions. In the report, a high V_{OC} of 1.16 V was achieved despite a low bandgap of perovskite ($FAPbI_3$). Kirchartz and co-workers reported high V_{OC} exceeding 1.26 V (Figure 8c) for the $MAPbI_3$ -based PSCs made by adding lead acetate and $PbCl_2$ into the perovskite precursor, which resulted in a smooth film with large grains, reducing the perovskite bulk recombination.⁵ Simultaneously, the suppressed perovskite surface or interface recombination by optimization of the CTLs is also an

important reason for such high V_{OC} .

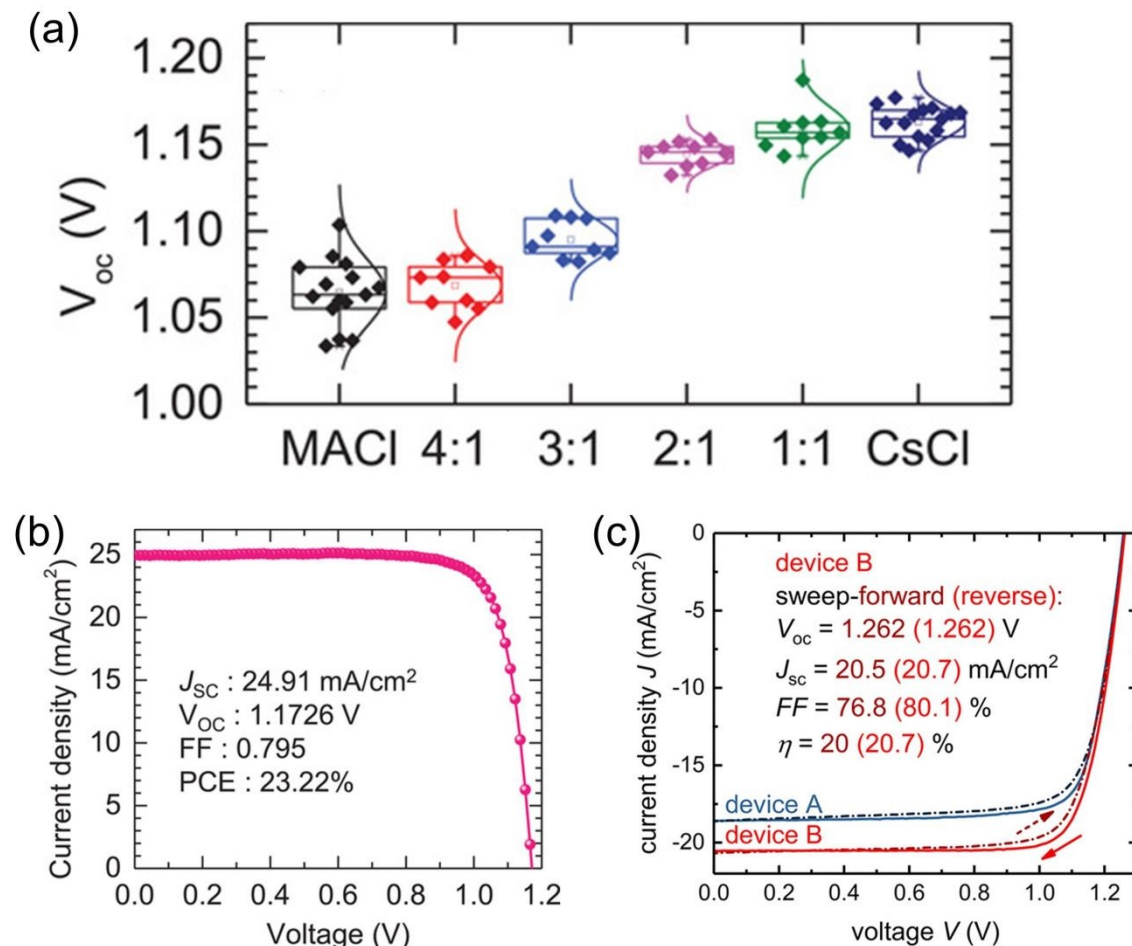


Figure 8 (a) V_{OC} for the PSCs based on $(\text{FAPbI}_3)_{0.96}(\text{MAPbBr}_3)_{0.04}$ perovskite films prepared by a dual additive of MACl and CsCl with different mixing ratios. (b) Reverse scanned J-V curve of the best performing PSC employing perovskite film formed by dual additive with $[\text{MACl}]/[\text{CsCl}] = 2$. (a) and (b),⁸² Copyright 2021, Wiley-VCH. (c) J-V curves of MAPbI₃ solar cells. Device A (blue) was optimized for a high open-circuit voltage, and device B (red) was also optimized for efficiency by increasing the thickness of the absorber layer and making the PTAA layer thinner.⁵ Copyright 2019, American Chemical Society.

Although the advent of compositional engineering in which various components in A-site cations and X-site halides are used in diverse ratios in perovskite precursors has led to the astonishing accomplishment of achieving high PCEs, the analysis and uncovering of the mechanism of PSCs have become more complex. In most papers dealing with additive engineering and anti-solvent methods to optimize efficiencies including, the compositions and components of perovskites are fixed. In other words, the methods seemed to be specific to compositions and environmental conditions. We have often experienced that the methods introduced in other reports are not reproducible in our systems/laboratories. While different environmental conditions such as temperature, pressure, and humidity may lead to the failure of experiments different perovskite compositions may also lead to reproducibility issues as the chemical or physical interactions of

additives or anti-solvents change by various cations and halides in the perovskite precursors. We recently reported that the perovskite films are largely affected by the evaporation kinetics of perovskite precursors during annealing when using the anti-solvent method.⁸⁴ Moreover, we also found that the sensitivity of the evaporation kinetics of precursors strongly depends on perovskite compositions. It was evident that the film quality strongly depends on the conversion of intermediates, which vary with composition, to perovskites during annealing. Hence, optimization of the evaporation kinetics is important for achieving high PCE. As witnessed in our system, the resulting high PCEs with optimized evaporation kinetics are mainly caused by the improved V_{OC} . Another research regarding improved V_{OC} by control of perovskite formation was conducted by Fan et.al. who tried to form perovskite films under high relative humidity in addition to DMSO-atmosphere during annealing.⁸⁵ Although the specific kinetic mechanism in the above case was not manifested, the resulting perovskite films showed superior V_{OC} , explained by induced self-passivation of perovskites that minimize surface defects and lattice distortion. Similarly, our group reported that the exposure of DMSO to perovskite films enables small fragments of perovskite crystals to be fused.⁸⁶ The mechanism behind this is called the Ostwald Ripening effect.⁸⁷⁻⁸⁹ Wu group tried to incorporate gadolinium fluoride (GdF_3) as an additive in perovskite precursors in parallel with aminobutanol vapor, thereby accelerating the Ostwald Ripening effect.⁹⁰ This dual approach applying additive and solvent annealing resulted in improved PCE caused by an increase in V_{OC} , recording 1.17 V.

From the above discussion, we can deduce that improving the perovskite film quality by optimizing the anti-solvent, incorporating proper additives, and controlling the perovskite crystallization process is an effective way to promote the V_{OC} output for hybrid PSCs. Although obtaining hybrid perovskite films with good morphology is not a challenge at the current stage, exploration of further improvement of film quality as well as reduction of the defects continues to hold great significance as a research topic. Recent studies found that high-quality perovskite films with enhanced V_{OC} always have long stability against air and electrical stress. This is because the high-quality perovskite films made by improved perovskite crystallization are likely to accompany dense films with few defects, preventing intrusion of moisture and leading to overcoming stability issues. Also, we believe that the use of certain additives helps in the distribution of the various components (A and X ions) across the film more uniformly, resulting in better chemical homogeneity.

2.2 Improving ETL and interface

The dense films with large grains/fewer grain boundaries that are also passivated with molecules (additives) in some cases work with higher V_{OC} due to reduced non-radiative recombination of carriers in the bulk of the film but carriers can also recombine at the interfaces of the perovskite with either the ETL or the HTM. Indeed, in some cases, this interfacial recombination, depending on the energy level matching and traps in the ETL or HTM, can be more significant than the bulk recombination. Therefore, the interfaces are equally important for improving the V_{OC} . TiO_2 has been widely used as an ETL in organic-inorganic hybrid-based PSCs. The best performances based on TiO_2 are seen in the cases where dual layers consisting of compact-

TiO_2 and mesoporous- TiO_2 are used as ETL. A great amount of work also has been done to modify the TiO_2 to form a better interface with the perovskite and hence, improve the V_{OC} . As an example, Hong and co-workers modified the surface of mesoporous- TiO_2 with a Nb_2O_5 layer deposited by the atomic layer deposition technique.⁹¹ They found that the ultrathin Nb_2O_5 layer improved the optoelectronic properties and morphology of the deposited perovskite films, enhanced the charge transfer, and suppressed the recombination at the interface. As a result, the solar cells using $\text{Cs}_{0.1}\text{FA}_{0.9}\text{PbI}_3$ as the light absorber showed a higher V_{OC} of 1.147 V and PCE of 21.04%, while 1.118 V and 19.11%, respectively, for the bare TiO_2 based device. Aranda et al. doped Li^+ into TiO_2 for MAPbBr_3 solar cells, resulting in a significant increase in V_{OC} from 1.36 to 1.58 V.^{92, 93} They discovered that Li^+ doping helps to modify the electronic charge distribution at the TiO_2 /perovskite interface, which could suppress the undesired non-radiative recombination and enhance the radiative recombination in the perovskite. Despite their high efficiency, the sintering process requiring over 500 °C to form anatase- TiO_2 can add to the overall cost of the device, leading to high cost-performance.⁹⁴⁻⁹⁷ Moreover, such a high-temperature process can not be applied to flexible PSCs, which is considered to give PSCs an advantage over other rigid inorganic PVs, in the view of commercial success. Hence, the development of SnO_2 , which can be made relatively at low temperatures and by simple solution methods, for use as an ETL in PSCs has received a lot of attention recently.⁹⁸ Many research groups are focusing on optimizing SnO_2 to achieve high V_{OC} and efficiency.

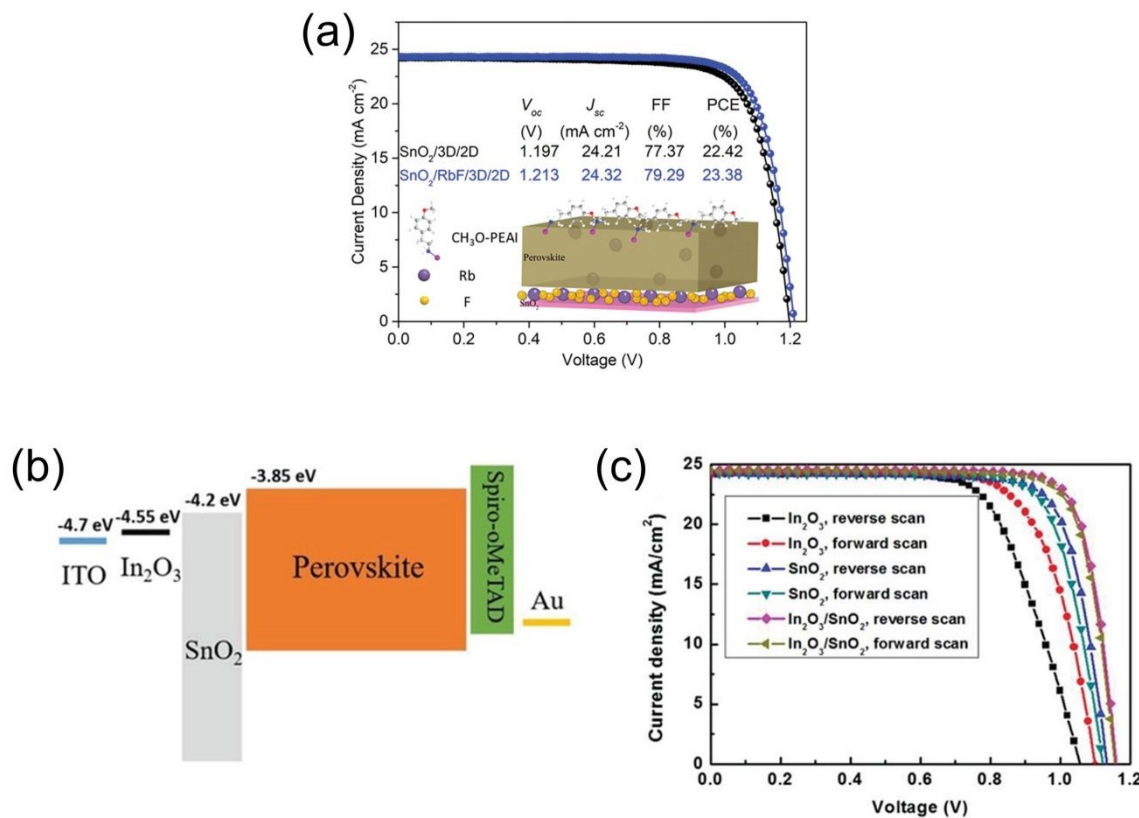


Figure 9 (a) J-V curves of 2D-3D champion PSCs based on SnO_2 and SnO_2/RbF . The inserted structure is the double-passivated perovskite model.⁹⁹ Copyright 2021, Wiley-VCH.

based on $\text{In}_2\text{O}_3/\text{SnO}_2$. (c) J-V curves from reverse and forward scanning for In_2O_3 , SnO_2 , and $\text{In}_2\text{O}_3/\text{SnO}_2$ -based devices. (b) and (c),¹⁰⁰ Copyright 2020, Wiley-VCH.

In addition to optimization of the coating and annealing methods to form SnO_2 or SnO_x , efforts have been made to modify/passivate the surface of SnO_2 or SnO_x as further improvement toward achieving higher V_{OC} . Recently, Mao et al. obtained high V_{OC} by spin coating RbF aqueous solution on SnO_2 film.⁹⁹ The Rb^+ cations actively escape into the interstitial sites of the perovskite lattice to inhibit migration and reduce non-radiative recombination. Here, with the help of the introduction of 2D perovskite materials on the perovskite layer, meaning the synergistic effect of ETL and passivation layers, the authors could achieve an astonishingly high V_{OC} of 1.213 V with a small E_{loss} of 0.347 eV (Figure 9a). Introduction of 3-(formamidinothio)-1-propanesulfonic acid (FTPS) into SnO_2 is also effective for achieving high V_{OC} .¹⁰¹ SnO_2+FTPS precursor solutions can be simply prepared by mixing FTPS dissolved in water with colloidal SnO_2 dispersed in water. The commercially available SnO_2 colloidal precursors should be handled with care as SnO_2 particles are easily aggregated by exposure to solvents except for water due to malfunctioning of functional groups attached to SnO_2 for better dispersion in water. Thus, typically doping materials should be prepared in water that is homogeneously mixed with SnO_2 without aggregation. In this regard, FTPS is adequate due to its extremely high solubility in water. As confirmed, the electrical resistance of ETL is reduced while the transparency of ITO and the light absorption ability of perovskite are hardly affected. The resulting performance of $\text{FA}_{1-x}\text{MA}_x\text{PbI}_3$ -based PSCs using SnO_2+FTPS recorded 22.3% PCE with V_{OC} of 1.141 V, while only 1.098 V was obtained for the reference using only SnO_2 as ETL. Similarly, the mixing of trimethylene phosphonic acid (ATMP) and KOH with SnO_2 precursor was reported to increase V_{OC} . The effect of these doping materials on the PSC was manifested as the minimization of Pb leakage from perovskite layers through Pb^{2+} ions being absorbed by ATMP, KOH-modified SnO_2 .¹⁰² In addition, ATMP could passivate oxygen vacancies in SnO_2 by reducing hydroxyl groups residing in ETL, thereby realizing optimized conditions at ETL/perovskite interface. Also, UPS measurement revealed that the work function of the ETL was shifted upward by ATMP to reduce the loss of energy during electron transfer. Overall, water-soluble acids such as FTPS and ATMP, which are easily blended with SnO_2 work well towards enhancing the electrical properties of ETL by either reducing defects of SnO_2 or shifting the energy level. Except for coating additional layer/material on SnO_2 , incorporation of the additional layer beneath SnO_2 is also reported.^{100, 103} For example, Zhang et al. recently revealed the effectiveness of dual ETL in which an In_2O_3 layer was coated beneath SnO_2 (Figure 9b).¹⁰⁰ First, the In_2O_3 layer is made on ITO by coating a precursor consisting of Indium nitrate pentahydrate, which does not require a sintering step (low-temperature process) and is followed by coating commercially available colloidal SnO_2 . Using this bilayer ETL, a high V_{OC} of 1.17 V (showing a low E_{loss} of 0.36 eV) and an efficiency of 23.24% was achieved with PSCs employing a 1.53 eV-perovskite as the absorber (Figure 9c). For the cases using single In_2O_3 and SnO_2 , a lower V_{OC} of 1.10 and 1.13 V were observed, respectively. The main reason for the improved V_{OC} in the case of the bilayer was thought to be the enhanced charge transfer from perovskite to ETL, due to the shallower CB of In_2O_3 than the working function of the ITO electrode, meaning better energy alignment at

the device interface. Moreover, the presence of In_2O_3 results in uniform, compact, and low-trap-density perovskite films, which also account for the enhanced V_{OC} and PCE. Therefore, in the SnO_2 -included bilayer ETL, the additional layers on SnO_2 work as an interfacial enhancer to optimize charge transfer between ETL and perovskites while supplementary layers beneath SnO_2 tend to facilitate the quality of perovskite films driven by smooth ETL surface.

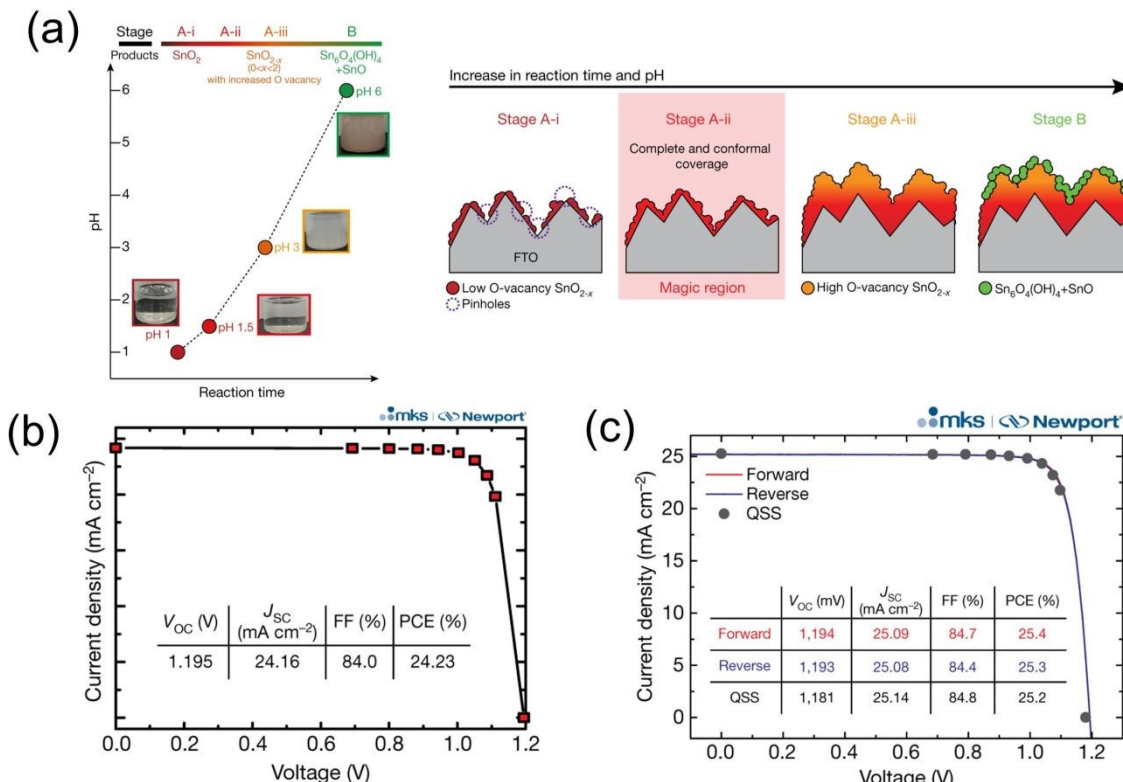


Figure 10 (a) Schematic illustration of the reaction progress with the photograph of the reaction solution at each stage and the progress of the reaction highlighting stage A-ii as the ‘magic region’, which exhibits ideal film coverage, morphology, and chemical composition. (b) Quasi-steady-state J-V curve of the best-performing device (stage A-ii) certified at Newport (MKS Instruments). The perovskite composition is FAPbI_3 with an added 5 mol% MAPbBr_3 . (c) J-V curves of the champion device measured at Newport, showing both the conventional J-V sweep and the certified quasi-steady-state measurements. The perovskite composition is FAPbI_3 with an added 0.8 mol% MAPbBr_3 . (a)-(c),⁴ Reprinted with permission from Nature Publishing Group (2021).

In addition to the commercial SnO_2 , many research groups have prepared SnO_2 ETL using the starting materials of SnCl_2 . For example, Seo and co-workers prepared the SnO_2 layer by the chemical bath deposition method and found that the pH of the freshly prepared chemical bath deposition solutions increases (from pH=1) with a longer reaction time (Figure 10a) as urea decomposes and releases OH^- .⁴ At the stage where pH=1.5, the solution produced a complete and conformal coverage of the SnO_2 layer on the FTO substrate (Figure 10a), which strongly prevents interfacial recombination. The solar cells

(perovskite composition of FAPbI_3 with 5 mol% MAPbBr_3) based on this ETL showed a high V_{OC} of 1.195 V, with a PCE of 24.23% (Figure 10b). With reducing the MAPbBr_3 amount to 0.8 mol% ($E_g = 1.56$ eV), PCE was further increased to 25.2% (Figure 10c). Li et al. recently reported remarkable improvement in V_{OC} of PSCs using perovskite with a bandgap of 1.54 eV by replacing the commercially available SnO_2 with newly synthesized ligand-tailored SnO_2 quantum dots (QDs).¹⁰⁴ The SnO_2 QDs ETL with multi-functional terminal groups refines the buried interfaces with both the perovskite and transparent electrode via enhanced interface binding and perovskite passivation. The perovskite crystallization direction was well controlled and the interface defects were reduced, leading to suppressed non-radiative recombination and a long carrier lifetime. The PSC using SnO_2 QD as ETL demonstrated a V_{OC} of 1.205 V (Figure 11a), while only 1.161 and 1.156 V for the devices employing SnO_2 ETL made from SnCl_2 and commercial SnO_2 nanoparticles, respectively. In addition, the SnO_2 QDs ETL also produced a high V_{OC} of 1.242 V for a perovskite with $E_g = 1.613$ eV. Such high V_{OC} for organic-inorganic hybrid-based PSCs using SnO_2 QDs have been also obtained for blade-coated perovskite, prepared by a low-temperature sintering process, facilitating mass production of PSCs. The organic ligand used in this experiment was 2-(2-aminoethyl) isothiourea dihydrobromide (2AT) having amine terminal groups. Double layer concepts using SnO_2 are usually combined with interfacial engineering as the upper layer on SnO_2 is in direct contact with perovskites, enhancing the ETL/perovskite interface. Multiple functional groups in 2AT such as -NH₂, -NH, and -Br groups promoted stabilization of interface by multifunctional ligand-tailored groups in newly synthesized SnO_2 QDs (Figure 11b). The results do not only show superior PCEs contributed by high V_{OC} but also better electrical stability compared to the cells with pristine SnO_2 .

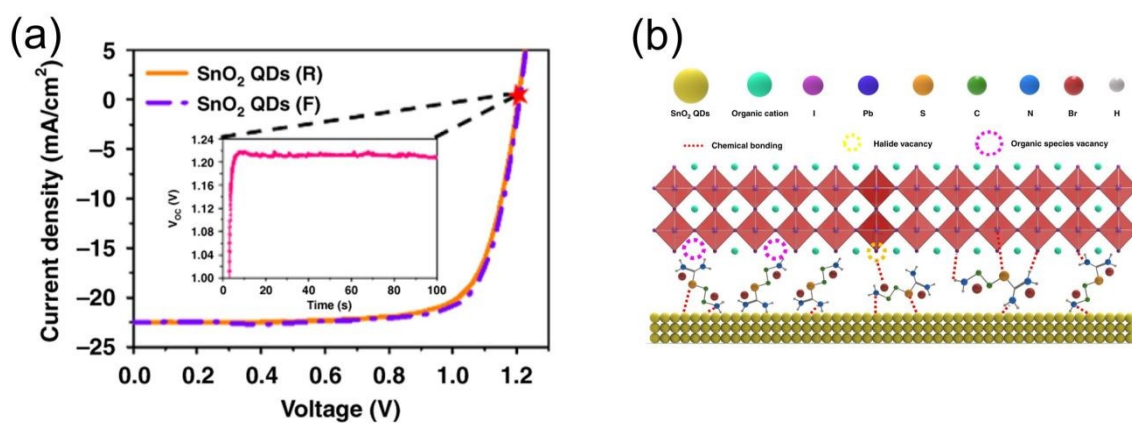


Figure 11 (a) Best-performing J-V curves with reverse and forward scans of PSCs with SnO_2 QDs ETL. Inset: stabilized V_{OC} as a function of the time. (b) Schematic illustration of proposed in situ interfacial defect passivation induced by utilizing ligand-tailored SnO_2 QDs. (a) and (b).¹⁰⁴ Reprinted with permission from Nature Publishing Group (2021).

Based on the aforementioned results, we can conclude that SnO_2 is becoming the most promising ETL for hybrid PSCs for achieving high V_{OC} and efficiency. While a single SnO_2 layer is not perfect some modification materials or layers are necessary to reduce the defects in SnO_2 and enhance the interface

interaction by minimizing the non-radiative recombination and tuning the energy alignment for better carrier transfer. One more advantage of modification of SnO_2 ETL is the control of perovskite growth, resulting in high-quality perovskite film and high V_{OC} of the solar cells.

2.3 Improving HTM and interface

In a similar manner to ETL, tremendous developments in HTM have been made to improve the overall performances of PSCs. As mentioned earlier, in the early stage of the development of PSCs the research was primarily focused on perovskites and ETL to realize high performance.¹⁰⁵ Since the light management of PSCs nearly approached S-Q limits, further enhancement in photocurrent of PSCs became challenging. Different from ETLs in PSCs that are mostly metal oxides such as TiO_2 and SnO_2 , which show stable and high PCEs, various types of HTMs have been used in PSCs that include metal oxide, small organic molecules, and polymers.¹⁰⁶⁻¹¹¹ In other words, there are more choices for HTM than for ETL. However, the most commonly used HTM in PSCs in conventional structure is Spiro-OMeTAD, which can be categorized under small molecules. The high solubility of Spiro-OMeTAD in aprotic solvents makes the fabrication process easy. To maximize the potential of Spiro-OMeTAD, dopants such as Li-TFSI, FK209, and tBP as an additive are used to increase the conductivity of the HTM. Otherwise, its intrinsic low hole mobility, owing to its small molecular structure, prevents PSCs from recording high performance. In general, high hole mobility and a HOMO level close to the VBM of perovskite are the necessary conditions for an HTM to work with high efficiency. Better HOMO level matching causes effective transfer of holes from the perovskite to the HTM and high hole mobility in the bulk of the HTM helps to transport them to the contact without loss. Although many high-efficiency PSCs are made with Spiro-OMeTAD as HTM that included the dopants (Li-TFSI), issues with the long-term stability of the cells arising from the diffusion of Li (from Li-TFSI) into perovskite and ingress of moisture caused by the hygroscopic nature of Li-TFSI have made the HTM less popular recently.

2.3.1 Modification of Spiro-OMeTAD HTM

To tackle the stability issue associated with Spiro-OMeTAD, modification of spiro-OMeTAD or introduction of newly synthesized small molecules that are similar to Spiro-OMeTAD has been applied to PSCs in the recent past. For example, Nam et. al slightly modified Spiro-OMeTAD by synthesizing a fluorene-terminated HTM (DM), the structure of which is described in Figure 12a.¹¹² DM has a deeper HOMO than Spiro-OMeTAD (Figure 12b), which is beneficial for the reduction of energy loss at the interface. Although Li and tBP dopants are also used here, the optimized amounts of dopants for DM were less than those used for the same molar amounts of Spiro-OMeTAD, despite the resemblance of their main structures. The optimized concentration of DM is also much less than Spiro-OMeTAD, appealing cost-effectiveness. The resulting PCE by using DM was over 22% for $(\text{FAPbI}_3)_{0.95}(\text{MAPbBr}_3)_{0.05}$ -based perovskites. This high performance was mainly caused by the enhancement of V_{OC} from 1.07 V to 1.11 V while other parameters (J_{SC} and FF) were similar in both cases (Figure 12c). Similarly, two fluorinated

isomeric analogs of Spiro-OMeTAD were developed and used as HTMs in hybrid PSCs.¹¹³ The fluorinated Spiro-*m*F and Spiro-*o*F have deeper HOMO values than that of Spiro-OMeTAD, which better match with perovskite (FAPbI_3) and thus, could reduce the energy loss at the perovskite/HTM. As a result, the PSCs employing FAPbI_3 (1.48 eV) perovskite showed enhanced V_{OC} of 1.164 V (24.82% efficiency) for Spiro-*m*F HTM and 1.161 V (24.50% efficiency) for Spiro-*o*F HTM, respectively, demonstrating only ~ 0.3 eV E_{loss} .

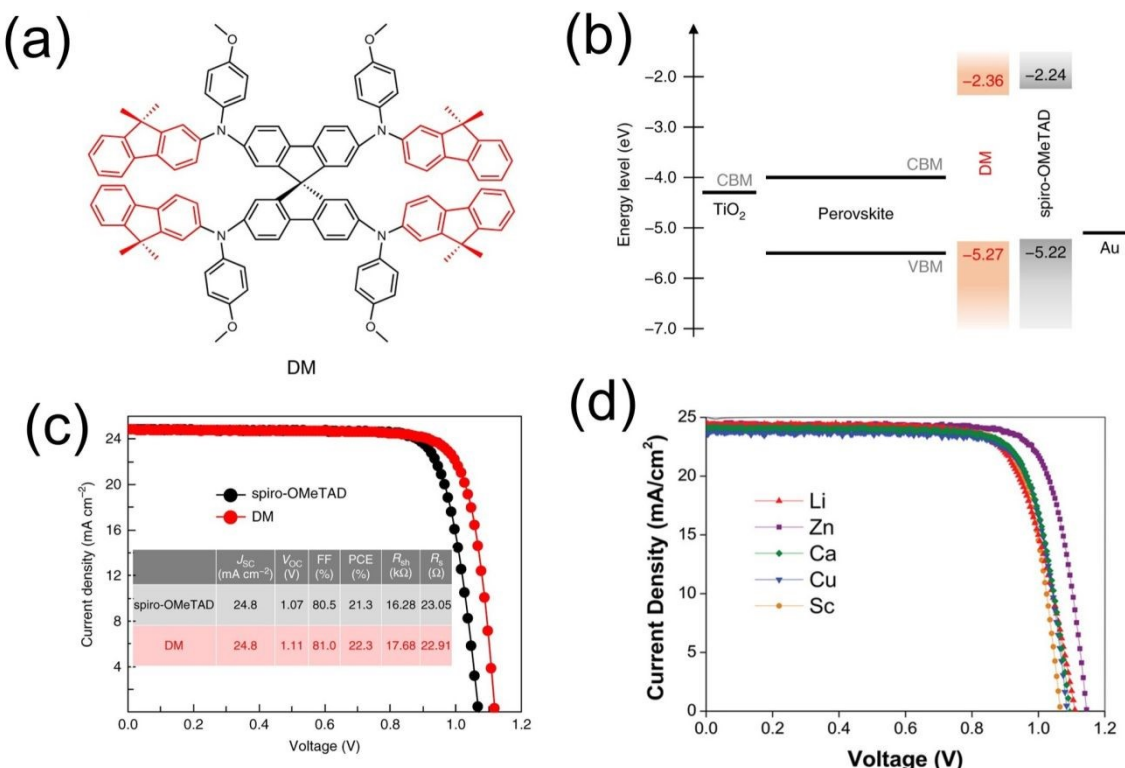


Figure 12 (a) Chemical structure of a fluorene-terminated HTM (N2,N2',N7,N7'-tetrakis(9,9-dimethyl-9H-fluoren-2-yl)-N2,N2',N7,N7'-tetrakis(4-methoxyphenyl)-9,9'-spirobi[fluorene]-2,2',7,7'-tetraamine) (abbreviated as DM). (b) Energy level diagram of DM and spiro-OMeTAD. CBM and VBM denote conduction band minimum and valence band maximum, respectively. (c) J-V curves of the average measured efficiency for the spiro-OMeTAD and DM-based devices. (a)-(c),¹¹² Reprinted with permission from Nature Publishing Group (2018). (d) J-V curves of the devices employing M(TFSI)_n as a dopant for spiro-OMeTAD.¹¹⁴ Copyright 2021, Wiley-VCH.

Replacing dopants prevalently used in Spiro-OMeTAD with new dopants is also an efficient method for changing/improving the cell performance as the complex synthetic procedure of novel HTM is not necessary. Wang et al. attempted to replace Li in Li-TFSI with alkaline-earth bis(trifluoromethanesulfonyl) additives to form Mg-TFSI₂ and Ca-TFSI₂.¹¹⁵ The difference in initial performances of PSCs with the Mg-TFSI₂ and Ca-TFSI₂ to those of PSCs with Li-TFSI was marginal, showing similar V_{OC} and J_{SC} . However,

the steady-state power output (SPO) measured for Mg-TFSI₂ was much greater than PSCs with Li-TFSI, resulting in higher PCEs after light and electrical stresses. Due to the more hydrophobicity of Mg-TFSI₂ and Ca-TFSI₂ than Li-TFSI, the electrical stability of the PSCs was improved. Better performances using Mg-TFSI₂ after external stress to devices resulted from relatively higher V_{OC} which almost retained original performances. This indicates that when considering high V_{OC} in PSCs, V_{OC} after long exposure to light and electrical bias should be considered more important because the PSCs in real use is going to operate continuously during the daytime. In a similar manner to the aforementioned study, Seo et al. recently reported the use of M(TFSI)_n in Spiro-OMeTAD, where M = Li, Zn, Ca, Cu, Sc.¹¹⁴ All these five metallic components used in this study showed sufficiently high performance, higher than Li-TFSI, and similar performance for Ca, Cu, and Sc-TFSI when used in PSCs employing (FAPbI₃)_{0.87}(MAPbBr₃)_{0.13} perovskite. It was expected that redox-active dopants such as Cu(TFSI)₂ would facilitate hole conduction in Spiro-OMeTAD by generating radical cation species. However, the results of Cu-TFSI did not show obvious improvement compared to other metallic components, rather, Zn(TFSI)₂ displayed the highest PCE, owing to the increase of V_{OC} from 1.11 V (Li) to 1.15 V (Zn) (Figure 12d). PL emission spectra revealed that Zn-containing Spiro-OMeTAD led to the minimum value of PL lifetime, implying more effective hole transfer from perovskite to the HTM.

Although it is understood that the kind of dopants in the HTM determine the overall V_{OC} and quite a good amount of work has been done to improve the V_{OC} by choosing suitable dopants, negative effects regarding the long-term stability of the PSCs have been uncovered in most cases. In this regard, attempts have been made to fabricate PSCs without dopants in Spiro-OMeTAD. Methods have been developed to solve the intrinsic problem of extremely low hole mobility of Spiro-OMeTAD without dopants. For instance, replacing the chlorobenzene solvent that is widely used for dissolving spiro-OMeTAD with pentachloroethane has been a relatively simple method to solve the problem.¹¹⁶ Surprisingly, the performances of PSCs based on Spiro-OMeTAD without dopants in pentachloroethane (PCE > 16% for cells with an active area of 1 cm²) were comparable to those of PSCs using Spiro-OMeTAD with dopants in chlorobenzene. High V_{OC} and J_{SC} were simultaneously obtained with even better air stability. The authors claimed that chlorine radicals from pentachloroethane transfer partially to Spiro-OMeTAD and are retained in the HTM layer, resulting in improved conductivity (comparable to the HTM with dopants). Pentachloroethane has also been used by Nishimura et al.¹¹⁷ for checking the performance of newly synthesized π-conjugated small molecules (TOP-HTM-α1, TOP-HTM-α2, TOP-HTM-α3) without dopants. All these HTMs have a lower HOMO level than Spiro-OMeTAD, showing higher V_{OC} than that achieved with the latter, even when they are dopant-free. Though PCEs were higher with the introduction of dopants such as Li-TFSI, the dopant-free π-conjugated HTMs showed adequate performances with better stability. PCEs over 16% were obtained by TOP-HTM-α3 without dopants while only 12.1% was observed for dopant-free Spiro-OMeTAD-based PSCs. Here, pentachloroethane was also used for TOP-HTM-α3 only when dopants were not used while chlorobenzene was used for incorporating dopants in the HTM. The authors found that the use of dopants with pentachloroethane had negative effects in terms of performance,

the mechanism of which was not discussed in the report. However, they observed severe color change of TOP-HTM- α 3 in pentachloroethane-based precursor solutions with dopants. Conclusively, in conjunction with the results regarding dopant-free Spiro-OMeTAD with pentachloroethane, it is conjectured that the positive effect of pentachloroethane on HTM can be seen only when dopants are not used. As HTMs with different molecular structures (Spiro-OMeTAD, TOP-HTM- α 3) displayed similar trends of V_{OC} improvements by pentachloroethane without dopants, further studies regarding various solvents for dopant-free HTMs should be conducted for possible enhancement of PCEs driven by the increase in V_{OC} . Among the three molecules, TOP-HTM- α 1 and TOP-HTM- α 3 are now commercially available so that the researchers can study further on the HTMs.

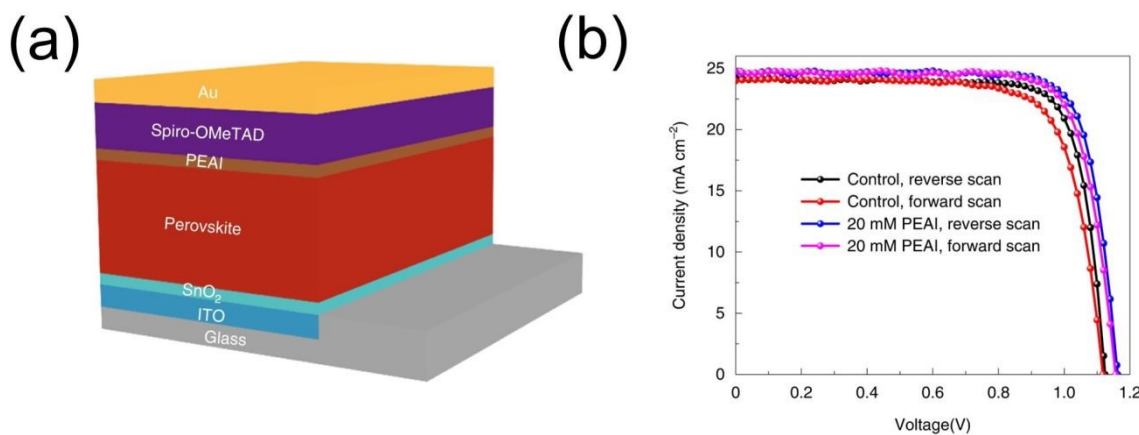


Figure 13 (a) Device structure with phenethylammonium iodide (PEAI) is used for post-treatment of the perovskite surface. (b) J-V curve of the device with PEAI (20 mM) and without PEAI treatment. (a) and (b),¹¹⁸ Reprinted with permission from Nature Publishing Group (2019).

2.3.2 Modification of perovskite/HTM interface

This is well known that the performance of PSCs are/can be significantly altered by changing the HTMs either by using different molecules, different dopants, or even different solvents, as discussed above. All these changes eventually affect the carrier management (i.e. hole transfer and conduction), which is considered a critical factor to enhance V_{OC} . We have discussed the significant role of HTMs regarding carrier (hole) management in the PSCs in conventional structures so far. However, it must be noted that the property of the perovskite/HTM interface, which can be strongly influenced by the surface of perovskite, can also affect the carrier management (hole transfer and interfacial recombination) and ultimately, the device performance remarkably. In our experience, we have often encountered the saturation value of V_{OC} though we have tried various fabrication conditions of HTMs. Many research groups insisted that the reason behind this lies in the fact that defects existing on perovskite surface induce charge trapping at the perovskite/HTM interface thereby limiting the overall efficiency.¹¹⁹⁻¹²³ As the surface passivation of perovskites is a conspicuous approach to overcome this issue, tremendous efforts related to surface passivation have been made. Nazeeruddin et al. developed a perovskite surface passivation strategy using

perhydropoly(silazane).¹²⁴ They demonstrated that this passivation layer regulates the Fermi-level of the perovskite surface, causing band-bending between the surface and bulk of the perovskite, which enhances the hole extraction from perovskite bulk to the HTM side. Using a 1.61 eV hybrid perovskite, the V_{OC} was increased from 1.07 to 1.14 V (efficiency from 20.5% to 22.1%). Later, they reported a similar band-bending strategy with enhanced V_{OC} using an organic polymer.¹²⁵

As a pioneer work, Jiang et al. applied phenethylammonium iodide (PEAI) to the interface between perovskite and Spiro-OMeTAD (Figure 13a).¹¹⁸ The optimum concentration of PEAI dissolved in 2-propanol is 20 mM which led to PCE of over 23% for PSCs based on $FA_{1-x}MA_xPbI_3$ perovskite (1.53 eV). The major contribution to such high PCE was the improvement in V_{OC} recorded at 1.18 V despite the low bandgap of the perovskite (Figure 13b). Interestingly, thermal treatment of PEAI on perovskites degraded performance while PEAI that was not thermally annealed worked better. The authors insisted that the formation of 2-dimensional (2D) perovskites by reacting PEAI with perovskites on thermal treatment is not ideal for the purpose. The exact mechanism for this phenomenon was not fully uncovered in this report but this study triggered passivation engineering using phenethylammonium-based halides due to their ability to form 2D perovskites with the underlying perovskite active layer. Contrary to the above work stating the merit of unannealed PEAI, several other studies insisted that phenethylammonium (PEA) halides (X) with thermal treatments on perovskite layers have a positive impact on overall performances, explained by the decrease in defect density of perovskites by the 2D perovskite formed on top.^{126, 127} Based on these contradicting results, regarding whether thermal treatment of PEAX is effective in the improvement of V_{OC} , the clarification of how PEAX works at the perovskite/charge transport layer interface is important.

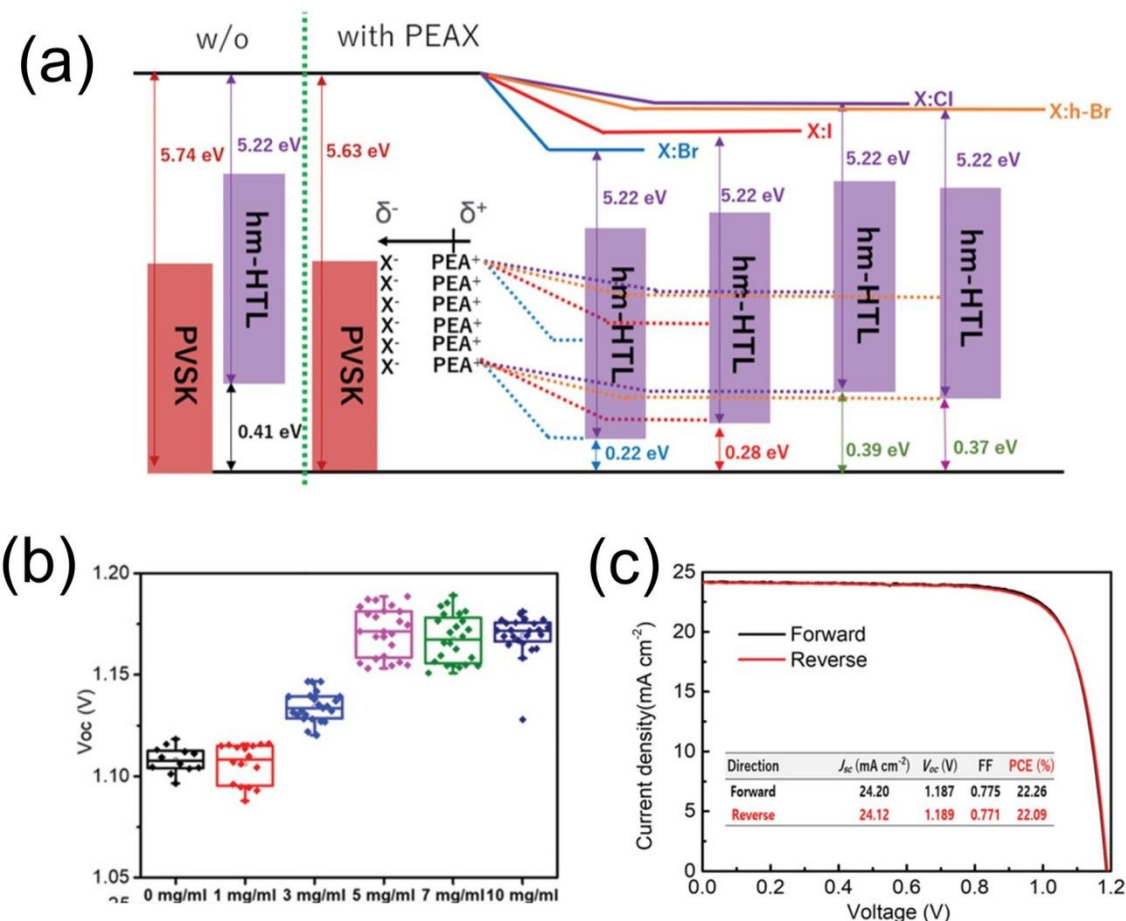


Figure 14 (a) Schematic diagram of the energy level of each layer with the insertion of phenethylamine halides (PEAX). (b) V_{oc} distribution of PSCs for different concentrations of poly(methyl methacrylate) on vacuum dried phenethylammonium bromide (PEABr). (c) J-V curve of the best performance PSC with optimized conditions. (a)-(c),⁶ Copyright 2021, Wiley-VCH.

In a recent study, we attempted to understand this.⁶ To precisely analyze how PEAX works on perovskites, we synthesized novel HTMs (HTM-1, HTM-2) consisting of donor-acceptor-donor (D-A-D)-typed small molecules. The new HTMs were suitable to study the working mechanism of PEAX because the dynamic change in performance of the PSCs based on the HTMs was not pronounced while PSCs with Spiro-OMeTAD showed gradual improvements in PCEs by increasing V_{oc} and FF overtime after fabrication, which is explained by oxidation of Spiro-OMeTAD by exposure to oxygen and air. Interestingly, only high performances were obtained only when PEAX was incorporated between perovskites and the new HTMs. In other words, PSCs using these HTMs without PEAX showed lower performances with PCE of less than 15% due to low FF and V_{oc} . To verify whether PEAX acts as a surface passivator, we carried out PEAX treatment in different ways in our PSCs to create situations where the PEAX does/does not come in contact with the perovskite. The blocking of direct contact of PEAX with the bottom or top layer was done by inserting poly(methyl methacrylate) (PMMA) at the perovskite/PEAX or PEAX/HTM interface.

Surprisingly, the incorporation of PEAX that was neither in direct contact with perovskite nor HTM was also effective in enhancing the overall performances of PSCs, equivalent to PEAX that was directly coated on perovskite surface. This indicated that the working mechanism to enhance V_{OC} by PEAX does not result from passivating perovskite surface. Through the ultraviolet photoelectron spectroscopy (UPS) and Kelvin probe Force Microscope (KFM) measurements, the formation of dipole moments caused by arrangements of cations and anions that PEAX comprises was confirmed (Figure 14a). The degree of dipole moments relies on halide components in PEAX with the order of $\text{Br} > \text{I} > \text{Cl}$, which is following the performances of PSCs with different halides. From the results, it is reasonable to say that the primary factor to performance improvement by the introduction of PEAX is not perovskite surface passivation, but the electric field driven by PEAX at the perovskite/HTM interface. This can explain why PSCs with PEAX perfectly work with the blocking layer at each interface because the dipole moments still exist regardless of PMMA. This, in turn, means that device structure (conventional and inverted PSCs) should be carefully considered when using PEAX as the dipole moments are directional. We also attempted to fabricate inverted PSCs including PEAX and observed that the performance of inverted PSCs with PEAX at the perovskite/PCBM interface was poor (less than 3% PCE), resulting from a significant reduction in V_{OC} , which is also an indicator of the formation of dipole moments. The direction of the electric field induced by the dipole moments created by PEAX is not preferred in inverted structure as the energy level offset between the LUMO level of perovskite and that of ETL enlarges, leading to energy loss during electron transport. As we mentioned earlier, however, the performance improvements were often reported in inverted structure PSCs using PEAX, which is not in accordance with our results. Through scrutinizing experimental sections of these reports, we newly found that all PEAX in inverted structures reported up to now were thermally treated. We conjectured that heat treatment of PEAX on perovskites promotes the formation of 2D perovskites thereby losing dipole moments. Several reports revealed that the formation of 2D perovskites by PEAX effectively blocks penetration of moisture and oxygen into the perovskite layer, improving the stability of devices. Conclusively, when using PEAX in PSCs, we have to approach two mechanisms depending on the structure of PSCs; 1) formation of dipole moments without heat treatment and 2) passivation by 2D perovskite formed by heating. Furthermore, we observed the synergistic effect of PEAX/PMMA at the perovskite/new HTM interface, which might be due to the strong interaction of PEAX with PMMA through hydrogen bonding, increasing the degree of dipole moments and the device V_{OC} (Figure 14b). The champion PCE with this structure recorded 22.26% with 1.19 V of V_{OC} (Figure 14c). Considering the low bandgap (1.51 eV) of perovskite we used, an extra-low E_{loss} (0.32 eV) was accomplished by this HTM interface engineering. Note that the 0.32 eV E_{loss} , to the best of our knowledge, is the lowest energy loss achieved among all kinds of PSCs.

Because several CTLs, such as PTAA and ZnO, can be employed in both normal and inverted configurations, the influence of device configuration on V_{OC} must be considered. Here we take PTAA as an example. In general, PTAA-involved inverted structure is more popular than the normal structure and the former's champion efficiency (23.8%)¹²⁸ is also higher than that of the latter (22.6%).¹²⁹ The energy

alignment of PTAA with perovskite is the same in both normal and inverted structures, and the key concern is the interface contact property. In the normal structure, the PTAA works similarly to Spiro-OMeTAD, where the additives or dopants are necessary to improve the intrinsic low conductivity and the HTM must fully cover the rough perovskite surface. Jia and co-workers, for example, proposed a novel fluorinated iron(III) porphine dopant for PTAA and achieved a V_{OC} of 1.11 V and efficiency of 21.73% using a $(\text{FAPbI}_3)_{0.95}(\text{MAPbBr}_3)_{0.05}$ perovskite.¹³⁰ When used in an inverted structure, PTAA always produces higher V_{OC} and promoted efficiency. For instance, using a 1.59 eV hybrid perovskite, Jen group obtained a remarkable V_{OC} of 1.21 V and a high PCE of 22.31%.¹³¹ In the inverted structure, perovskite is deposited on PTAA and its hydrophobic feature renders the continuous perovskite difficult to produce. However, large perovskite grains (low bulk defects) were formed on the hydrophobic PTAA surface,¹³² which helps to enhance the V_{OC} . The interface between perovskite and PTAA is always modified by an extra layer,^{131, 133, 134} whereas the working mechanism differs depending on the configuration. In the normal structure, the interface modification primarily serves to strengthen hole extraction and suppress carrier recombination. While in the inverted structure, the modification layer additionally guides the perovskite growth, resulting in fewer perovskite defects and a physically continuous heterojunction.¹³¹ Therefore, the effect of device configuration on V_{OC} mainly lies in the perovskite quality and interface contacting properties.

Due to technical challenges such as the wettability of perovskite precursor on HTM, HTMs utilized for inverted PSCs are relatively scarce as compared to the normal structure.¹³⁵ To address these difficulties, new HTMs for inverted PSCs have been recently highlighted. For example, molecules containing carbazole backbones and phosphonic acid (2PACz, MeO-2PACz) have been found to be efficient HTMs in inverted PSCs, with over 21% efficiency.¹³⁶ Unlike conductive polymer and metal oxide HTMs (PEDOT:PSS, PTAA, and NiO_x), these small molecules form self-assembled monolayers (SAM) on different oxides, resulting in an energetically favorable interface between ITO and the perovskite. The superiority of those small molecules was conspicuous for monolithic CIGSe/perovskite tandem solar cells recording 23.26% efficiency on a 1 cm² cell. They also performed excellently on PEDOT:PSS, resulting in high PCE (23.3%) for Pb-Sn mixed (1.25 eV) PSCs due to enhanced V_{OC} (0.88 V).¹³⁷

In summary, for achieving high V_{OC} , research on HTM or perovskite/HTM interface has been focused on the replacement of popular doped Spiro-OMeTAD HTM by new HTMs and optimization of the carrier transfer at the interface. Among these studies, we believe that developing new HTMs and interface modification are more promising for realizing high-performance and stable hybrid PSCs. As we discussed here, the dopants are always necessary for Spiro-OMeTAD, while these dopants are always hygroscopic and diffusive, which will negatively affect the long-term stability of the device.¹³⁸ By developing new HTMs, especially dopant-free HTMs, this problem of dopants can be eliminated. More importantly, people can design new HTMs with proper HOMO levels that can better match the energy levels (VBM) of perovskite materials, reducing the energy loss in the hole transfer from perovskite to HTM. The interface between perovskite and HTM needs more attention because although many interface strategies have been developed, the mechanisms underlying the V_{OC} enhancement are still not clear. A better understanding of

the mechanisms will help us exploit more interfacial engineering that further promotes the V_{OC} and FF, and finally the efficiency of hybrid PSCs.

Although the V_{OC} of the best hybrid PSCs is approaching the S-Q limit, the V_{OC} of PSCs using perovskites with larger bandgap still has room for improvement (Figure 2a). As is most widely studied, it seems every layer of hybrid PSCs is nearly perfect, while the study on the contact interfaces of these stack layers is still inadequate and will be the key to further performance improvement. For instance, Hu et al. used a high work function MoO_3 to modify the $NiO_x/MAPbBr_3$ interface and an atomic ZrO_2 layer to modify the $MAPbBr_3/PCBM$ interface.¹³⁹ With the minimized energy barrier height by MoO_3 and the hole-blocking effect by ZrO_2 (suppressed carrier recombination and enhanced QFLS), the V_{OC} was promoted from 1.101 to 1.653 V. While it is still not high enough regarding the large bandgap of $MAPbBr_3$ perovskite (2.30 eV). As J_{SC} is nearly saturated with $EQE > 90\%$, the main contributions of the recent high-efficiency PSCs are due to V_{OC} and FF. As we discussed earlier, in the attempts of obtaining high V_{OC} , the non-radiative recombination in the device should be suppressed, which also benefits the FF improvement and finally, the PCE. Since the loss in FF is more severe than V_{OC} for hybrid PSCs (Figure 2b), even a small degree of improvement in V_{OC} with low recombination might benefit a lot for FF. The gap between the S-Q limit for hybrid PSCs (i.e. PCE over 30%) and current world-record efficiency (near 26%) will be further narrowed by V_{OC} and FF enhancement.

3 All-inorganic perovskite solar cells

Not all marriages are perfect. Although the marriage between organic and inorganic counterparts leads to magic properties of hybrid perovskites, the issues of instability, especially thermal stability, have been confirmed to arise from the organic part. For instance, $MAPbI_3$ decomposes into lead iodide and organic molecules when exposed to a temperature as low as 80 °C.^{140, 141} Mixing inorganic Cs with the MA and FA can improve the composition and structural stability at a higher temperature (100 °C), but it is still weak upon long-term heating.^{142, 143} Replacing the organic cations entirely with Cs cations is a fundamental solution to the instability problem because of the excellent thermal stability of all-inorganic $CsPbX_3$ ($X = I, Br$) perovskites. It has been proved that the photo-active phase of $CsPbX_3$ is stable over 400 °C, fully eliminating the concern about thermal instability.¹⁴⁴ Snaith group presented the $CsPbI_3$ PSCs for the first time, showing a PCE of 2.9%.¹⁴⁵ Since then, $CsPbX_3$, such as $CsPbI_3$, $CsPbI_2Br$, $CsPbIBr_2$, and $CsPbBr_3$ have been attracting tremendous attention while making rapid progress on PCE that has pushed the champion efficiency over 20% in only about six years.¹⁴⁶⁻¹⁴⁸ This rapid development certainly should be attributed to the techniques and lessons learned from developed hybrid PSCs. However, all-inorganic PSCs are still facing two main challenges. The first challenge lies in stabilizing the photo-active phase (black phase) at room temperature for a longer time. At room temperature, the black phases (α , β , and γ phase) easily transform into photo-non-active yellow phase (non-perovskite, δ phase), which arouses researchers' interest to develop efficient methods for stabilizing the black phase.¹⁴⁸ The second challenge is further enhancing the device's efficiency. By a quick review of the photovoltaic parameters of all-inorganic solar

cells, it can be noticed that the J_{SC} (EQE) and FF are already quite high, comparable with the S-Q limits. For example, J_{SC} of 16.79 and 16.78 mA cm⁻², which were reported by different groups for CsPbI₂Br ($E_g = 1.91$ eV) solar cells,^{149, 150} are even higher than the S-Q limit of around 16.5 mA cm⁻². High FF over 0.80 is easily achieved in many reports, and Xue et al. have achieved even a very high FF of 0.852 for all-inorganic PSCs.¹⁵¹ Whereas, for the V_{OC} , as summarized in Figure 2a, the champion values deviate more from the theoretical V_{OC} than those of narrow bandgap perovskites, implying larger energy loss. This underachieved V_{OC} output is the reason for the gap between the theoretical limit and the achieved efficiency of all-inorganic PSCs. Therefore, a lot of efforts have been made to develop methods for enhancing the V_{OC} , which are summarized in this part.

Different methods have been developed to reduce different recombination types. Trap-assisted SRH recombination in the perovskite bulk has been reduced largely by improving the film quality/morphology, either enhancing the crystallinity or increasing the grain size, or by incorporating additives, and by metal doping. Surface recombination has been reduced by several treatments of the perovskite film surface. Recombination loss at the perovskite/ETL and perovskite/HTM interfaces, which seem to be quite a significant contributor to the overall loss, has been addressed by interface engineering.

3.1 Reducing bulk recombination

3.1.1 Controlling CsPbX₃ perovskite film growth

The crystal growth of all-inorganic perovskites is not fully the same as that of organic-inorganic hybrid perovskites. In the one-step fabrication process of CsPbX₃ perovskite film, the anti-solvent is not necessary while stepwise annealing is often adopted for obtaining high-quality film. For instance, You et al. prepared a uniform and phase pure α -CsPbI₃ film via solvent-controlled growth of the spin-coated precursor film by leaving it to stand by for several ten minutes at room temperature before annealing at high temperature.¹⁵² The DMSO with a high boiling point of 189 °C could not completely escape from the spin-coated film. During the slow solvent evaporation at room temperature, the mass transport is enhanced and the precursor film is transformed from δ -phase to β -phase. Then, the uniform and high-quality pure α -phase CsPbI₃ film is formed after high-temperature annealing (Figure 15a). This stepwise annealing method yields a high PCE of 15.7% with a V_{OC} of 1.08 V, while the direct high-temperature annealing method delivers only 8.58% PCE and 0.91 V V_{OC} (Figure 15b). Similar results have been also reported for stepwise annealing of CsPbI₂Br, CsPb(I_{0.85}Br_{0.15})₃, CsPbIBr₂, and CsPbBr₃.¹⁵³⁻¹⁵⁶

Adding additives to the perovskite precursor for controlling the crystallization process, improving the film quality, and thereby, reducing the bulk defects in CsPbX₃ film is also a method that results in V_{OC} improvement in devices. Meng's group added urea-ammonium thiocyanate (UAT) into the CsPbI₃ precursor and found that NH₄⁺-urea bonding increases the cation size and weakens the Coulombic bondage of SCN⁻, and increasing the coordination ability of SCN⁻ with the Pb-I octahedron.¹⁴⁷ This enhanced coordination improves the film morphology and suppresses defects and the non-radiative charge recombination in the film remarkably, resulting in a champion PCE of 20.08% with V_{OC} enhanced from

1.06 to 1.15 V. Yin et al. reported a π -conjugated small molecule 4-guanidinobenzoic-acid hydrochloride (4-GBACl) serves as a cross-linker to retard the fast crystallization and of CsPbI₂Br and cross-link the neighboring Pb-X framework effectively.¹⁵⁷ This cross-linking inhibited ion migration and the functional groups of the molecule passivated the defects at the grain boundaries and on the surface. With suppressed non-radiative recombination, the V_{OC} was remarkably improved from 1.13 to 1.28 V, accompanied by an enhanced PCE of 15.59%. Recently, ionic liquid started to be used in CsPbX₃ precursors because of their strong interaction with Pb²⁺, through which the crystallization process can be retarded.^{158, 159} The high-quality perovskite film with less defects also promoted the V_{OC} of the cells. In conclusion, careful control of crystallization by optimizing the annealing process and manipulating the intermediate phases is efficacious in obtaining high-quality all-inorganic perovskite films with suppressed non-radiative recombination in the bulk of the film.

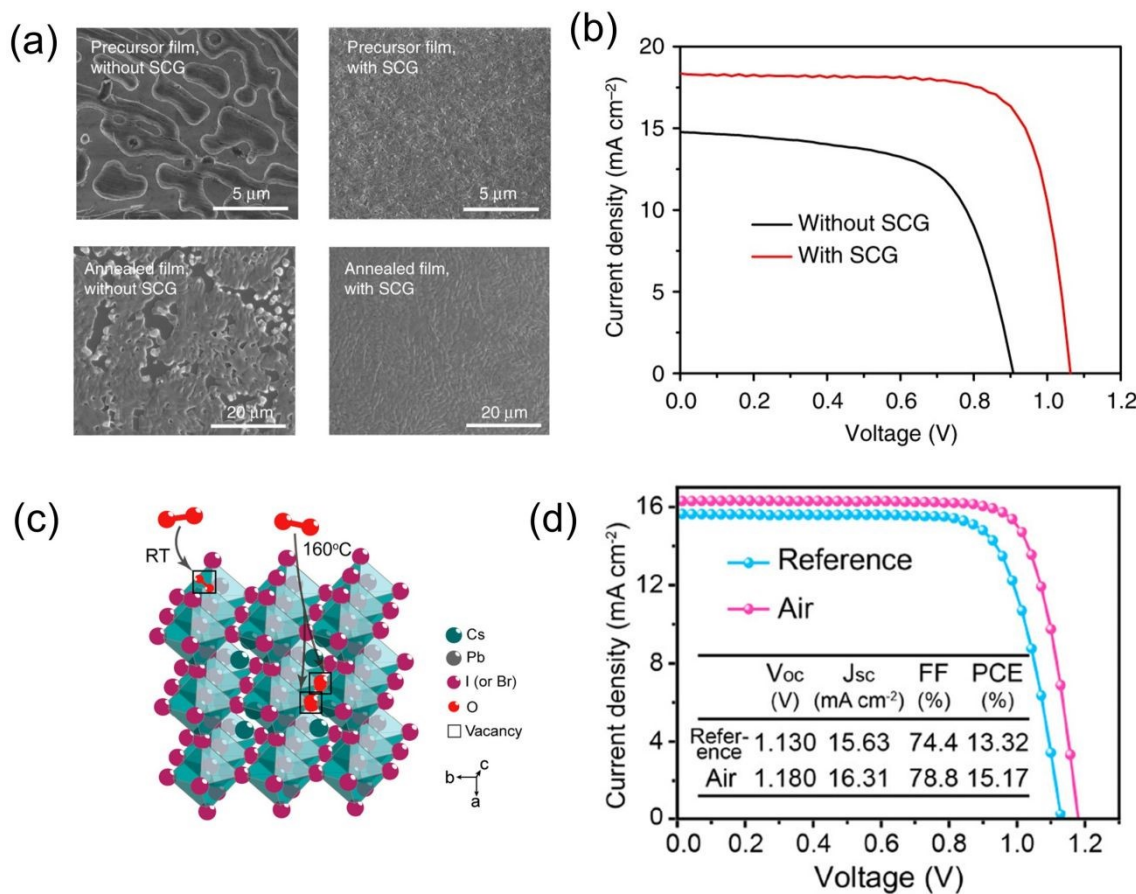


Figure 15 (a) Scanning electron microscopy (SEM) images of CsPbI₃ perovskite precursor films and annealed films without and with solvent-controlled growth (SCG). (b) J-V curves of the devices using CsPbI₃ as the absorber layer, while the CsPbI₃ without and with SCG. (a) and (b),¹⁵² Reprinted with permission from Nature Publishing Group (2018). (c) Schematic of adsorbed oxygen molecule passivation and oxygen atom passivation. (d) J-V curves and photovoltaic performance of the devices fabricated in the air (with oxygen atom passivation) and glove box (reference). (c) and (d),¹⁶⁰ Copyright 2019, American

Chemical Society.

Fabrication condition/environment also has a substantial influence on the carrier recombination in the CsPbX_3 perovskite. Oxygen (O_2) in the ambient environment was proved to act as a passivator of hybrid perovskites, helping to suppress the non-radiative recombination through strongly binding to halide vacancies on the perovskite surface.¹⁶¹⁻¹⁶³ However, O_2 also accelerates the degradation of hybrid perovskites by deprotonating the organic cations of MA^+ or FA^+ , forming MA or FA due to the strong hydrogen bonds between O and organic cations.^{164, 165} Applying oxygen passivation in CsPbX_3 can maintain the positive influence and remove the negative influence because of the organic-free property of the CsPbX_3 perovskites. Hu et al. prepared the O-passivated (rather than O_2) CsPbI_2Br perovskite in dry-air condition (15% RH), where O_2 is dissociated into O during the perovskite annealing process and then gets incorporated into the whole perovskite (Figure 15c), passivating the halide vacancies, which is different from the passivation effect of an oxygen molecule by surface absorption at room temperature.¹⁶⁰ Comparing with the cells fabricated in the glove box (O_2 -free), the defect density and non-radiative recombination in the device prepared in the dry-air condition were efficiently reduced and the V_{OC} was improved from 1.13 to 1.18 V with an efficiency promotion to 15.17% (Figure 15d). The importance of dry air in realizing oxygen atom passivation was also proved by the work of Liu's group.¹⁶⁶ Specifically, the developed in-situ hot oxygen cleansing passivation method for $\text{CsPb}(\text{I}_{2.85}\text{Br}_{0.149}\text{Cl}_{0.001})$ film only works well in the low humidity of 10-20% and it does not work in higher humidity conditions (over 30%). Except for reducing defects and passivating halide vacancies by forming a Pb-O bond, this treatment can also promote the removal of dimethylammonium (formed by the reaction between hydroiodic acid additive and DMF solvent), avoiding its deterioration in device performance and stability. Finally, the PCE was increased from 17.15% (in the glove box) to 19.65% (in dry-air) with the V_{OC} enhancement from 1.14 to 1.23 V. This indicates that in studies where people have fabricated all-inorganic PSCs in dry-air condition,^{16, 167} although they didn't deliberately take advantage of oxygen atom passivation, the passivation is possibly working for promoting the device performance.

3.1.2 Metal doping to CsPbX_3 perovskite

Suppression of the non-radiative recombination in CsPbX_3 films can also be realized by metal doping. Up to now, lots of metal ions have been incorporated into the CsPbX_3 materials and Pb-site doping is more popular than those for Cs-site and X-site.¹⁶⁸ Except for the effect of stabilizing the black phase of CsPbX_3 ,^{168, 169} metal doping also plays role in reducing the defects and improving the device performance. With the same valence state and similar properties, Sn^{2+} and Ge^{2+} were employed to dope into CsPbX_3 and substitute Pb^{2+} . For instance, a Pb/Sn mixed inorganic perovskite, $\text{CsPb}_{0.9}\text{Sn}_{0.1}\text{IBr}_2$, was developed by replacing 10% PbBr_2 with SnBr_2 in the CsPbIBr_2 precursor.¹⁷⁰ The bandgap of CsPbIBr_2 perovskite was reduced from 1.90 to 1.79 eV, which is easily seen from the color change of the films (Figure 16a). Using carbon as the electrode, a high V_{OC} of 1.26 V, and PCE of 11.33% have been achieved for $\text{CsPb}_{0.9}\text{Sn}_{0.1}\text{IBr}_2$ solar cells while only 1.08 V V_{OC} was obtained for wider bandgap CsPbIBr_2 (Figure 16b), which indicates that the defect density and the recombination in perovskite were highly suppressed by Sn^{2+} doping. However, the

bandgap (1.90 eV) of CsPbIBr_2 reported in this study was different from those in other reports (over 2.0 eV) and was matching iodine-rich CsPbX_3 perovskite. It means the perovskite composition here needs to be further confirmed. Germanium ion (Ge^{2+}), in the same main group with Pb and Sn, was also doped into an all-inorganic CsPbI_2Br perovskite.¹⁷¹ A V_{OC} of 1.27 V and PCE of 10.8% was achieved for $\text{CsPb}_{0.8}\text{Ge}_{0.2}\text{I}_2\text{Br}$ based solar cells, in comparison to 1.02 V and 5.3% for pristine CsPbI_2Br cells. Moreover, a higher V_{OC} of 1.32 V was obtained for $\text{CsPb}_{0.7}\text{Ge}_{0.3}\text{I}_2\text{Br}$ based devices but it suffered from J_{SC} and FF loss, showing a poorer PCE of 9.0%. Although Sn^{2+} and Ge^{2+} can substitute Pb^{2+} due to the similarity in element properties, the oxidation of Sn^{2+} and Ge^{2+} to respective +4 oxidation states, which is inevitable, and especially its effect on device performance and stability needs to be understood well. In Sn/Ge-mixed perovskites, Padture et al. proved that a native oxide layer of GeO_2 doped with a small portion of Sn was formed on $\text{CsSn}_{0.5}\text{Ge}_{0.5}\text{I}_3$ perovskite film as soon as it was exposed to air.¹⁷² This native oxide layer not only encapsulates the perovskite from moisture but also suppresses the recombination of carriers at the interface between perovskite and HTM. Therefore, it is believed a similar tin oxide or germanium oxide layer can be formed in Sn^{2+} or Ge^{2+} doped CsPbX_3 perovskites, which contributes to enhanced V_{OC} output.

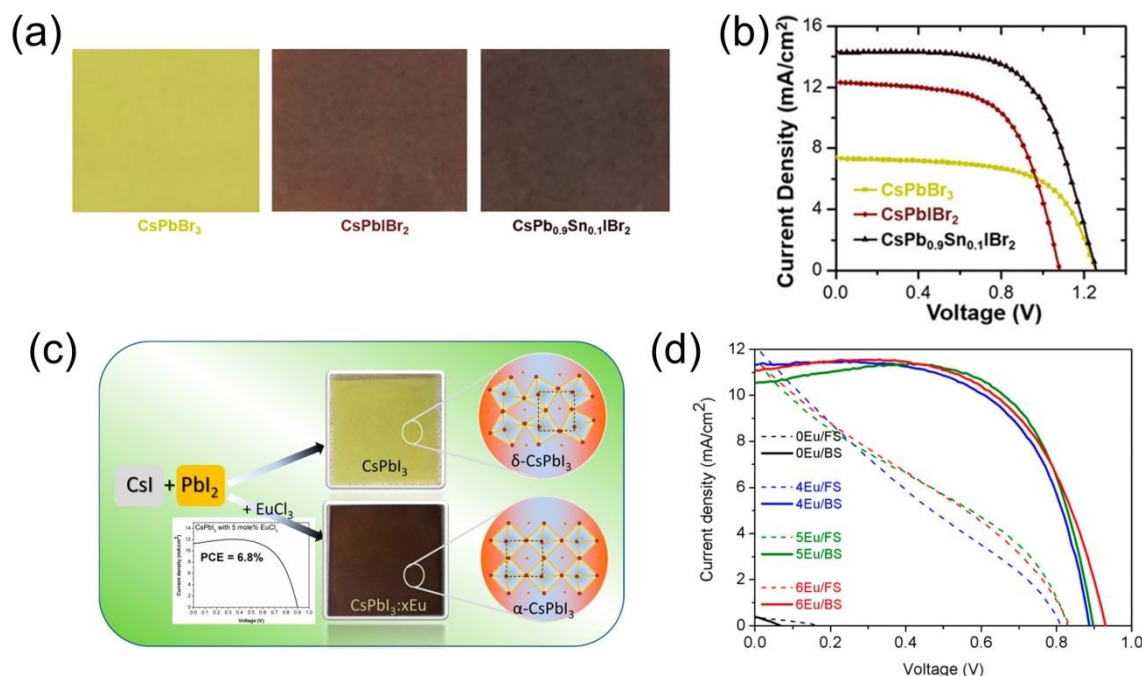


Figure 16 (a) Optical images of CsPbBr_3 , CsPbIBr_2 , and $\text{CsPb}_{0.9}\text{Sn}_{0.1}\text{IBr}_2$ films and (b) J-V curves of the corresponding devices.¹⁷⁰ Copyright 2017, American Chemical Society. (c) Schematic illustration of $\alpha\text{-CsPbI}_3$ phase stabilization by incorporation of Eu^{3+} . (d) J-V curves of a set of $\text{CsPbI}_3:\text{xEu}$ cells with 4, 5, and 6 mol % EuCl_3 . (c) and (d),¹⁷³ Copyright 2018, American Chemical Society.

Other divalent metal ions such as Mn^{2+} , Sr^{2+} , Mg^{2+} , Ba^{2+} , Fe^{2+} , Zn^{2+} , and Eu^{2+} have been proved to be a substitution of Pb^{2+} and helpful for promoting the device V_{OC} output due to the suppressed non-radiative recombination.¹⁷⁴⁻¹⁸¹ Differently, Hagfeldt and co-workers demonstrated that Ba^{2+} can't be incorporated into the CsPbI_2Br lattice. Instead, it segregates into Ba-based non-perovskite phases (Br-rich), leaving a

perovskite with more iodide and a smaller bandgap. Specifically, with 20% Ba²⁺ (vs. Pb²⁺), the E_g of the initial CsPbI₂Br (1.92 eV) decreased to 1.86 eV, identical to that of CsPbI_{2.27}Br_{0.73}. Here, the iodide-rich perovskite acts as the light-harvesting species whereas the Ba-based non-perovskite phases, located at the surface or grain boundaries, prohibit non-radiative recombination in perovskite. Therefore, although the addition of Ba results in smaller E_g of perovskite with lower theoretical V_{OC}, it leads to a significant improvement in V_{OC}, from 1.12 V for undoped CsPbI₂Br cells to 1.33 V for Ba-doped CsPbI₂Br. Phase segregation of mixed-halide perovskites into iodide-rich and bromide-rich domains is a challenge for the cells working under continuous light irradiation.^{182, 183} The iodide-rich domains always act as the recombination center and deteriorate the device performance. Nevertheless, in the case of Ba²⁺ induced phase segregation, an enhanced performance was achieved. One possible reason is that the light-induced phase segregation is different from that of Ba²⁺-induced segregation. Another reason can be the passivation effect of Ba-based non-perovskite phases, turning the negative effect of iodide-rich perovskite into a positive role. The positive effect of Ba-based non-perovskite phases has been confirmed by enhanced performance, while how they reduce the carrier recombination and boost V_{OC} output needs further investigation. Except for divalent metal ions, some trivalent ions have also been incorporated into CsPbX₃ perovskites. For instance, incorporation of Bi³⁺ to CsPbI₃ perovskite has been reported to partially substitute Pb²⁺ and the extra charge is compensated by a slightly larger iodine component.¹⁸⁴ The smaller size of Bi³⁺ causes the larger τ and micro-strain in perovskite by lattice distortion, which stabilizes the α-CsPbI₃ at room temperature. Moreover, an enhanced PCE of 13.21% with a V_{OC} of 0.97 V was achieved in the CsPb_{0.96}Bi_{0.04}I₃ solar cell, much better than the control sample (8.07% and 0.89 V). However, a recent work proposed that CsPb_{0.96}Bi_{0.04}I₃ is not a thermodynamically favored black phase system, though it has a larger τ.¹⁸⁵ CsPb_{0.96}Bi_{0.04}I₃ with compositional disorder and crystal strain can transform to Cs₄PbI₆ under the activation of enough thermal energy. Hence, the stabilization of the CsPbI₃ black phase by Bi³⁺ incorporation can be mainly because of the tailored colloid size in the solvent system. Following the Bi³⁺ doping, many other trivalent metal ions including Sb³⁺, In³⁺, Y³⁺, and lanthanide ions have been incorporated into CsPbX₃ with a positive effect on V_{OC} and efficiency of the solar cells.¹⁸⁶⁻¹⁸⁹ Our group firstly explored the inclusion of Eu³⁺ into CsPbI₃ and examined its effect on the stabilization of the perovskite phase and photovoltaic properties of devices.¹⁷³ We found that the addition of a certain amount of EuCl₃ into the precursor of CsPbI₃ stabilizes the perovskite phase at room temperature and in ambient conditions while the reference shows a fully δ-CsPbI₃ at the same temperature (Figure 16c). Eu³⁺-incorporated CsPbI₃ PSCs showed a PCE over 6.0% with V_{OC} over 0.8 V (Figure 16d). In very recent work, we confirmed that Eu incorporation promotes the formation of γ-CsPbI₃ at a low temperature of 80 °C.¹⁹⁰ The main roles of Eu in CsPbI₃ are 1) assisting the formation of the γ-phase either by substituting Pb or by occupying interstitial positions in the CsPbI₃ lattice; 2) indirectly promoting the formation of fine grains wherein the high surface-to-volume ratio makes the establishment of the δ-phase unfavorable. Liu et al. have taken the advantages of Eu³⁺ and acetate (Ac⁻) by incorporating Eu(Ac)₃ into CsPbI₂Br perovskite to not only improve the CsPbI₂Br film quality but also increase the built-in potential, resulting in V_{OC} improvement.¹⁹¹ They proposed an interesting conclusion that Pb²⁺ was substituted with Eu³⁺ while I⁻ was

replaced with Ac^- . These researches indicate that CsPbX_3 perovskite has quite high tolerability to metal ions with different valences, even though many questions about metal doping remain unanswered. In an attempt to answer the question about the crystal site of the location of the metals, Kim et al proposed that the divalent metal cations stabilize the α -phase of CsPbI_3 by replacing the Pb^{2+} , while trivalent cations stabilize the β -phase of CsPbI_3 by inducing stress on the crystal lattice, rather than replacing the Pb^{2+} sites.¹⁹² This may apply to trivalent and pentavalent ion incorporation, which were proved to be effective while the working mechanism was unclear.^{156, 193} In addition, monovalent cations tuning is also helpful to increase the device V_{OC} output. For example, Tang's group doped a variety of alkali metal ions (Li^+ , Na^+ , K^+ , and Rb^+) into the CsPbBr_3 perovskite.¹⁹⁴ Here, the dopants are supposed to enter the interstitial site and prevent the formation of defects in perovskite.^{194, 195} The perovskite crystal size is also enlarged, leading to a suppressed trap-dominated recombination. Besides, the energy level of perovskite can be tuned by mixing A-site ions, through which the energy barrier can be reduced and the recombination can be eliminated. The champion V_{OC} of 1.514 V was achieved using the $\text{Cs}_{0.92}\text{K}_{0.08}\text{PbBr}_3$ based solar cells with a PCE of 8.61%. Rb^+ doping into CsPbI_2Br was also studied, where Rb^+ is responsible for higher perovskite film quality, resulting in a high V_{OC} of 1.32 V and PCE of 17.16%.¹⁹⁶

From the above discussion, we can conclude that metal doping always benefits the CsPbX_3 cells by suppressing the non-radiative recombination and enhancing the V_{OC} output. However, how they interact with the perovskite host and how the valence state, electronegativity, and size of the metal ions generally affect the non-radiative recombination in perovskite need to be understood.

3.1.3 Constructing 2D/3D heterostructure

The construction of 2D/3D heterostructure has also been regarded as a useful strategy for suppressing trap states of 3D perovskite. For instance, You's group added PEAI and $\text{Pb}(\text{OAc})_2$ into the CsPbI_3 precursor to form 2D perovskite of $\text{PEA}_2(\text{CsPbI}_3)_{n-1}\text{PbI}_4$ (Figure 17a), which remarkably promoted the V_{OC} to a record-value of 1.32 V (Figure 17b).¹⁷ The 2D/3D heterostructure can be realized by mixing the precursors. But, it is difficult to obtain the structure by post-treatment of crystallized 3D CsPbX_3 perovskite because unlike in the case of hybrid perovskites, Cs would not exchange with the long-chain alkyl-ammonium halide cation spin-coated onto the crystallized 3D perovskite.¹⁹⁷ Addressing this issue, Lin's group demonstrated an *in-situ* growth method to form a 2D/3D heterostructure based on inorganic CsPbI_2Br perovskite.¹⁹⁸ In this method, 1 vol% dimethyl sulfoxide (DMSO) was added to the butylammonium iodide (BAI) solution that was spin-coated on CsPbI_2Br . During the spin-coating process, DMSO would dissolve a thin layer of the crystallized 3D CsPbI_2Br film and facilitate the cation exchange process between BAI and Cs to form only a thin layer of 2D $\text{BA}_2\text{CsPb}_2\text{I}_6\text{Br}$ perovskite on the surface of 3D CsPbI_2Br perovskite (Figure 17c). They found that this 2D/3D heterojunction promotes hole extraction and suppresses charge carrier recombination, resulting in higher V_{OC} and efficiency (Figure 17d).

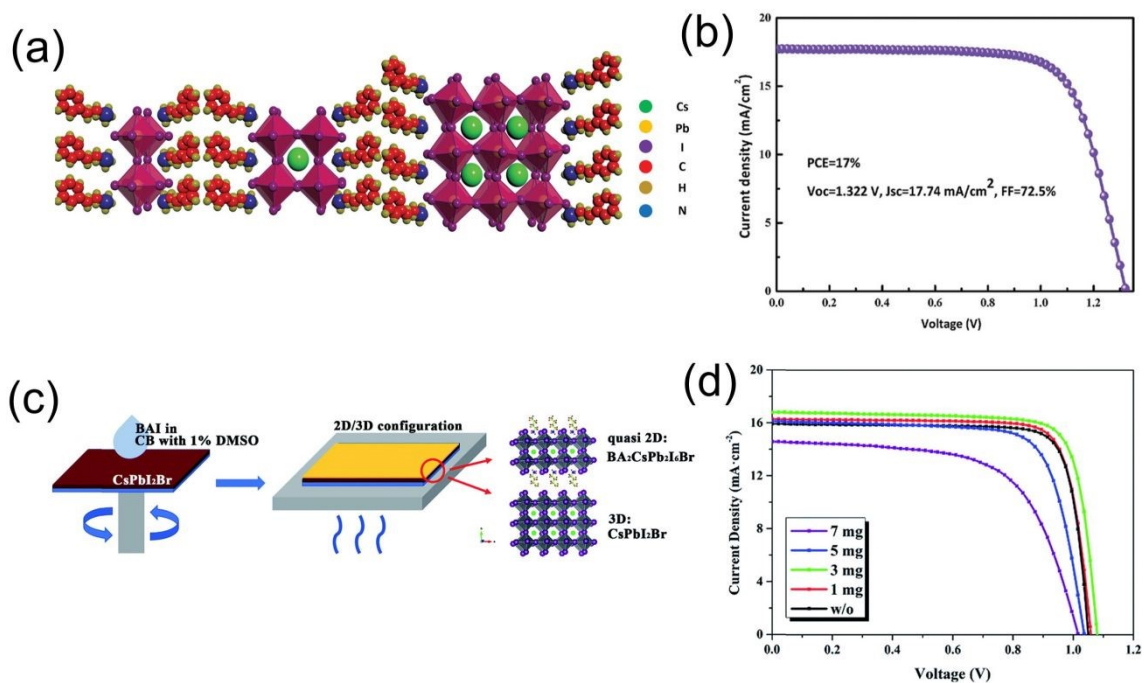


Figure 17 (a) Schematic illustration of 3D perovskite with quasi-2D perovskite composition. (b) J-V curve of the PEA-CsPbI₃ (2D/3D) based champion device. (a) and (b),¹⁷ Copyright 2020, Wiley-VCH. (c) Schematic illustrations of the BAI treatment procedure and 2D/3D bilayer configuration. (d) J-V curves of devices based on pristine and 1, 3, 5, and 7 mg BAI treated CsPbI₂Br films. (c) and (d),¹⁹⁸ Copyright 2019, Royal Society of Chemistry.

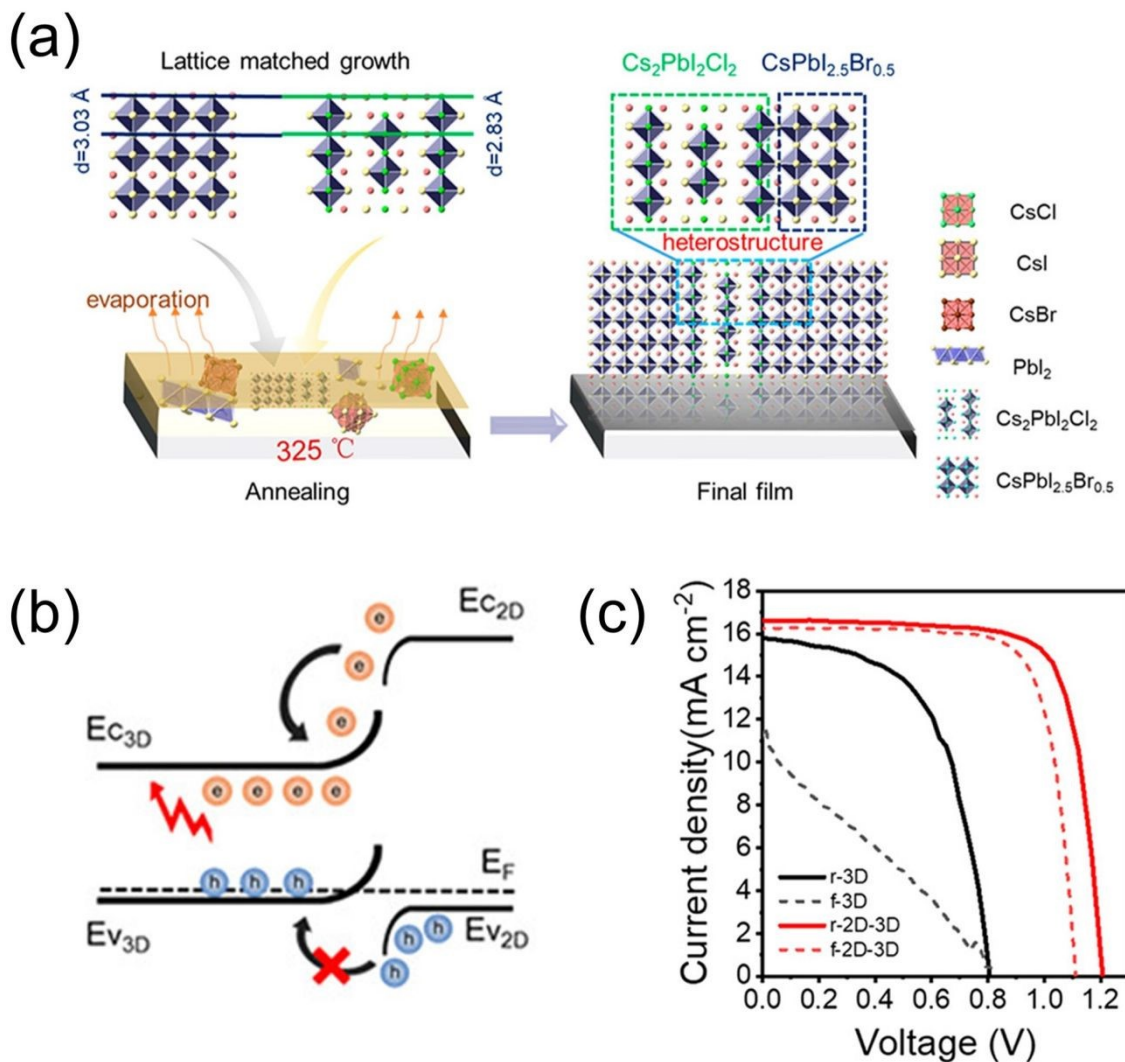


Figure 18 (a) Schematic depicting the processes used to generate the $\text{Cs}_2\text{PbI}_2\text{Cl}_2$ - $\text{CsPbI}_{2.5}\text{Br}_{0.5}$ film. (b) Schematic depicting the band bending for the 2D-3D heterojunction under illumination. (c) J-V curves of the 3D and 2D-3D based PSCs. (a)-(c),¹⁹⁹ Copyright 2020, American Chemical Society.

Compared with the organic-cation-based 2D perovskite, inorganic 2D perovskite is easier to be incorporated into the 3D CsPbX_3 perovskite. A $\text{Cs}_2\text{PbI}_2\text{Cl}_2$ - $\text{CsPbI}_{2.5}\text{Br}_{0.5}$ 2D/3D mixed-dimensional perovskite film was prepared by adding CsCl and extra amount of PbI_2 into the $\text{CsPbI}_{2.5}\text{Br}_{0.5}$ precursor.¹⁹⁹ The Ruddlesden-Popper (RP) type 2D $\text{Cs}_2\text{PbI}_2\text{Cl}_2$ has a good lattice matching with the $\text{CsPbI}_{2.5}\text{Br}_{0.5}$, giving rise to the (100) preferential crystal orientation (Figure 18a). The lattice match between two crystals favored defect passivation and the suppression of non-radiative recombination within the films, and the (100) orientation of the perovskite facilitated the carrier transport (Figure 18b). The V_{OC} of the $\text{CsPbI}_{2.5}\text{Br}_{0.5}$ ($E_g=1.82\text{ eV}$) solar cells was remarkably improved from 0.81 V to 1.21 V after the introduction of the 2D $\text{Cs}_2\text{PbI}_2\text{Cl}_2$, as well as efficiency enhanced from 7.30 to 15.09% (Figure 18c). A 2D-3D-2D heterojunction was constructed by coating 3D CsPbI_2Br on top of 2D $\text{Cs}_2\text{PbI}_2\text{Cl}_2$ nanosheet modified TiO_2 and then coating a layer of $\text{Cs}_2\text{PbI}_2\text{Cl}_2$ on CsPbI_2Br .²⁰⁰ It was found that the Cl of $\text{Cs}_2\text{PbI}_2\text{Cl}_2$, located both under and above

CsPbI_2Br , can diffuse from 2D nanosheets to 3D perovskite, resulting in Cl doping to CsPbI_2Br , which is responsible for the passivation of perovskite surface trap states. Moreover, the 2D nanosheets notably altered the surface energy level of both TiO_2 and 3D perovskite, which is thought to facilitate the interface charge transfer. The device performance was improved, while the working mechanisms, such as how Cl diffusion from 2D nanosheets to perovskite happens and how it sharply changes the energy level of ETL and perovskite, still need in-depth discussion. Moreover, the properties of the $\text{Cs}_2\text{PbI}_2\text{Cl}_2/\text{CsPbI}_2\text{Br}$ interface including the lattice matching are also important since an imperfect interface may have a reverse effect. A dimensionally graded (3D-2D-0D) heterojunction, e.g. CsPbI_2Br exists as bulk, nanosheet, and quantum dots has also been constructed.²⁰¹ This unique heterojunction, depending barely on dimension rather than hetero-materials, displayed improved V_{OC} of 1.19 V from 1.11 V for pure 3D perovskite cells, as a result of better energy level alignment. However, the judicious design of the heterostructures is critical since inappropriate configuration may impede the charge transport across the device, lowering the efficiency.²⁰²

3.2 Minimizing perovskite surface and interface recombination

In addition to bulk recombination, interface non-radiative recombination is a significant source of energy loss. For suppression of this recombination in the CsPbX_3 solar cells, efforts have been made to modify the perovskite surface, optimize the contact quality between perovskite and CTL, and tune the interface energy level alignment. The perovskite surface, differing from the bulk composition and morphology, is enriched with undercoordinated ions or mobile species.^{33, 203} These defects could introduce electronic trap states that act as the fast channels for the non-radiative charge recombination, causing energy loss and poor V_{OC} output.²⁰⁴ Recently, an increasing number of works have been dedicated to addressing the issue of recombination at the perovskite surfaces.²⁰⁵⁻²⁰⁷ CsPbX_3 PSCs, with serious energy loss, definitely need effective perovskite surface passivation to reduce the non-radiative recombination.

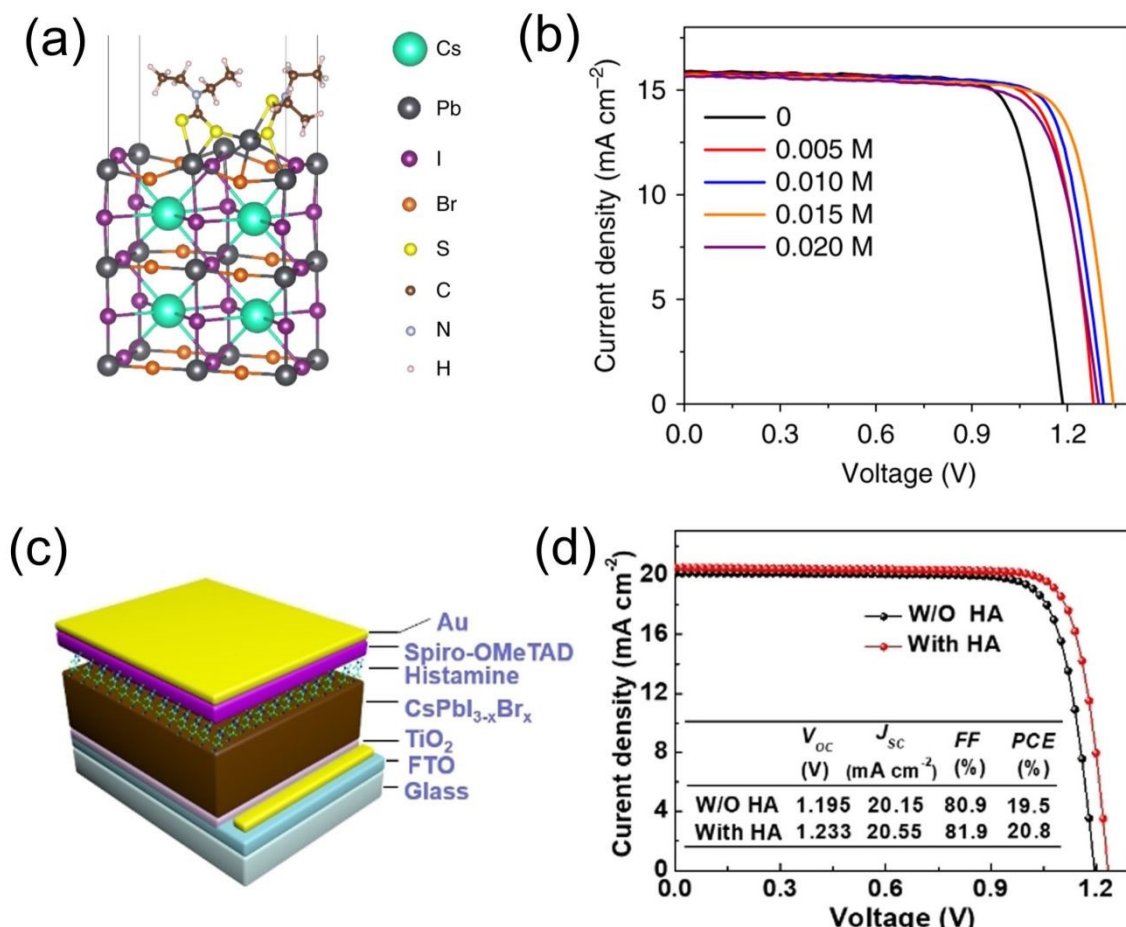


Figure 19 (a) Atomic structure of optimized CsPbI₂Br (001) surface with lead diethyldithiocarbamate (Pb(DDTC)₂) molecule. (b) J-V curves of PSCs with different concentrations of Pb(DDTC)₂. (a) and (b),²⁰⁸ Reprinted with permission from Nature Publishing Group (2020). (c) Device structure and (d) J-V curves of the devices with and without histamine (HA) passivation.²⁰⁹ Copyright 2021, Wiley-VCH.

Hou and co-workers introduced the diethyldithiocarbamate (DDTC) molecule as a chelating agent for the surface engineering of CsPbI₂Br perovskite.²⁰⁸ It was found that the DDTC molecule strongly coordinates to surface Pb cation via a bidentate chelating bonding (Figure 19a). Such chelating structure enabled excellent and persistent passivation of surface defects of perovskite, generating significantly enhanced efficiency of 17.03% for CsPbI₂Br solar cells with a V_{OC} of 1.34 V (Figure 19b). A champion V_{OC} of 1.37 V was achieved with the PCE of 16.51%, indicating highly suppressed recombination after the DDTC molecule passivation. Liu and co-workers' study proved that the predominant defect on the surface of CsPbX₃ is iodine vacancy.²⁰⁹ For passivating the vacancy, they used histamine for perovskite surface post-treatment (Figure 19c). The histamine bonded to the iodine vacancy via a Lewis-base-acid interaction, which was further strengthened by the formed hydrogen bond. The number of undercoordinated Pb²⁺ and Pb clusters was also reduced. With the passivation of undesirable surface trap density and the facilitation of interfacial hole transfer, the histamine post-treatment improved the V_{OC} from 1.195 to 1.233 V and boosted the PCE to 20.8% (Figure 19d), which is the highest efficiency for CsPbX₃ PSCs. Jen and co-

workers developed a passivation strategy by using a Lewis base, π -conjugated 6TIC-4F, for $\text{CsPbI}_x\text{Br}_{3-x}$ film.²¹⁰ The 6TIC-4F was dissolved into the antisolvent and spin-coated onto the perovskite film during the perovskite coating process. The molecule exists at the surface and the grain boundaries of $\text{CsPbI}_x\text{Br}_{3-x}$ film, with a gradient distribution with the highest concentration at the perovskite surface. The electron-rich CN group in 6TIC-4F interacts with the exposed Pb on the perovskite surface through coordination bonds to passivate the trap states and delocalize the valence electron density from the Pb-exposed surface to bulk (Figure 20a and b), which is beneficial for suppressing the non-radiative recombination. Meanwhile, the LUMO of 6TIC-4F creates a better energy-level alignment between CB of perovskite and ZnO in an inverted device structure (Figure 20c) and thereby, improves the charge extraction. With the passivation, the efficiency was improved from 13.69% ($V_{OC}=1.10$ V) to 16.10% ($V_{OC}=1.16$ V) for an inverted structure $\text{CsPbI}_x\text{Br}_{3-x}$ ($E_g=1.78$ eV) solar cell (Figure 20d). Hayase et al. reported the usage of delocalized organic ammonium molecules for passivation of the CsPbI_2Br surface.²¹¹ They found that the amino-thiazolium iodide containing sulfur atoms can effectively passivate defects arising from vacancies of halide ions or Cs^+ on perovskite surface, suppressing trap-assisted recombination. Moreover, the π -electrons from delocalized molecules could occupy the vacuum orbitals of lead atoms, which promoted the charge extraction from perovskite to HTM. As a consequence, the V_{OC} of the fabricated solar cells was improved from 1.10 V to 1.19 V by the passivation process. Tang et al. inserted a layer of multicarbazolyl-substituted benzonitrile (4t-5CzBn) between CsPbI_2Br and Spiro-OMeTAD to tune the interfacial energy level alignment.²¹² The 4t-5CzBn with an intermediate energy level could form a uniform stepped interfacial energy level structure, which is helpful to reduce the E_{loss} and boost the hole extraction. The best device showed a high V_{OC} of 1.335 V and a PCE of 17.34%.

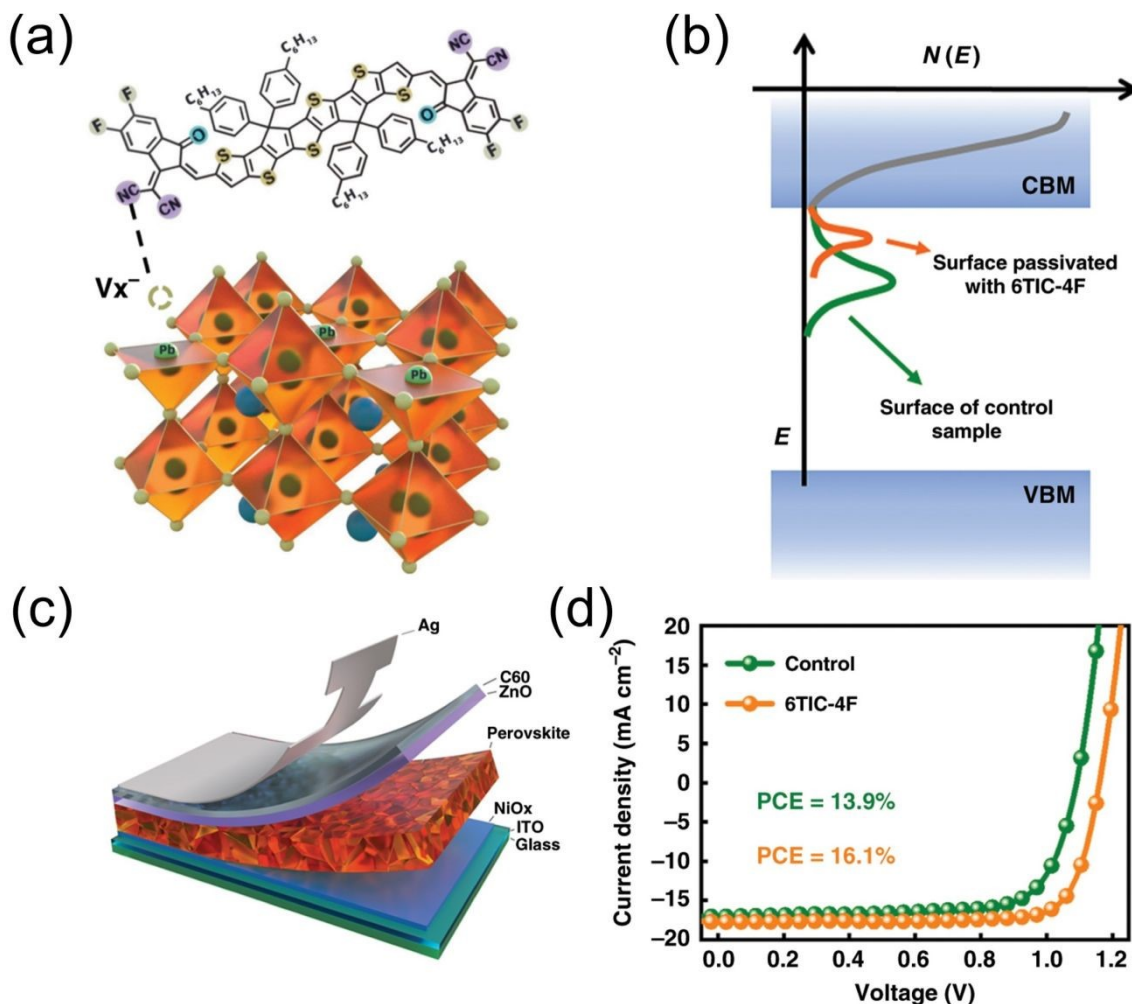


Figure 20 (a) Illustration of possible passivation mechanism of 6TIC-4F and potential interaction sites on perovskite. (b) Energy-level diagram of the trap states passivation by 6TIC-4F. (c) Device architecture of the inverted $\text{CsPbI}_x\text{Br}_{3-x}$ PSC and (d) J-V curves of the champion PSCs with (orange) and without (green) 6TIC-4F passivation. (a)-(d),²¹⁰ Reprinted with permission from Nature Publishing Group (2020).

As a popular surface passivator in hybrid perovskites, PEAI was also studied in CsPbI_3 solar cells.^{118, 197} Unlike forming a 2D perovskite layer in the case of hybrid perovskites,²¹³ the PEAI can only contribute to forming an organic cation surface termination of the CsPbI_3 surface. A modified PEAI molecule, 4-trifluoromethyl phenethylammonium iodide, has been also reported to passivate the surface of CsPbI_2Br perovskite.²¹⁴ Here, an enhanced V_{OC} of 1.23 V and extremely high FF of 84.65% were obtained after passivation. The enhanced V_{OC} was attributed to the interaction between F and Pb, which reduces the trap density and non-radiative recombination of the perovskite surface.²¹⁵ Several other organic iodides have been studied working as surface passivation for all-inorganic perovskites. For example, Zhao et al. reported the passivation of the CsPbI_3 surface by choline iodide, which has been used previously in hybrid perovskites.^{32, 216} This surface passivation boosted the V_{OC} of $\beta\text{-CsPbI}_3$ solar cells from 1.05 to 1.10 V, and PCE from 15.1 to 18.4%, which is attributed to the increased charge-carrier lifetime and the improved

energy-level alignment between the perovskite and CTls. The surface treatment of CsPbI_3 with phenyltrimethylammonium bromide (PTABr) forms a Br-richer phase at the surface through the Br/I halide exchange.²¹⁷ In addition, the PTA organic cation plays a role in surface passivation, leading to better charge transport and decreased charge recombination. As a result, the PTABr- CsPbI_3 solar cell showed a high PCE of 17.06% with a V_{OC} of 1.10 V, surpassing the performance of the control device (13.59% and 1.05 V). Similarly, guanidinium bromide (GABr) post-treatment formed a Br-rich region on the CsPbI_2Br surface, which reduced the defects, accelerated the hole extraction, and regulated the Fermi level of perovskite to achieve better band matching with HTM.²¹⁸ As a result, the champion device exhibited a high V_{OC} of 1.31 V and an efficiency of 16.97%. Some other halides, such as phenyltrimethylammonium chloride²¹⁹ and octylammonium iodide¹⁴⁶ were also proved to be useful in reducing the perovskite surface defects and promoting device V_{OC} .

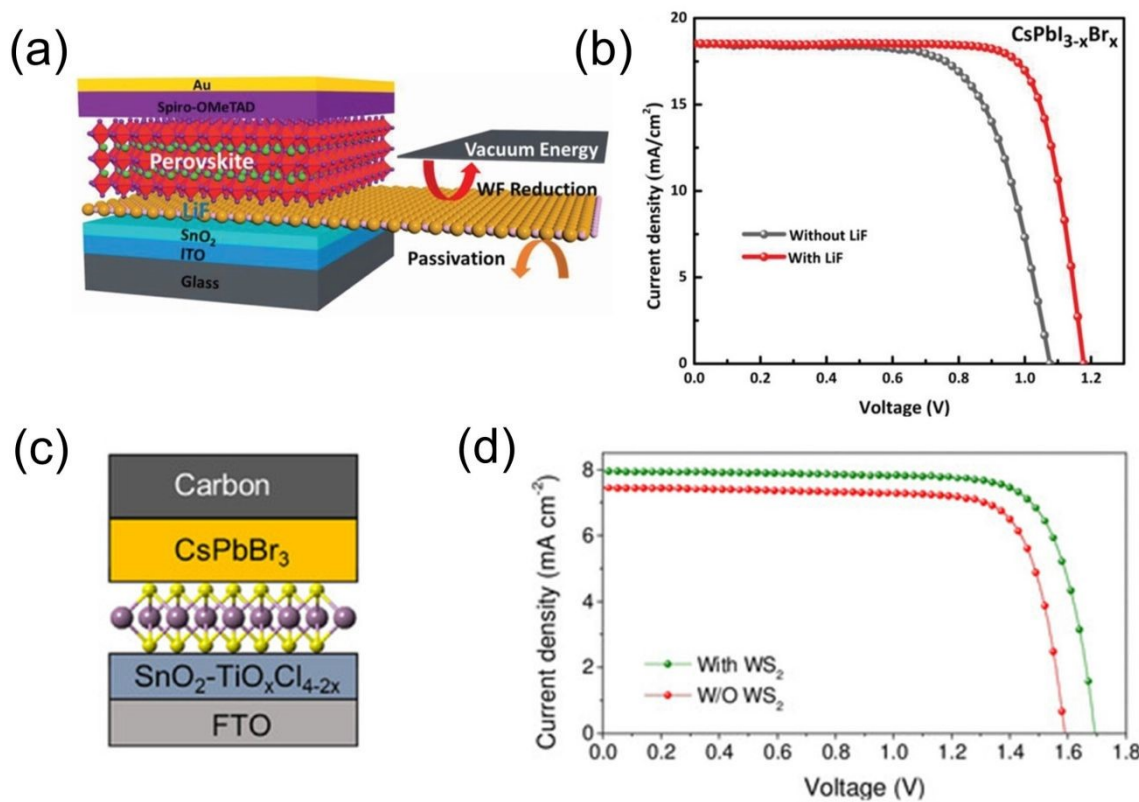


Figure 21 (a) The scheme of device architecture of the $\text{CsPbI}_{3-x}\text{Br}_x$ PSCs; LiF was used to modify the SnO_2 surface. (b) J-V curves of PSCs with and without LiF interlayer. (a) and (b),²²⁰ Copyright 2019, Wiley-VCH. (c) Schematic diagram of an all-inorganic CsPbBr_3 PSC; WS_2 is an interlayer between ETL and perovskite. (d) J-V curves of PSCs with and without WS_2 modification. (c) and (d),²²¹ Copyright 2020, Wiley-VCH.

Besides the organic molecules summarized above, some inorganic thin layers have been also introduced to modify the interface. You's group introduced an insulated shunt-blocking layer of lithium fluoride (LiF) on top of the SnO_2 ETL (Figure 21a) for interface defect passivation and better energy level alignment with

CsPbI_{3-x}Br_x perovskite ($E_g=1.77$ eV).²²⁰ The high work function of LiF enhanced the built-in potential within the device and reduced the interfacial recombination. Consequently, the V_{OC} increased from 1.08 to 1.18 V while the FF improved from 67.89% to 78.26%. Furthermore, when a proper amount of PbCl₂ was added to perovskite, the V_{OC} and efficiency were further improved to 1.25 V and 18.64% respectively (Figure 21b), as a result of improved film crystallinity and suppressed charge recombination in perovskite. This work emphasized again the equal importance of interface and perovskite bulk recombination in determining the V_{OC} output of a solar cell. Brabec and co-workers proposed that, in CsPbI₃ solar cells, the defects at the interface are evenly distributed on the SnO₂ surface, whereas the defects in the bulk of CsPbI₃ film are present as islands (such as point defects, grain boundaries, and non-perovskite phases).²²² For reducing the bulk defects, a molecular additive trioctylphosphine oxide was introduced to the bulk of CsPbI₃, and for reducing the interfacial defects, a surface modifier Ba(OH)₂ was introduced to the SnO₂/CsPbI₃ interface. With reduced defects and suppressed non-radiative recombination, a high V_{OC} of 1.17 V and a PCE of 14% were obtained. 2D WS₂ nanoflakes used to modify the surface of ETL in a CsPbBr₃ solar cell work as a growth template of van der Waals epitaxy for high-quality CsPbBr₃ perovskite film owing to the matched lattices (Figure 21c).²²¹ Moreover, the layer-translational feature of WS₂ allows the interfacial perovskite lattice movement without restraint during annealing and cooling processes, reducing the interfacial tensile strain. Thanks to the improved carrier transfer and suppressed non-radiative recombination related to strain relaxation, an ultrahigh V_{OC} of 1.7 V was achieved, higher than the pristine device showing 1.59 V (Figure 21d). However, the roles of WS₂ which is not clear yet need to be further studied. The peaks in the GIXRD patterns of perovskite on WS₂ still show a shift that is similar to pristine perovskite film when changing the incident angle, which indicates that the strain relaxation is questionable. In addition, the rough surface of ETL with WS₂ might generate a nonuniform effect on perovskite growth. A MoO₃ thin layer, introduced as an interfacial layer between Spiro-OMeTAD and Ag electrode, reduces voltage loss and charge carrier recombination in CsPbI₂Br cells.²²³ The better-matching energy level of MoO₃ facilitates the hole transfer and blocks the electrons, minimizing the possible charge recombination loss at the anode. However, the J-V curves show serious hysteresis and a big difference in V_{OC} , which was also observed in CsPbI₃ solar cells with LiF interfacial layer.^{17, 220} Here, the hysteresis was attributed to the accumulation of ions resulting from external electrical bias and light-induced phase segregation. The mobile ions can pile up at the interface, resulting in the formation of larger injection barriers, hampering carrier extraction and leading to J-V hysteresis in solar cells.²²⁴ It must be noted that the explanation of hysteresis based on ion accumulation is not universal because, in our research on mesoporous-TiO₂-based CsPbI₂Br cells, we have found that the hysteresis can be fully removed.¹⁶⁷ Hence, it is very likely that ion accumulation at the interface and formation of carrier injection barriers depend on device structure and conditions of fabrication.

In summary, interface engineering including perovskite surface modification and insertion of the interfacial layer is a promising method for reducing the surface defects and the non-radiative recombination occurring at the interface. Choosing a proper molecule for perovskite surface passivation is still the primary task.

Except for the passivation effect, the mobility, conductivity, semiconductor type, and energy structure of the molecule need to be considered because it also works as a channel of charge transportation. In this context, a strong bonding with perovskite, good physical properties, and a proper energy level of the molecule are desired for a steady carrier transfer. On the other hand, in some cases, the additional interfacial layer caused severe J-V curve hysteresis and a remarkable V_{OC} difference. This may attribute to the side effects of the interfacial layer, such as the accumulation of ions and poor carrier extraction at the interface. This problem must be solved because it will greatly reduce the reliability of the device's performance.

3.3 Tuning charge transport layers

The CTLs, including ETL and HTM, also significantly affect the V_{OC} output of all-inorganic PSCs. This is because the poor carrier extraction capability of CTLs will make carriers recombine before being extracted from perovskite. More importantly, the ETL and HTM that are popular for hybrid perovskites are not perfectly aligning with the energy level of all-inorganic perovskites, showing a large energy offset. For example, the CB of CsPbI_3 is 0.66 eV higher than the CB of TiO_2 ,²¹⁶ and 0.41 eV higher than that of SnO_2 .²²⁵ On the other side, the popular HTM, Spiro-OMeTAD, has a high HOMO of -5.22 eV, which is 0.55 eV higher than the VB of CsPbI_2Br ,¹⁶ and 0.77 eV than that of CsPbIBr_2 .²²⁶ The similar energy offset also exists in the inverted structure, where the value between HTM (NiO_x , PEDOT:PSS, etc.) and CsPbX_3 perovskites is as larger as 0.9 eV.^{227, 228} This energy offset will lower the QFLS of perovskite, resulting in poor V_{OC} and large energy loss. Therefore, many efforts have been made to design novel ETLs and HTMs specifically for CsPbX_3 perovskites.

3.3.1 Improving ETL and energy alignment

In most all-inorganic PSCs, the conventional TiO_2 is still the most popular ETL. High V_{OC} and performance have been reported by using both TiO_2 -based mesoporous and planar structures. For example, Hong et al. obtained high V_{OC} over 1.3 V for CsPbI_2Br cells with a compact and mesoporous TiO_2 ETL.^{196, 229} In a compact TiO_2 -based planar structure, He et al. also obtained a high V_{OC} of 1.34 V in the champion device with PCE of 17.03%.²⁰⁸ However, in these cases, perovskite doping and surface passivation engineering were also employed, which were the main reasons for such high V_{OC} . SnO_2 , with a better energy matching with CsPbX_3 and a simple low-temperature preparation process, is thought to be a replacement for TiO_2 . You et al. used SnO_2 ETL in the all-inorganic PSCs, as an extension of their work in hybrid PSCs.¹⁵² It was found that the smaller perovskite/ SnO_2 interfacial energy offset could result in a higher V_{OC} but a worse FF than that of TiO_2 because of the poorer electron extraction.²³⁰ For better energy alignment and more efficient electron extraction, Yip et al. inserted a ZnO layer in between the SnO_2 and CsPbI_2Br perovskite.²³¹ The higher CB of ZnO (-4.21 eV) facilitates the desirable cascade energy level alignment between perovskite and SnO_2/ZnO bilayered ETL with stronger electron extraction capability than that based on a single SnO_2 layer (-4.43 eV). This bilayered ETL increased the V_{OC} and FF simultaneously, achieving a high V_{OC} of 1.23 V with a PCE of 14.6%. A solvothermal-synthesized $\text{ZnO}@\text{SnO}_2$ core-shell nanoparticle, which also shows a higher CB than only SnO_2 and has a better energy alignment with CsPbI_2Br , works with enhanced

V_{OC} (1.11 V).²³² It seems ZnO has the potential to be an efficient ETL because of its proper energy level and high electron mobility,^{232, 233} especially in all-inorganic PSCs because the disadvantage of its use in hybrid PSCs, which is deprotonation of MA^+ and FA^+ leading to degradation, can be fully eliminated when used in all-inorganic PSCs.^{234, 235} Wang et al. developed a ZnO ETL using zinc acetate as the Zn source, where they could control the residual content of acetate ions in the final ZnO film.²³⁶ The acetate could conduct the good crystallinity of $CsPbI_2Br$ perovskite and passivate the perovskite through the interaction between cesium and acetate. The ZnO film with the optimal amount of residual acetate, obtained at 150 °C, promoted the device performance to 16.84% with a V_{OC} of 1.24 V. Tang et al. further tuned the energy level of ZnO by doping with Cs_2CO_3 , CsF and K_2CO_3 and the results showed that Cs_2CO_3 has the best doping effect because Cs^+ partially replace Zn^{2+} , which generates dangling bond of O^{2-} and dissociative Cs^+ ions, forming a dipole moment pointing to Zn^{2+} at the ZnO surface.²³⁷ Compared with bare ZnO, Cs_2CO_3 doping contributes to the energy level shift from -4.0 to -3.7 eV, resulting in an enhanced built-in potential across the perovskite layer and significantly suppressed charge recombination loss. The V_{OC} and PCE were improved to 1.28 V and 16.42% (reverse scan), respectively. However, under the forward scan, only 1.23 V and 15.06% were obtained, showing serious hysteresis. The carrier transport property and carrier traps in ZnO ETL need to be considered in the future development of ZnO-based PSCs with suppressed hysteresis.²³⁸

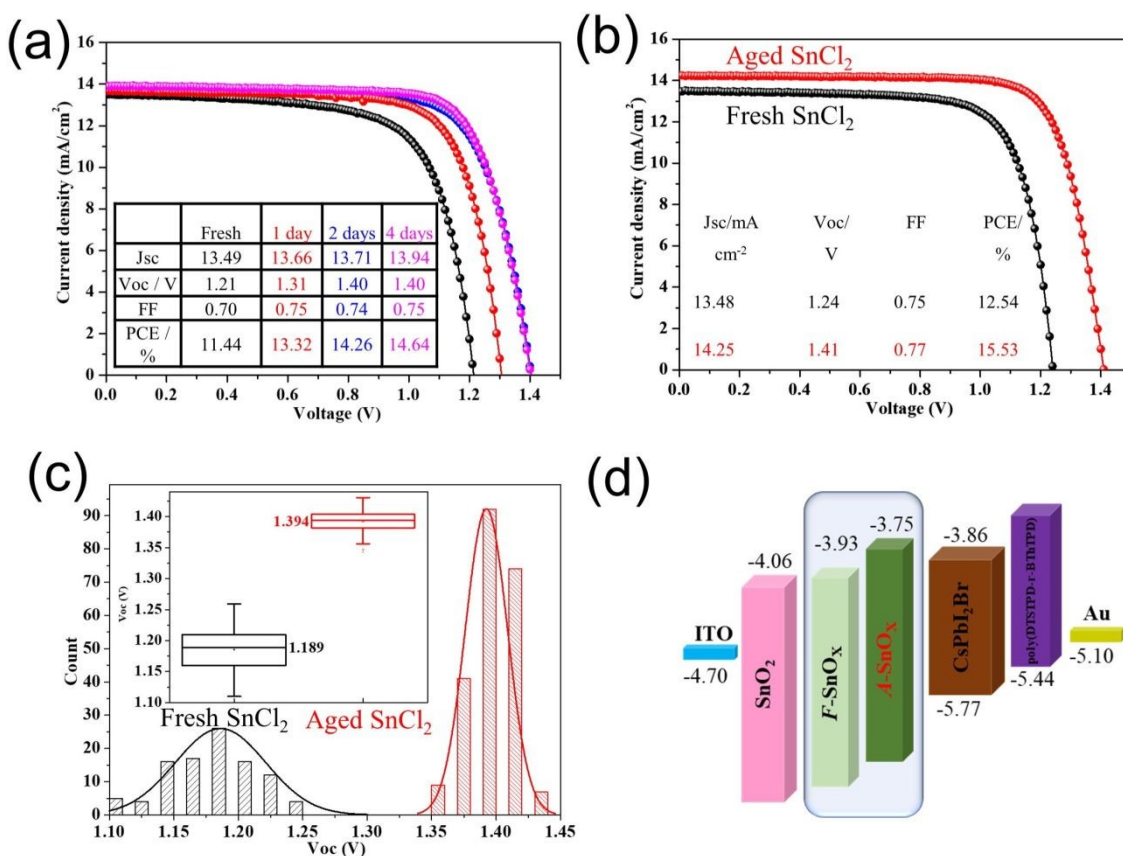


Figure 22 (a) Device performances of $CsPbI_2Br$ solar cells using $SnCl_2$ aging for different days. (b) J-V

curves of the champion devices using fresh and aged SnCl_2 solution. (c) V_{OC} distribution and box chart of solar cells using fresh and aged SnCl_2 solution. (d) Energy level diagrams of the components in the CsPbI_2Br solar cells. $F\text{-SnO}_x$ and $A\text{-SnO}_x$ represent film made using fresh and aged SnCl_2 solution, respectively. (a)-(d),¹⁶ Copyright 2020, American Chemical Society.

As a modification of SnO_2 , we firstly developed a SnCl_2 passivation method for widely used SnO_2 nanoparticle ETL.¹⁵⁵ Specifically, the commercially available SnO_2 colloid was diluted with water and was spin-coated on the ITO substrate followed by annealing, forming the SnO_2 nanoparticle layer. Then the SnCl_2 solution using ethanol and a trace amount of H_2O as the solvent was spin-coated onto the SnO_2 nanoparticle layer followed by annealing to form a SnO_x layer. We found that this surface passivation can effectively suppress the recombination at the interface between the perovskite and SnO_2 . Using carbon as the electrode, a champion V_{OC} of 1.31V was achieved in an HTM-free CsPbIBr_2 solar cell. A similar structure was also reported, where SnCl_2 -induced SnO_2 is on the bottom while SnO_2 nanoparticle is on the top.²³⁹ This strategy also works well by reducing the defects in the SnO_2 nanoparticle layer, facilitating the charge extraction, increasing the crystallinity and orientation of CsPbI_2Br films, and forming a cascade energy level in the device. Consequently, the E_{loss} of CsPbI_2Br PSCs was remarkably reduced, delivering a high V_{OC} of 1.31 V with an excellent PCE of 16.10%. In our recent research, we found an interesting phenomenon that leads to amazingly high V_{OC} output.¹⁶ The process was simply aging the prepared SnCl_2 solution (ethanol and trace amount of H_2O as the solvent) in the air for several days and then using the aged SnCl_2 solution to make an amorphous SnO_x film as ETL for all-inorganic solar cells. Here we used CsPbI_2Br as the light absorber and dopant-free poly(DTSTPD-r-BThTPD) polymer as the HTM (described below). We found that the device V_{OC} gradually increases with prolonging the aging time: from 1.21 V for the fresh solution to 1.40 V for the solution aged more than two days (Figure 22a). We achieved high V_{OC} of 1.41 V (Figure 22b), which is the record-high value for CsPbI_2Br based cells reported in the literature, regardless of doping, additive and passivation engineering. The V_{OC} enhancement has very high reproducibility, showing an average device V_{OC} of 1.39 V, much higher than its counterpart (1.19 V) using fresh SnCl_2 solution (Figure 22c). Importantly, this $A\text{-SnO}_x$ ETL also has good universality for all-inorganic PSCs with different light absorbers. As a reason account for the high V_{OC} of $A\text{-SnO}_x$ ETL-based devices, we found that during the aging process, the initially generated large particles, e.g. $\text{Sn}(\text{OH})_2$ and $\text{Sn}(\text{CH}_3\text{CH}_2\text{O})_2$, by hydrolysis and alcoholysis of SnCl_2 , gradually dissolve into the EtOH solvent, resulting in smaller nuclei helping in uniform growth of SnO_x film. Moreover, the SnO_x film obtained from the aged SnCl_2 ($A\text{-SnO}_x$) contains pure Sn^{4+} while that from fresh SnCl_2 ($F\text{-SnO}_x$) contains Sn^{2+} impurity as well as higher Cl residual. This difference accounts for the different energy levels: $A\text{-SnO}_x$ has a higher CB than that of CsPbI_2Br , forming a spike structure, which remarkably suppresses the charge recombination at the $A\text{-SnO}_x/\text{CsPbI}_2\text{Br}$ interface (Figure 22d), resulting in a high V_{OC} output. Alternatively, as inspired the work of Nazeeruddin et al.,¹²⁴ a band-bend between the perovskite bulk and surface (buried interface) may form here, which can enhance the electron extraction from perovskite bulk to the $A\text{-SnO}_x$ side. Using Spiro-OMeTAD with a shallower HOMO level (-5.22 eV) and P3HT (-5.00 eV) as HTM the devices showed

lower V_{OC} of 1.37 and 1.32 V, respectively. Therefore, it is believed that the HOMO level of the HTM, e.g., energy offset at the perovskite/HTM interface becomes the key factor determining the V_{OC} , after the recombination at the ETL/perovskite interface is highly suppressed by the 5 nm $A\text{-SnO}_x$ barrier layer which blocks the electron back transfer to perovskite. In other words, developing more suitable HTMs with matching energy levels as well as high mobility and conductivity is important for achieving high V_{OC} output for CsPbX_3 solar cells.

3.3.2 Improving HTM and energy alignment

Though Spiro-OMeTAD with dopant is still the most popular HTM for CsPbX_3 solar cells,^{146, 147, 158, 240} it is not suitable for CsPbX_3 perovskites mainly because the CsPbX_3 , especially iodine-rich perovskite, are very sensitive to humidity and the hygroscopic Li-TFSI dopant used in Spiro-OMeTAD can introduce moisture and induce the phase transition of CsPbX_3 . For example, as found by Hu et al., Spiro-OMeTAD causes the conversion of the photoactive perovskite phase to the photo-inactive phase within 10 min in ambient conditions, leading to an efficiency plunge from 14.87% to 0.14%.¹⁵⁴

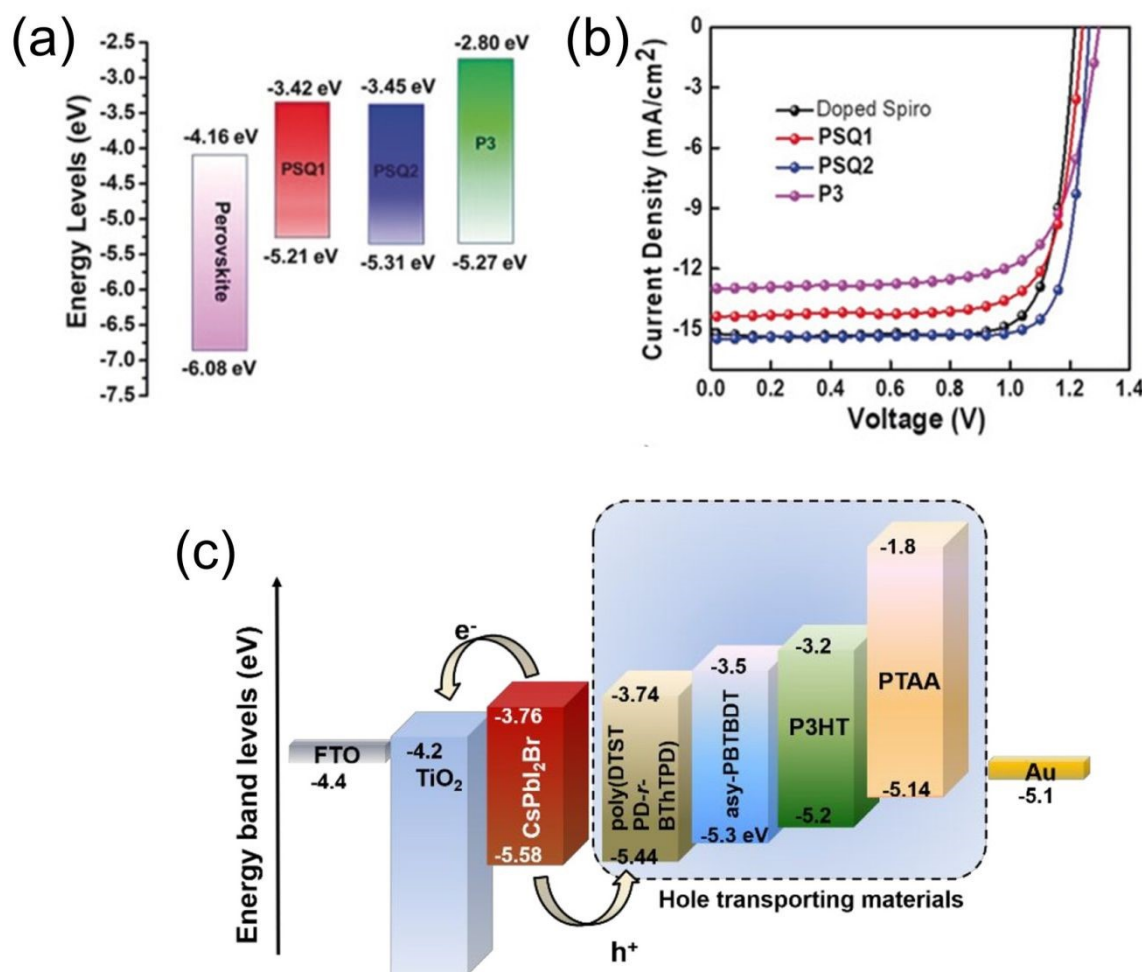


Figure 23 (a) Energy levels of polymer HTMs relative to CsPbI_2Br perovskite. (b) J-V curves of best-performing CsPbI_2Br PSCs with different HTMs. (a) and (b),²⁴¹ Copyright 2019, Wiley-VCH. (c)

Schematic diagram presenting energy levels of CsPbI_2Br with respect to HOMO and LUMO levels of the different HTMs.¹⁶⁷ Copyright 2020, American Chemical Society.

For solving the stability issue and increasing the device performance, efforts have been made to develop new dopant-free HTMs with excellent properties, which are summarized in this part. Hu's group used the dopant-free P3HT as the HTM for CsPbI_2Br cells, showing a comparable efficiency to that of Spiro-OMeTAD with dopants.¹⁵⁴ The PCE was further promoted to 15.50% ($V_{OC} = 1.26$ V) after introducing a buffer layer, which tuned the energy level between perovskite and P3HT. However, the large energy offset (0.93 eV) at the $\text{CsPbI}_2\text{Br}/\text{P3HT}$ interface was still lowering the QFLS and limiting the V_{OC} output. As a solution, they inserted a small molecule SMe-TATPyr layer between the perovskite and P3HT, which lowered the P3HT HOMO level to -5.03 eV, slightly alleviating the mismatch.²⁴² More importantly, the SMe-TATPyr molecule breaks the long-range ordering of "edge-on" P3HT and induces the formation of "face-on" clusters, and improves the hole mobility. Meanwhile, the sulfur-rich molecule works as a passivator for reducing the perovskite surface defect density through the Pb-S interaction. All of these advantages significantly promoted the performance of CsPbI_2Br solar cells, resulting in an impressive V_{OC} of 1.38 V and a champion efficiency of 16.93% (reverse scan). Nevertheless, severe hysteresis in the performance, showing only 1.28 V and 14.89% under the forward scan remained a significant drawback. Such hysteresis property leads to erroneous estimation of photovoltaic performance, and the reliability during actual performance becomes questionable, which will be a serious obstacle for the commercialization perspective.²⁴³ The hysteresis, though less serious, was also observed in our research employing P3HT as HTM.²⁴⁴ It is believed that the unbalanced charge extraction and the interfacial trap-assisted charge recombination need to be considered for alleviating the hysteresis in P3HT-based CsPbI_2Br solar cells.^{245, 246} For thoroughly eliminating the drawback of P3HT, other dopant-free HTMs with better energy level alignment with CsPbX_3 perovskite have been developed. Yip and co-workers developed several squaraines-based polymers with deeper HOMO levels than those of Spiro-OMeTAD and P3HT (Figure 23a).²⁴¹ The polymers were synthesized by polymerizing squaraines into pseudo-2D p-p conjugated polymers, using N, N-diarylanilinosquaraines as the co-monomers. This rational design endows the polysquareaines with ultra-high hole mobility approaching $0.01 \text{ cm}^2 \text{ V}^{-1} \text{ s}^{-1}$. Moreover, these polysquareaines, inheriting from the squareaines, also have a passivation effect on the perovskite surface through the interaction between Pb^{2+} and carbonyl group and oxygen ions of polysquareaines. As a consequence, the champion PCE of 15.5% with V_{OC} of 1.27 V has been accomplished (Figure 23b), outperforming that of the doped Spiro-OMeTAD-based devices (14.4% and 1.22 V).

We also developed a dopant-free HTM, poly(DTSTPD-r-BThTPD), with a deep HOMO of -5.44 eV, well matching with CsPbI_2Br perovskite (Figure 23c).¹⁶⁷ This donor-acceptor type random copolymer was synthesized by a Kosugi-Migita-Stille cross-coupling reaction. We found that this polymer, used as HTM in CsPbI_2Br solar cells with a structure of FTO/c-TiO₂/meso-TiO₂/1% lead propionate- CsPbI_2Br /poly(DTSTPD-r-BThTPD)/Au, worked with champion efficiency of 14.58% and V_{OC} of 1.15 V and the J-V curves were hysteresis-free. Moreover, by further increasing the additive amount to 5%, an

impressive V_{OC} of 1.36 V was obtained while the J_{SC} decreased obviously due to the low crystallinity of the film. By changing the substrate to ITO and the ETL to *A*-SnO_x, the poly(DTSTPD-r-BThTPD) enabled an extremely high V_{OC} of 1.41 V and high efficiency of 15.53% (Figure 22b).¹⁶ Here, though a decent efficiency was achieved, the J_{SC} and FF were not satisfactory, compared to other reports.

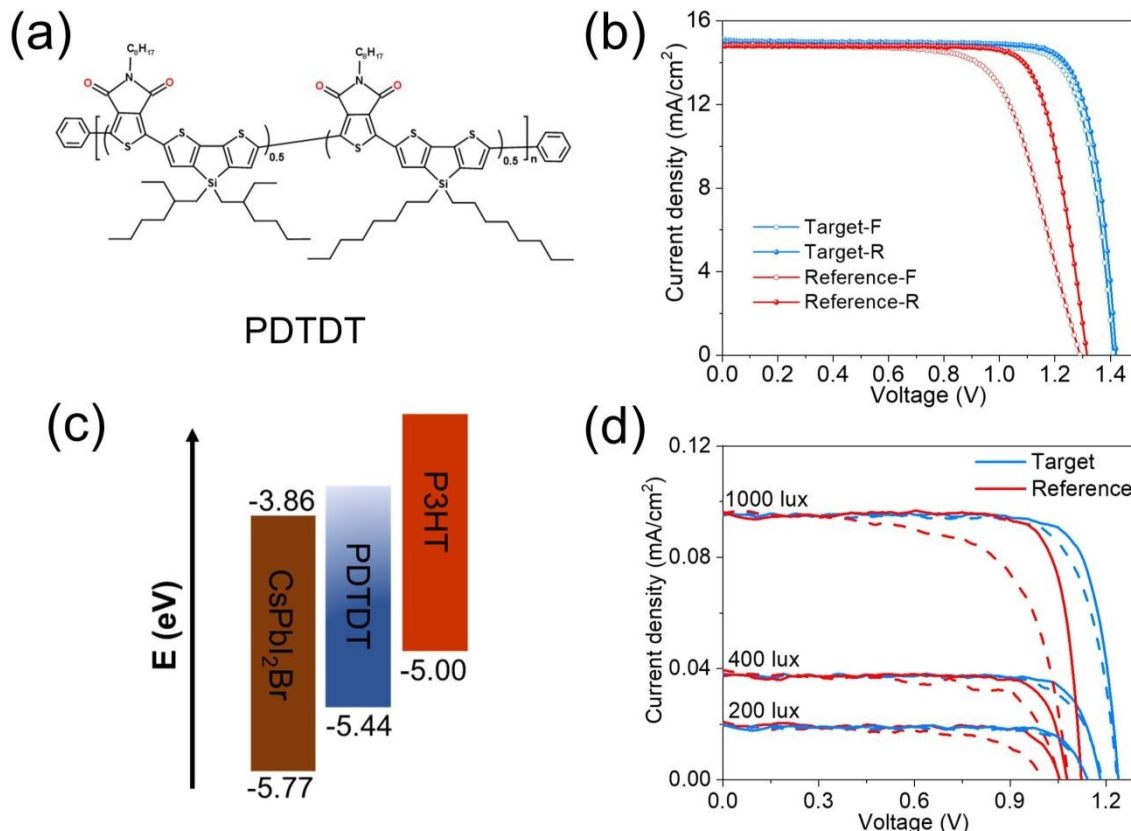


Figure 24 (a) Molecule structure of PDTDT polymer HTM. (b) J-V curves of champion target and reference CsPbI₂Br solar cells. (c) Energy level of CsPbI₂Br perovskite and HOMO level of HTMs. (d) J-V curves of target and reference CsPbI₂Br solar cells under LED light illumination with different light intensities. Target: device using PDTDT as HTM; Reference: device using P3HT as HTM. (a)-(d),²⁴⁴ Copyright 2021, Wiley-VCH.

For further enhancing J_{SC} and FF, we modified the molecular structure of poly(DTSTPD-r-BThTPD) but kept the HOMO level for maintaining the high V_{OC} of the final device (1.42 V with certification).²⁴⁴ In poly(DTSTPD-r-BThTPD), the bithiophene part easily twists, which reduces π -conjugation and polymer planarity, decreasing the carrier mobility and carrier injection efficiency. To restrict such twisting, we introduced the Si atom into bithiophene moiety and the resultant silole moiety could enhance the planarity of the polymer backbone and increase the interchain π - π overlapping. The newly designed polymer PDTDT (Figure 24a) possesses a predominant face-on orientation, as proved by GIWAXS measurements, which is favorable for hole transport in PSCs. With enhanced planarity of the backbone, increased interchain π - π overlapping, and face-on orientation, PDTDT exhibits a high hole mobility of $3.14 \times 10^{-3} \text{ cm}^2 \text{ V}^{-1} \cdot \text{s}^{-1}$, which

is higher than poly(DTSTPD-r-BThTPD) (1.50×10^{-3} cm 2 V $^{-1}\cdot$ s $^{-1}$) and P3HT (1.67×10^{-3} cm 2 V $^{-1}\cdot$ s $^{-1}$). With PDTDT HTM, we achieved increased J_{SC} and FF without any sacrifice of V_{OC}, and finally, a PCE of 17.36% was accomplished (Figure 24b). The dopant-free P3HT showed an inferior V_{OC} of 1.32 V and an efficiency of 15.22%. By looking into the V_{OC} output order: PDTDT (-5.44 eV) > Spiro-OMeTAD (-5.22 eV) > P3HT (-5.00 eV) (Figure 24c), we could confirm again that the HOMO level of HTM is determining the V_{OC} of the solar cells. Moreover, the high V_{OC} achieved with PDTDT HTM reflects suppressed trap-assisted carrier recombination in the device, which manifests its potential for indoor application. Also, the 1.91 eV bandgap of CsPbI₂Br is almost the optimum value for indoor photovoltaics because of well matching the room light spectrum. Then we checked the indoor photovoltaic performance of the devices using a LED light source. Under 200, 400, and 1000 lux light illumination, the device using PDTDT shows efficiency of 34.20%, 32.29% and 32.60%, respectively (Figure 24d). The PCE of 34.20% is the highest value for CsPbI₂Br solar cells and is higher than most indoor perovskite photovoltaics. Encouragingly, we also obtained ultra-high V_{OC}: 1.14 V under 200 lux, 1.18 V under 400 lux, and 1.23 V under 1000 lux. Regarding the voltage requirement (1.0 V) of a single junction indoor photovoltaic, the high V_{OC} achieved here emphasizes the potential of CsPbX₃ cells working as indoor devices to power the Internet of Things ecosystem. Some other novel dopant-free HTMs have also been developed for CsPbX₃ solar cells.²⁴⁷⁻²⁵¹ As can be summarized here, a good dopant-free HTM for PSCs should possess three merits including high hole mobility, good energy alignment with perovskite, and passivation effects on perovskite surface. We expect that, if these dopant-free HTMs can be mass-produced at a low cost, their prospects for commercialization of all-inorganic CsPbX₃ PSCs, especially for application as indoor photovoltaics, will be certainly high.

3.3.3 Improving inverted structure CsPbX₃ solar cells

Another solution for avoiding the limitation of Spiro-OMeTAD is to use inverted (p-i-n) architecture. The inverted structure is also advantageous for CsPbX₃ utilization in tandem solar cells because most all-perovskite tandem cells are manufactured in an inverted form.^{252, 253} While CsPbX₃ solar cells with an inverted structure are still uncommon and their device performance is lower than those with a normal (n-i-p) structure.^{210, 227, 228, 254-256} One of the main reasons that impede the efficiency is the imperfect interface charge transfer and undesired charge recombination caused by the large energy offset at the perovskite/CTL interface. Specifically, the energy offset between the PEDOT:PSS and CsPbI₂Br is as large as 0.98 eV and 0.86 eV for that between NiO_X and CsPbIBr₂.^{227, 228} Yip et al. developed TPE-S, a novel small molecular HTM based on tetraphenylethylene (TPE), which lowered the energy offset from 0.98 eV in the PEDOT:PSS case to 0.79 eV.²²⁸ As a result, the V_{OC} was improved from 1.15 to 1.26 V, pushing the efficiency to 15.4%. Ma et al. inserted N749 dye into the interface between NiO_X and CsPbIBr₂ for tuning the energy alignment.²²⁷ The proper HOMO level of N749 facilitated the carrier transport and suppressed the carrier recombination. The V_{OC} was remarkably boosted from 0.86 to 1.22 V, resulting in an efficiency improvement from 6.28 to 9.49%. Similarly, the large energy offset at the perovskite/ETL interface has been diminished to improve V_{OC}. For instance, Jen group used 6TIC-4F (described above) to passivate the

$\text{CsPbI}_x\text{Br}_{3-x}$ perovskite (1.78 eV), which also tuned the energy alignment between perovskite and ZnO .²¹⁰ With reduced energy offset from 0.76 to 0.65 eV, the V_{OC} of the inverted $\text{CsPbI}_x\text{Br}_{3-x}$ solar cell was enhanced from 1.10 to 1.16 V.

In conclusion, the inverted structure should be more promising for CsPbX_3 photovoltaic cells due to its low-temperature processibility and compatibility with tandem solar cells. Similar to the normal structure cells, the inverted CsPbX_3 cells suffer from a huge energy offset and poor V_{OC} output. Up to now, only a few HTMs are available for inverted cells, which partly makes it less popular. We believe that finding more suitable HTMs^{228, 255, 256} to reduce the large interface energy offset is critical to the development of inverted CsPbX_3 solar cells.

4 Tin perovskite solar cells

As an element sitting just above Pb in group 14 of the periodic table, Sn is a possible replacement for Pb, and Sn-based perovskites (ASnX_3 ; A = FA, MA, Cs; X = I, Br) adopt structures similar to those of Pb counterparts, which leads to analogical photovoltaic characteristics, such as high absorption coefficient, small exciton binding energy, and high carrier mobility, etc.^{257, 258} In general, Sn-based perovskites have a lower bandgap than their Pb-counterparts. Compositions like MASnI_3 and FASnI_3 with E_g values of 1.25 and 1.4 eV respectively, match the optimum bandgap range for maximum efficiency estimated by the S-Q limit. Therefore, Sn-base PSCs are expected to work better than the Pb-counterparts. Following the seminal work from Kanatzidis's group²⁵⁹ and Snaith's group,²⁶⁰ the tin-based PSCs are drawing increasing attention due to their promise for efficient and environment-friendly Pb-free PSCs. However, compared with Pb-based counterparts, Sn-based PSCs always suffer more severe energy loss. For example, FASnI_3 perovskite has an E_g of 1.40 eV, while most reported V_{OC} values are lower than 0.9 V, with an E_{loss} over 0.5 eV, which is quite large for narrow-band perovskites. Though recent works have achieved V_{OC} over 0.9 V,^{18, 261} it still has a gap between the theoretical V_{OC} of over 1.1 V according to the S-Q limit. The E_{loss} is due to the non-radiative charge recombination in the device, which can be attributed to i) poor film quality because of rapid crystallization (no intermediate state),^{260, 262} resulting in a high defect density of $\sim 10^{16} \text{ cm}^{-3}$,²⁶³ ii) easy oxidation of Sn^{2+} in Sn^{4+} , leading to too high background carrier (hole) density and Sn vacancy;²⁵⁸ iii) short carrier diffusion length of tin perovskite and disadvantageous energy level alignment with common charge transport layers, causing poor carrier extraction efficiency.^{263, 264}

4.1 Improving tin perovskite film quality

4.1.1 Controlling tin perovskite film growth

Like in Pb-perovskites, improving the film quality by precisely controlling the crystal growth, including optimization of the fabrication process by varying perovskite precursor and perovskite film composition results in enhanced V_{OC} in Sn-perovskites. For instance, Wakamiya group developed a method of hot antisolvent treatment (HAT) process that resulted in higher V_{OC} for $\text{FA}_{0.75}\text{MA}_{0.25}\text{SnI}_3$ perovskite.²⁶² The HAT, where hot chlorobenzene was used instead of the room temperature solvent increased the number of

nuclei and thus, improved the coverage, homogeneity, and grain size of the final film. This integrated technique promoted the V_{OC} from 0.36 to 0.55 V with an enhanced PCE of 7.2%. On the contrary, Han et al. found that a decrease in the number of nuclei is more favorable for tin perovskite crystal growth.²⁶⁵ Specifically, a cold perovskite precursor was used for spin-coating, where the nucleation rate was retarded and the number of nuclei was decreased, leaving more space and time for crystal growth, resulting in FASnI₃ perovskite crystals with large grain size and preferential orientation as well as better device performance (Figure 25a and b). This film with the post-treatment by n-propylammonium iodide (PAI) solution worked with a high PCE of 12.11% and V_{OC} of 0.77 V in the best device (Figure 25c). Although the perovskites and solvent systems were different in the above two studies, which could be the reason why the film quality was improved by two opposite approaches, it can be comprehended from the two studies that cold solution generates fewer nuclei and larger grain size, while hot solution generates more nuclei and smaller grain size. It seems that the controlled perovskite crystal growth resulting in uniform pinhole-free film is more important than the perovskite grain size.

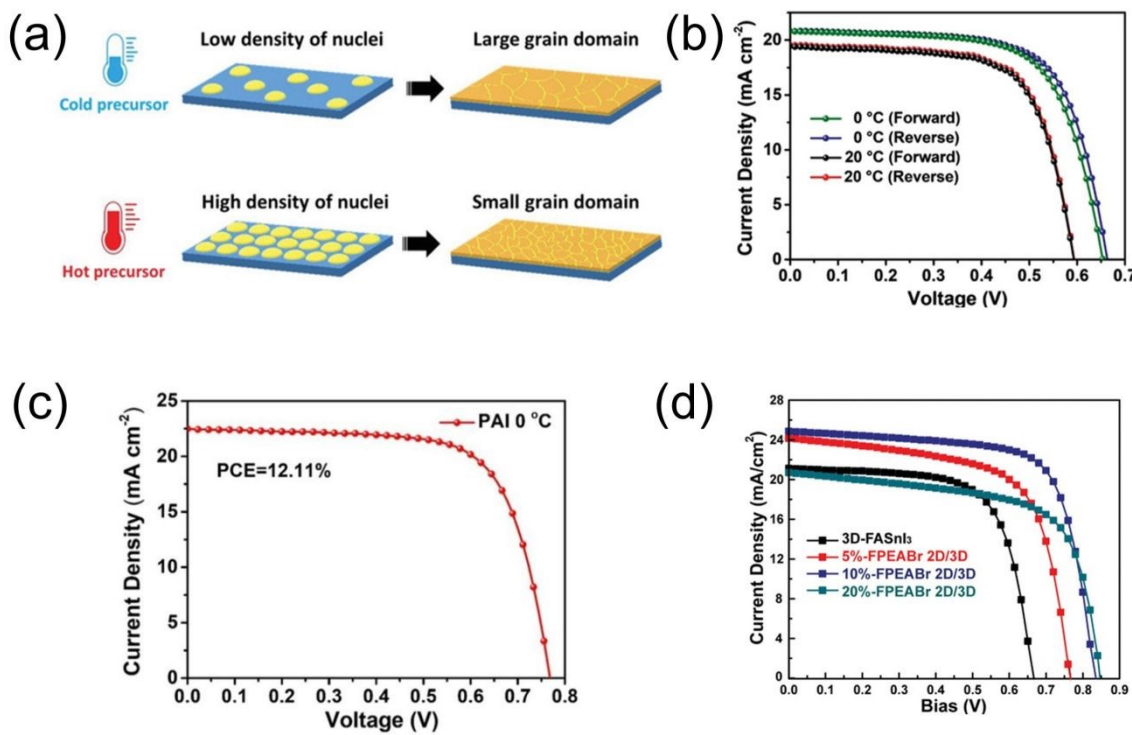


Figure 25 (a) Schematic illustration of the nucleation mechanism for FASnI₃ perovskite films with different precursor temperatures. (b) J-V curves of the best-performing PSCs based on FASnI₃-0 °C and FASnI₃-20 °C films. (c) J-V curve of the champion device based on n-propylammonium iodide (PAI) post-treated FASnI₃-0 °C film. (a)-(c),²⁶⁵ Copyright 2021, Wiley-VCH. (d) J-V curves of the champion devices containing pure 3D FASnI₃ and 2D/3D perovskite with different 4-fluoro-phenethylammonium bromide (FPEABr) concentrations.²⁶⁶ Copyright 2021, Wiley-VCH.

Besides controlling the Sn compound properties in the precursor, the Sn perovskite crystal growth can be

regulated through coordination interactions. For example, n-butylammonium acetate (BAAc) ionic liquid could tune the tin coordination with O...Sn chelating bonds and N-H ... X hydrogen bonds.²⁶⁷ These interactions were able to slow down the crystal growth rate, generating high-quality, Sn⁴⁺-fewer FASnI₃ film with preferential crystal orientation. In consequence, the V_{OC} was promoted to 0.65 V (PCE=10.4%) from 0.60 V (8.6%). With the same working mechanism, formamidine acetate (FAAc) ionic liquid was also studied in FASnI₃ PSCs, achieving 9.96% efficiency.²⁶⁸ The interaction between ammonium and halide seems to be an effective way to control the Sn perovskite growth. Diau et al. introduced ethylenediammonium diiodide (EDAI₂) to FASnI₃ perovskite to slow down the crystal growth via the interactions between the ammonium functional groups and tin perovskite.²⁶⁹ With 1% EDAl₂ additive, dense and pinhole-free perovskite film, suppressed Sn²⁺ oxidation, and reduced defect states were achieved. The modified device achieved high initial efficiency of 7.4% and V_{OC} of 0.52 V, higher than the reference with 4.0% and 0.36 V, respectively. More interestingly, the efficiency of the 7.4%-device slowly increased to 8.9% (V_{OC} of 0.58 V) during the storage in the glove box, which was attributed to the slow relaxation of crystal strain induced by the EDAl₂ additive. Such V_{OC} and efficiency increment during the storage have been also observed in other studies on Sn-based solar cells.²⁷⁰⁻²⁷² Light soaking was also proved to improve V_{OC} and PCE. Mora-Sero et al. added dipropylammonium iodide and NaBH₄ into the FASnI₃ and tested the device stability under continuous illumination under one sun with a UV cut-off filter.²⁷³ They discovered that the initial efficiency of both pristine and modified cells increased due to the substantial increase in V_{OC} and that the modified PSC continued to increase for 500 h. However, the mechanism of light-soaking-induced V_{OC} increase has yet to be discovered. A large organic ammonium molecule, butylammonium iodide (BAI), added to FASnI₃ perovskite has been found to alter the orientation of perovskite crystal and improve the connectivity of the crystal grains. Here, the optimal amount of BAI was 15% and increasing the amount to 20%, a BA-based 2D structure was detected. Thus, it is believed that the formed 2D structure possibly benefits the cell by enhancing its performance. Up to now, many long-chain organic ammoniums such as phenethylammonium iodide (PEAI),²⁷⁴⁻²⁷⁷ n-propylammonium iodide,²⁷⁸ triethylphosphine,²⁷⁹ and thienylethylammonium²⁸⁰ have been used to assist the oriented tin perovskite growth or form beneficial 2D tin perovskite. Very recent work reported the highest efficiency of 14.81% (V_{OC} of 0.84 V) for tin-based PSCs with 2D/3D structure, made by using FPEABr that substitutes FAI in FASnI₃ perovskite (Figure 25d). In this case, the high performance was attributed to the preferential crystal orientation, suppression of Sn²⁺ oxidation, and decreased defect density.²⁶⁶ Ning's group introduced removable pseudohalogen ammonium thiocyanate (NH₄SCN) to manipulate the crystal growth process of tin perovskite, leading to the formation of a 2D-quasi-2D-3D hierarchy structure.²⁸¹ Because of the 2D layer on the surface, the air stability was remarkably enhanced and the carrier density was reduced, and the V_{OC} was also slightly improved from 0.58 to 0.61 V. Similar to the 2D capping layer, other passivation layers on the tin perovskite surface has been also proved to be sufficient to enhance the device performance. For instance, Hayase et. al. developed a post-treatment method of tin perovskite with edamine Lewis base.²⁸² They found that the amine group in edamine bonds to the undercoordinated tin, passivating the dangling bonds and defects and suppressing the Sn²⁺ oxidation, leading to suppressed charge carrier recombination. Finally, with the help of V_{OC}

improvement by 0.11 V, the efficiency surpassed 10%, which was first report with PCE above 10% for any Sn-based PSCs. Therefore, besides the bulk properties, surface property of Sn perovskite is also equally important because the surface can suffer from more defects and more severe Sn^{2+} oxidation. This puts forward higher demands for interface charge extraction; the carriers need to be efficiently extracted from perovskite before recombination.

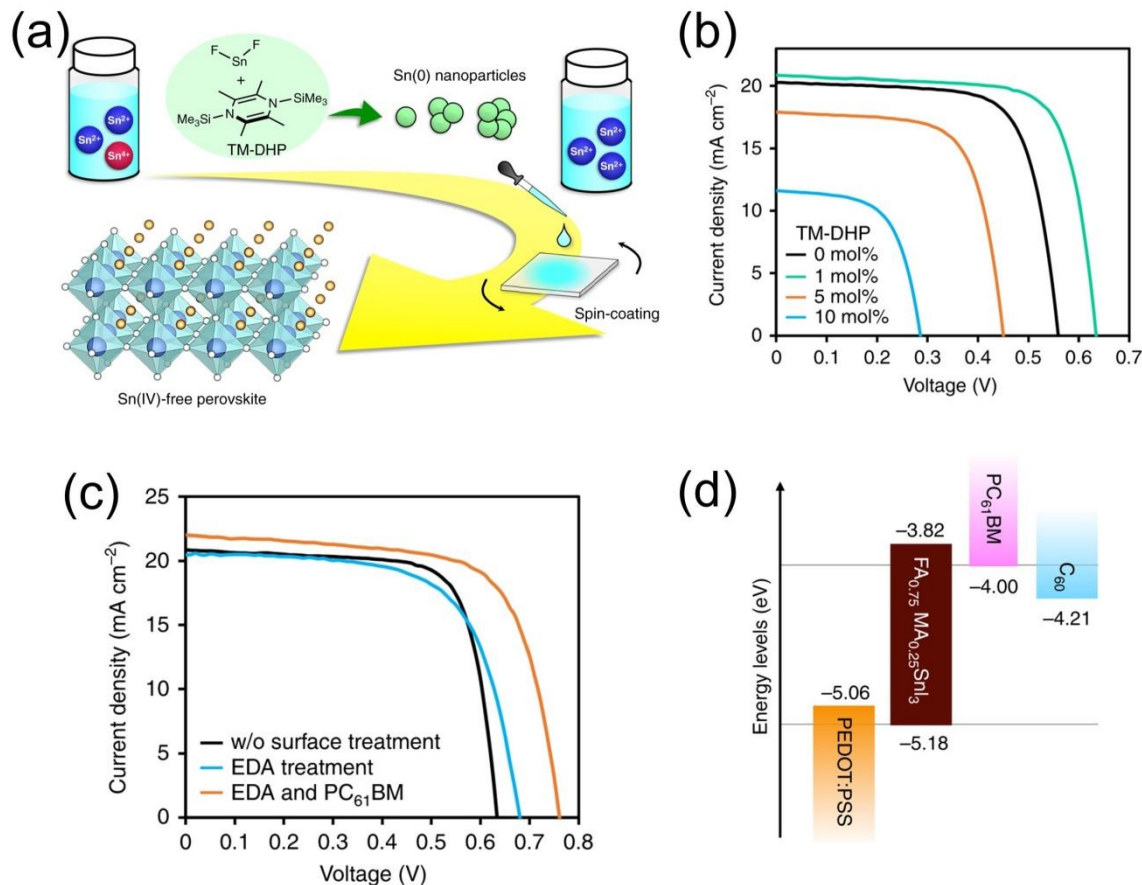


Figure 26 (a) Schematic illustration of the Sn(IV) scavenging method. 1,4-Bis(trimethylsilyl)-2,3,5,6-tetramethyl-1,4-dihydropyrazine (TM-DHP) is added to the tin perovskite precursor solution. $\text{Sn}(0)$ nanoparticles formed by the reduction of SnF_2 by TM-DHP scavenge residual Sn(IV) impurities. (b) J-V curves of PSCs based on $\text{FA}_{0.75}\text{MA}_{0.25}\text{SnI}_3$ perovskite prepared by adding different amounts of reductant TM-DHP. (c) J-V curves of Sn-based PSCs with or without surface treatment using ethylene diamine (EDA) and PC_{61}BM . (d) Energy levels diagram of the cell components. (a)-(d).²⁶⁴ Reprinted with permission from Nature Publishing Group (2020).

4.1.2 Preventing Sn^{2+} oxidation

Uniform, pin-hole-free film with large grains is essential but not sufficient for achieving high V_{oc} . Although high-quality perovskite films were obtained in the above studies, the quantum efficiency of the solar cells was still low, indicating severe non-radiative recombination in the perovskite. Specifically, the Sn^{2+} oxidation could induce heavy self-doping and increase the background carrier density in the perovskite,

leading to severe charge recombination and a short carrier lifetime. The oxidation of Sn^{2+} can happen very quickly upon exposure to air and moisture. Therefore, Sn-based PSCs are only assembled in an inert gas (N_2 or Ar)-filled glove box. Moreover, the use of degassed solvents and pure precursors is also important. Sn^{4+} impurity in the raw materials can deteriorate the performance. For example, Wakamiya et al. found about 10 wt% SnI_4 impurities in SnI_2 (99.9%, trace metals basis, purchased from Kojundo Chemical Laboratory Co., Ltd.).²⁸³ The impurity was sublimated by heating and pure SnI_2 was recrystallized, generating colorless crystalline needles of $[\text{SnI}_2(\text{DMF})]$ and $[\text{SnI}_2(\text{DMSO})]$. The $\text{FA}_{0.75}\text{MA}_{0.25}\text{SnI}_3$ perovskite films made from these pure Sn precursors showed energy levels different from that of the unpurified SnI_2 . Furthermore, 1,4-bis(trimethylsilyl)-2,3,5,6-tetramethyl-1,4-dihydropyrazine (TM-DHP) reductant was added to the $\text{FA}_{0.75}\text{MA}_{0.25}\text{SnI}_3$ perovskite precursor containing 10 mol% SnF_2 .²⁶⁴ TM-DHP can selectively reduce the SnF_2 , forming Sn (0) nanoparticles, which scavenges Sn^{4+} impurities in the precursor (Figure 26a). Finally, the Sn^{4+} ratio on the perovskite film surface was reduced and the bulk became Sn^{4+} -free. Here, the selective reduction of SnF_2 , attributed to the strong affinity of fluoride, is the key factor in the Sn^{4+} removal, which emphasizes the necessity of SnF_2 additive to tin perovskite. Employing this Sn^{4+} -free film in the p-i-n device structure, the V_{OC} was promoted to 0.63 V (PCE= 9.9%) (Figure 26b). And, after perovskite surface treatment with ethylene diamine (EDA) and by minimizing the interfacial energy gap using PCBM, the efficiency and V_{OC} was further promoted to 11.5% and 0.76 V, respectively (Figure 26c and d). A more simple method by adding Sn (0) powder to the perovskite precursor was also reported, in which metallic Sn works as a reductant to convert Sn^{4+} to Sn^{2+} , suppressing the recombination loss and promoting V_{OC} from 0.19 to 0.58 V (PCE= 6.75%).²⁵⁸ Although the reduction reaction between Sn (0) and Sn^{4+} can compensate Sn^{2+} in the system, the SnF_2 additive is still necessary for high-performance cells. The roles of SnF_2 additive in tin perovskite were recently elucidated by Abate et al.²⁸⁴ They found that fluoride anions show a stronger affinity to Sn^{4+} over Sn^{2+} , selectively complexing it as SnF_4 . The SnF_4 has a lower tendency to be included in the perovskite structure than that of SnI_4 , hence preventing the inclusion of Sn^{4+} in the final film. Fluoride also has a strong influence on the colloidal chemistry of precursor dispersions, directly affecting perovskite crystallization.

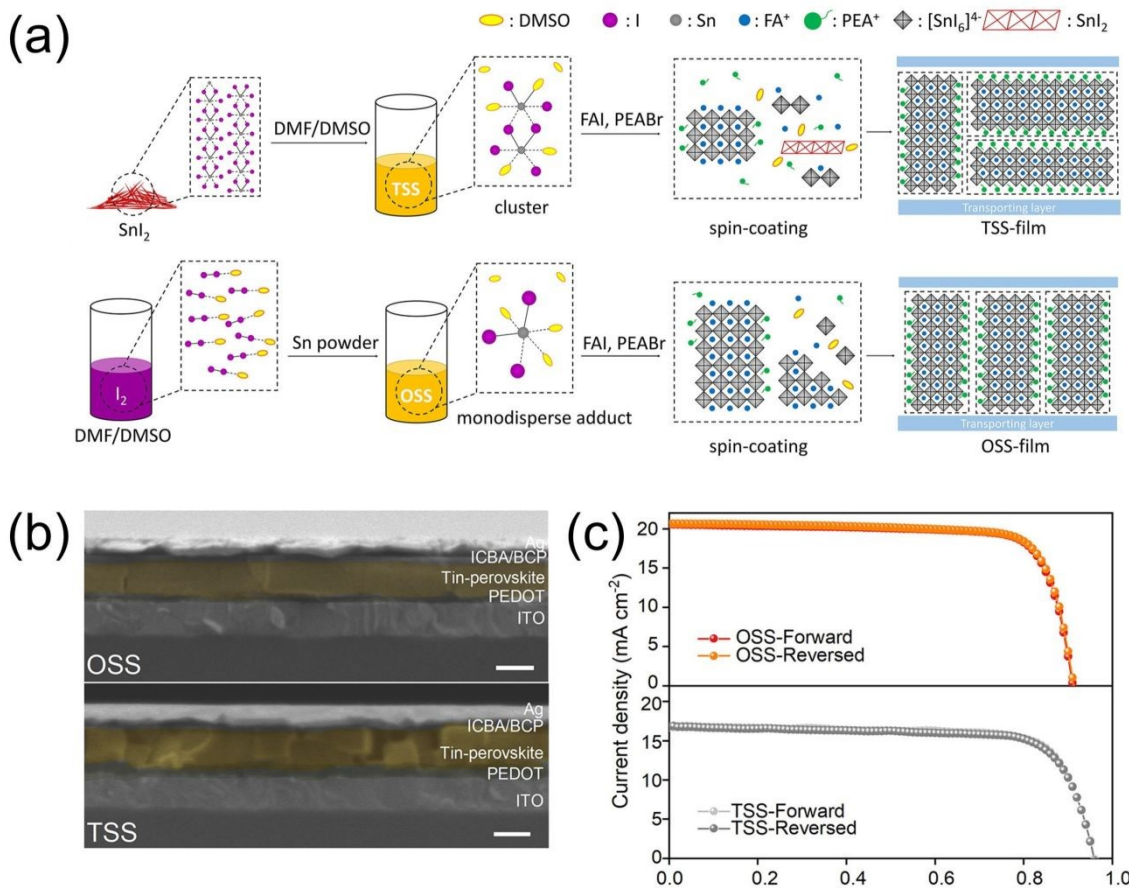


Figure 27 (a) One-step synthesis (OSS) and two-step synthesis (TSS) method for SnI_2 precursor and perovskite film preparation. (b) Cross-sectional SEM images of OSS and TSS devices. (c) J-V curves of the champion devices based on the tin-perovskite prepared by OSS and TSS method. (a)-(c),²⁶¹ Copyright 2021, American Chemical Society.

The importance of Sn adduct in controlling the tin perovskite film property was studied by Ning's group.²⁶¹ They prepared $\text{SnI}_2 \cdot (\text{DMSO})_x$ adduct by the reaction between Sn (0) and I_2 in DMF/DMSO solvent. The adduct is well-dispersed in the precursor solution, avoiding needle-shaped SnI_2 segregation and enabling uniform perovskite films with increased out-of-plane crystal orientation (Figure 27a). The solar cells (structure in Figure 27b) showed high efficiency of 14.6% with V_{OC} of 0.91 V, and J_{SC} of $20.6 \text{ mA} \cdot \text{cm}^{-2}$ (Figure 27c). The high J_{SC} , in this case, was due to the enhanced diffusion length owing to the orientation of the perovskite film. Whereas, for the case where synthesized SnI_2 was dissolved into the solvent, an even higher V_{OC} of 0.96 V was obtained. But, a lower PCE (12.2%) in the latter case was due to lower J_{SC} (Figure 27c) possibly because of the large voids in perovskite film. It seems that the better morphology of tin perovskite film is favorable for higher J_{SC} , but it doesn't necessarily guarantee less non-radiative recombination in the film. On the other hand, similar to the case of excess PbI_2 in lead perovskites,²⁸⁵ the SnI_2 cluster may also play a positive role in achieving high voltage, which needs more study to confirm.

4.2 Minimizing interface recombination

4.2.1 Tuning energy alignment in inverted structure

The biggest interfacial problem is the energy level mismatching between tin perovskite and the charge extraction materials that are more suitable for lead perovskites. There is always a large energy level offset between perovskite and ETL/HTM, which is restricting the attainable voltage output of the cells. For example, in the inverted structure of tin-based PSCs, PEDOT:PSS is the most widely used HTM, which possesses a work function (WF) of -5.0 eV, much higher than the VB of FASnI_3 (-5.59 eV).²⁸⁶ This inferior band alignment of tin perovskite with the HTM results in poor hole extraction and a lower voltage. To improve the band alignment, efforts have been made to modify the energy structure of perovskite to match those of the charge extraction layers. For example, Wakamiya et al. prepared a series of $\text{FA}_x\text{MA}_{1-x}\text{SnI}_3$ perovskites and found that FA-rich perovskites have larger bandgaps than those of MA-rich ones, and $\text{FA}_{0.75}\text{MA}_{0.25}\text{SnI}_3$ has the optimized alignment with PEDOT:PSS.²⁶² Diau and co-workers incorporated a nonpolar organic cation, guanidinium (GA^+) into the FASnI_3 perovskite (with 1% EDAI_2).²⁸⁷ Here, the VB of FASnI_3 gradually decreases with increasing GA^+ amount and E_g slowly increases. With 20% GA^+ , the perovskite exhibits the optimal alignment with PEDOT:PSS, showing an enhanced V_{OC} of 0.62 V (PCE=9.6%).

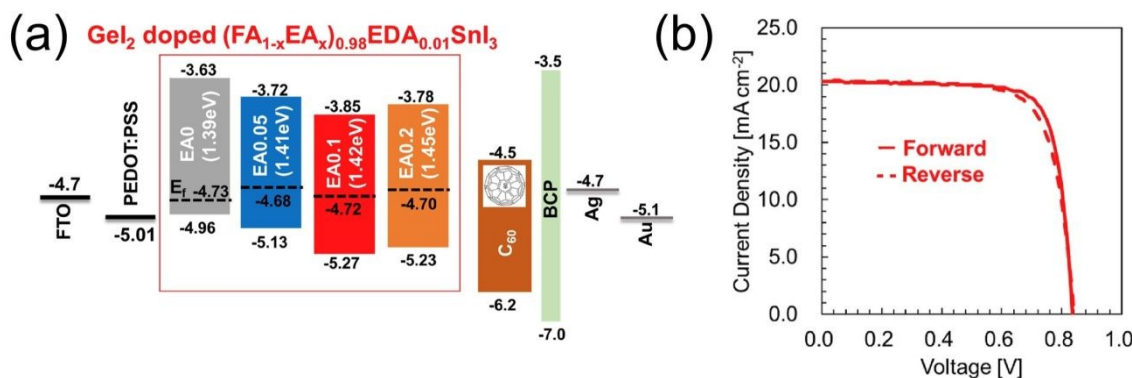


Figure 28 (a) Schematic diagram of the energy band levels for the inverted tin halide PSCs. (b) J-V curves of the best-performing PSC-based tin perovskite with EA0.1-EDA passivation. EA represents ethyl ammonium and EDA represents ethylene diammonium. (a) and (b),²⁷¹ Copyright 2020, Elsevier.

Hayase et al. followed a compositional engineering method by adding ethylammonium iodide (EAI) into the tin perovskite to form $(\text{FA}_{0.9}\text{EA}_{0.1})_{0.98}\text{EDA}_{0.01}\text{SnI}_3$.²⁷¹ The EA^+ cation incorporation aligned the energy levels of the perovskite to match that PEDOT: PSS and C₆₀ (Figure 28a), which helped to improve the built-in potential. EAI also works for suppressing the formation of traps and defects and reducing the lattice disorder of perovskite. Additionally, with the help of a post-treatment with edamine, the efficiency of the solar cells was promoted to 13.24% with a high V_{OC} of 0.84 V (Figure 28b). Similarly, a larger size divalent cation, ethylenediammonium (en) incorporated into tin perovskite lattice,²⁸⁸⁻²⁹⁰ serves as a cation of 3D structure but creates a high density of SnI_2 vacancies, forming a hollow 3D structure, which shows a larger

bandgap, lower trap-state density, much longer carrier lifetime and finally enhanced performance, compared with reference cells. In the trial of modifying the energy level of perovskite, the change in E_g is always inevitable, which may cause the deviation from optimal E_g , affecting the efficiency. In this context, constructing gradient energy alignment may facilitate the charge transfer without the necessity of altering the E_g of the light absorber. Han et al. reported a perovskite graded heterostructure, where a narrow-bandgap FASnI_3 dominates at the bulk and a wide-bandgap 2D $\text{TFBA}_2\text{SnI}_4$ ($\text{TFB} = \text{CF}_3\text{C}_6\text{H}_5\text{CH}_2\text{NH}_3^+$) is distributed with a gradient from bulk to the surface.²⁹¹ This heterostructure helps the electron extraction at the perovskite/C60 interface as a result of improved energy alignment between FASnI_3 and C60. The large steric hindrance effect of the TFBA molecule was thought to serve as an energy barrier to suppress the permeation of oxygen molecules and the subsequent oxidation of Sn^{2+} , which reduced the electronic trap states and the non-radiative recombination in FASnI_3 perovskite. As a result, the V_{OC} of 0.58 V with an efficiency of 8.53% was improved to 0.70 V with an efficiency of 10.96%. Larger molecules have been also introduced to the tin perovskite precursor to form a bulk heterojunction and facilitate the charge transfer.^{286, 292} A semiconducting molecule PTN-Br with HOMO level of -5.41 eV added to the FASnI_3 perovskite precursor was found to be located at the grain boundaries of the final perovskite crystals and the HOMO level of the molecule creates a gradient band alignment between perovskite (-5.59 eV) and PEDOT:PSS (-5.0 eV), promoting the hole transportation and V_{OC} output.²⁸⁶ Pushing down the WF of PEDOT:PSS to match with the energy level of perovskite can also avoid the change in E_g . For instance, a p-type dopant F4TCNQ deposited onto PEDOT:PSS film pushed down the WF of PEDOT:PSS from -5.04 to -5.18 eV, exhibiting more favorable hole extraction.²⁹³ This layer also suppressed trap density at the perovskite/HTM interface as a result of molecular interaction with the perovskite. Compared with the approach of modifying perovskite, constructing gradient energy alignment at the perovskite/HTM interface and modifying HTM looks more promising. This is because i) the optimal E_g of perovskite can be maintained; 2) some molecules with proper energy levels and certain functional groups can simultaneously work for controlling perovskite growth and reducing interfacial defects.

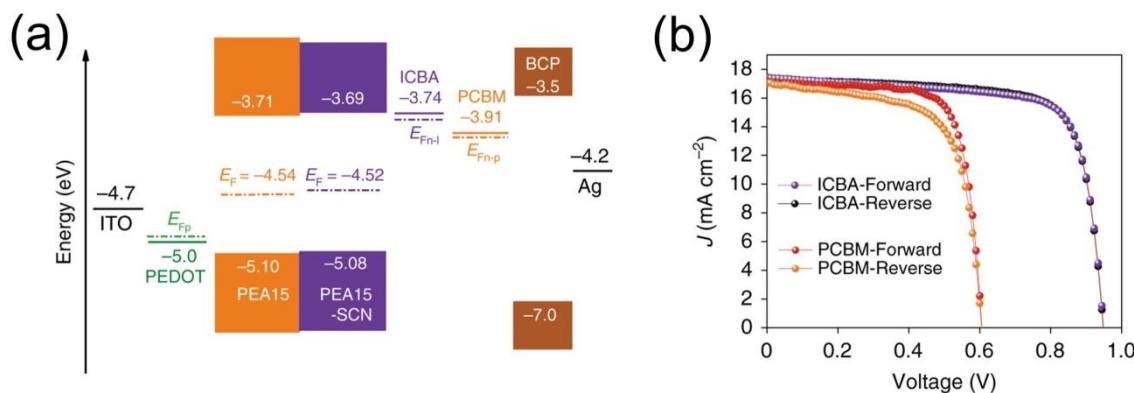


Figure 29 (a) Schematic illustration of energy levels. Dashed lines represent the quasi-Fermi level of ICBA (E_{Fn-I}), PCBM (E_{Fn-P}), and PEDOT (E_{Fn-P}). (b) J-V curves of the certified PEA15-SCN device with ICBA and champion device of PEA15-SCN film with PCBM. (a) and (b).¹⁸ Reprinted with permission from Nature

Publishing Group (2020).

Most research on band alignment for Sn-based PSCs are focused on the perovskite/HTM interface in an inverted structure, while the perovskite/ETL interface has not been given much attention. This can be attributed to the shorter hole diffusion length of Sn-perovskites than that of the electron,²⁹⁴ which makes the hole extraction at the perovskite/HTM interface more critical. However, there is also an energy level mismatch between perovskite and ETLs, such as C60 and PCBM.^{270, 287} This energy level offset can be a reason to lower the photovoltage. Elevating the LUMO level of ETL is possible to improve the V_{OC} of tin-based PSCs. Recently, indene-C60 bisadduct (ICBA), used in OPV and Pb PSCs,^{80, 295-297} with a shallower energy level (-3.74 eV) than that of PCBM (-3.91 eV) was employed as ETL in $\text{PEA}_x\text{FA}_{1-x}\text{SnI}_3$ (NH_4SCN) as an additive, $E_g=1.39$ eV-based PSCs (Figure 29a).¹⁸ Its better energy alignment with tin perovskite promises a larger attainable voltage. In addition, the shallow LUMO of ICBA prevents the electron injection from iodide, giving rise to less electron density and suppressed interface carrier recombination while the high electron density of PCBM, caused by remote doping from iodide (ion migration), aggravates the interface carrier recombination with p-type tin perovskite film.²⁹⁸ As a result, an unprecedentedly high V_{OC} of 0.94 V was accomplished with an efficiency of 12.4%, while the case using PCBM only shows a V_{OC} of 0.60 V and an efficiency of 7.7% (Figure 29b). This work emphasized the imperfection of the tin perovskite/ETL interface, such as energy level mismatch and carrier recombination. These problems are also observable for the Sn-perovskite/ETL interface of the normal (n-i-p) structure.

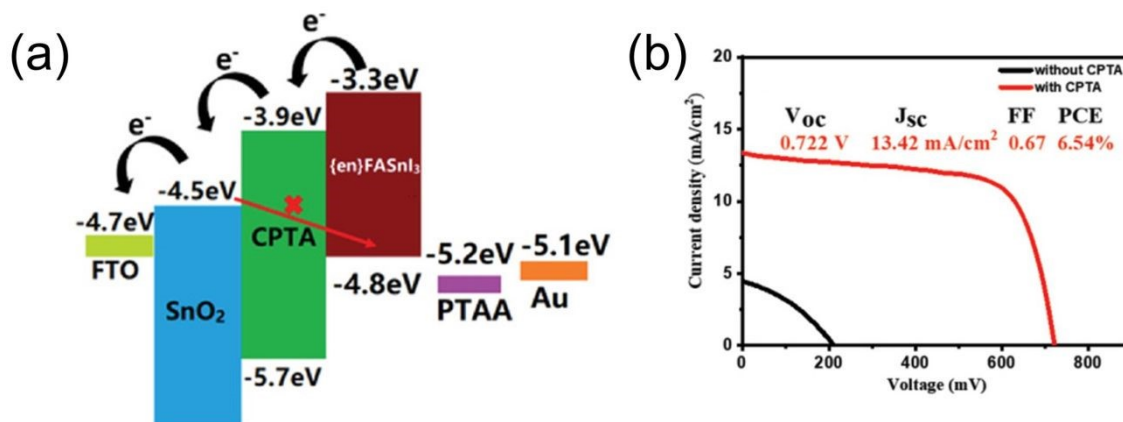


Figure 30 (a) Energy band alignment diagram of the tin-based PSCs. (b) J-V curves of tin-based PSCs with and without CPTA. CPTA represents C60 pyrrolidine tris-acid. (a) and (b),²⁹⁹ Copyright 2019, Wiley-VCH.

4.2.2 Tuning energy alignment in normal structure

In tin-based PSCs, the inverted (p-i-n) structure is much more popular than the normal (n-i-p) structure (more popular in Pb-based PSCs). Among the reported works, only approximately 10% of the total reports employed a normal structure, where V_{OC} and efficiency are always lower. From the point of view of the intrinsic property, the shorter hole diffusion length (193 nm) than that of electron (279 nm) of tin perovskite makes the inverted structure more suitable for tin perovskites. However, with the popular additive of SnF_2 ,

the carrier diffusion lengths of tin perovskite can exceed 500 nm, which means the device architecture should not limit the device performance.²⁹⁴ Some reasons accounting for the poor performance of tin-based PSCs in a normal structure have been reported. The most significant one, as mentioned above, is the large conduction band offset at the perovskite/ETL interface. For example, there is a big offset between the CB of tin perovskite and that of popular TiO₂ and SnO₂ ETL.³⁰⁰ Given that the V_{OC} of a solar cell is partly determined by the energy difference between ETL's CB and the perovskite's VB, too deep CB of ETL would limit the V_{OC} output.³⁰¹ Moreover, the electrons injected into ETL could recombine with the holes in tin perovskite, lowering the quasi-Fermi level of electrons. This easily happens because tin perovskites possess a p-type semiconductor property with a high background hole density, stemming from Sn²⁺ oxidation to Sn⁴⁺. Unlike the case of Sn-PSCs, the perovskite/ETL energy offset does not affect the V_{OC} strongly in the case of Pb-based PSCs. Lead perovskites are n-type semiconductors and the n-p junction formed at the perovskite/HTM interface leaves fewer holes for recombination at the perovskite/ETL interface. It means the energy offset at the perovskite/HTM interface is more important for lead perovskite solar cells while perovskite/ETL interface is critical for tin perovskite solar cells.^{259, 300} This agrees with our recent research on CsPbI₂Br solar cells, where PDTDT HTM with a smaller energy offset than that of P3HT displayed a much higher V_{OC} output. Therefore, TiO₂ and SnO₂ ETLs that are commonly used in lead PSCs are not suitable for tin-based solar cells because of their too deep CB and poor hole blocking ability. For reducing the energy offset, Nb₂O₅ with a much higher CB has been used as ETL in FASnI₃ cells, where the conduction band offset could be minimized to almost zero and a much-enhanced V_{OC} of 0.42 V was achieved.³⁰⁰ Kanatzidis's group reported a cascade structure of ETL by coating ZnS onto mesoporous TiO₂ in FASnI₃ cells.³⁰¹ ZnS has CB of -3.5 eV, much higher than that of TiO₂ (-4.2 eV), matches well with that of FASnI₃ perovskite (-3.3 eV), and significantly reduces the interfacial recombination and enhances the V_{OC} to 0.38 V. A C60 pyrrolidine tris-acid (CPTA)-modified SnO₂ used as ETL in n-i-p planar structure (en)FASnI₃ cell reduces the energy loss during electron transfer and efficiently suppresses charge recombination (block the holes) at the perovskite/SnO₂ interface (Figure 30a).²⁹⁹ As a result, a high V_{OC} of 0.72 V was achieved, while bare SnO₂-based devices show only 0.2 V (Figure 30b). One more possible reason that accounts for the low performance can be the formation of undesirable Ti-O-Sn bonds when tin perovskite contacts with TiO₂, which acts as traps and charge recombination centers.³⁰² This problem can be solved by inserting a fullerene layer between TiO₂ and tin perovskite to avoid their direct contact.

In most research using normal structure, the large energy offset at the perovskite/ETL (metal oxide) interface is regarded as the main problem while the offset at perovskite/ETL (fullerene) in the inverted structure is also quite large. For example, the energy offset in the case of GeI₂-doped (FA_{0.9}EA_{0.1})_{0.98}EDA_{0.01}SnI₃/C60 is as large as 0.65 eV, which is comparable to or even larger than that of FASnI₃/TiO₂.^{271, 300, 301} In addition, the LUMO of C60 (-4.5 eV) is lower than those of metal oxide ETLs in the normal structure, meaning a high possibility of recombination between injected electrons and holes in p-type tin perovskite. Nonetheless, a very high V_{OC} of 0.84 V was achieved in the former case even with a

0.65 eV energy offset.²⁷¹ Though the carrier transport mechanism between normal and inverted structures is not the same, the carrier recombination caused by energy offset can be similar. Therefore, we believe that the energy offset at the perovskite/ETL interface in the normal structure might not be the single and decisive factor for low V_{OC} and efficiency. Moreover, the properties of perovskite/metal oxide interface such as chemical bonds, electron transportation efficiency, and Sn^{2+} oxidation accelerated by oxygen vacancies on metal oxide surface should be considered for further development of normal structure tin-based PSCs.^{302, 303} As summarized above, efforts have been made to optimize the inverted structure devices to improve V_{OC} and PCE. If adequate attention can be paid to normal structure Sn cells, high performance might also be achievable, which could provide more options in designing single-junction and tandem solar cells. We also noted in the two seminal works on the normal structure, high V_{OC} (0.68 and 0.88 V) were already achieved using MASnI_3 ($E_g=1.30$ and 1.23 eV),^{259, 260} while they were not able to be repeated even by the same group.^{288, 301, 304} This poor repeatability can be attributed to the poor air stability of tin perovskite as well as some unknown reasons for tin-based solar cells. This poor stability also leads to diverse energy levels reported for the same tin perovskite. As we know, the tin perovskites are extremely sensitive to air and the solar cells were fabricated in an inert gas-filled glove box. But, for measuring PYS or UPS to determine the energy structure, tin perovskites have to be moved out of the glove box. This can result in different Sn^{2+} oxidation levels of the same tin perovskite, leading to diverse energy levels reported by different groups.³⁰⁵ In other words, the reported energy levels may not accurately reflect the energy match situation at the interfaces of tin perovskite solar cells.

In general, even though the tin perovskites with narrower bandgaps have smaller theoretical E_{loss} according to the S-Q limit, they are suffering from severe E_{loss} . The main reasons lie in the high defect level caused by Sn^{2+} oxidation tin perovskite and poor interfacial carrier transportation caused by energy level mismatch, both of which lead to serious non-radiative recombination and low V_{OC} output. As summarized above, methods of controlling the crystal growth, suppressing the Sn^{2+} oxidation, and optimizing the interfacial energy alignment have been developed, which has promoted V_{OC} approaching 1.0 V. For further enhancing the V_{OC} and efficiency for tin-based PSCs, on one hand, the defects in perovskite need to be minimized. The fast crystallization of tin perovskites can be retarded by additives, generating films with much better morphology. However, better morphology doesn't always mean fewer defects and less non-radiative recombination. Besides the well-known Sn^{2+} -oxidation-related defects, other defects including vacancies, undercoordinated ions, and ion migration that can play important roles must be studied. On the other hand, the interfacial carrier transport/properties need intensive studies to have an accurate understanding. As mentioned above, the widely accepted energy level mismatch at the perovskite/HTM and perovskite/ETL interface may not be reliable because of the inevitable change of perovskite during measurement. The interface property related to the non-radiative recombination such as perovskite surface defects and undesirable interaction between perovskite and carrier extraction layers needs to be investigated. This is quite important for a better understanding of the reasons why tin perovskites are more suitable for inverted structures rather than normal structures. We believe that with adequate study and effort, the energy loss of

tin-based solar cells can be further reduced and higher V_{OC} will be achieved. This is also quite meaningful for tin perovskite working as a bottom-cell of a tandem cell, offering a higher contribution to the total V_{OC} output.

5 Bismuth perovskite (analog) solar cells

As the adjacent element to Pb in the periodic table, trivalent Bi³⁺ cation has a similar electronic configuration and ionic radius as Pb and Sn, and therefore, has been used to partly substitute Pb²⁺ cation at the B sites of lead perovskites.^{184, 185, 306} For example, in an earlier study, Bi³⁺ doping of CsPbI₃ was reported to improve the performance of CsPbI₃ solar cells although a recent study found that the Bi³⁺ doped CsPbI₃ is not a thermodynamically favored system despite a better tolerance factor.¹⁸⁵ Pure Bi³⁺-occupied B site, neutral perovskite with the formula of ABX₃ (A=Cs, MA; X=I, Br, Cl) is not possible because of the +3 valence state.³⁰⁶ Instead, it forms ternary Bi³⁺-based perovskites that exist in structures with a formula A₃Bi₂X₉ (A = MA⁺, Cs⁺ or Ag⁺, and X = I⁻ or Br⁻), where three Pb²⁺ are replaced by two Bi³⁺ to maintain the charge neutrality, and they form a 2D or 0D structure with face-sharing octahedral, unlike 3D CsPbI₃ or MAPbI₃ perovskite that exist in corner-sharing octahedra. In addition, several Bi-based halides with structures different from cubic perovskites, and even with non-perovskite structures have been found to work as a replacement for toxic lead perovskite light absorbers.^{144, 307, 308} All of these reported Bi-based halides can be divided into four kinds according to the formula: BiX₃, A₃Bi₂X₉, A₂AgBiX₆, and Ag_aBi_bX_{a+3b}. This section summarizes recent advances in improving the V_{OC} of Bi-based halide solar cells.

The application of BiX₃ in photovoltaics has been reported over 50 years ago.³⁰⁷ Among all the three halides of Bi, BiI₃ is much more popular than BiBr₃ and BiCl₃ in the photovoltaic area, but its development is still quite slow, with the champion efficiency reaching only 1.21% with a V_{OC} of 0.61 V so far. Such low PCE is mainly regarded to its E_g of ~2.0 eV,³⁰⁹ and short carrier lifetime (1 ns), meaning short diffusion length of carriers and heavy recombination before extraction.^{309, 310}

5.1 Low-dimensional A₃Bi₂X₉ solar cells

Two-dimensional (2D) or zero-dimensional (0D) A₃Bi₂X₉ materials such as MA₃Bi₂I₉, FA₃Bi₂I₉, and Cs₃Bi₂I₉ have been used as light absorbers because of their high humidity stability. Research efforts have been made to enhance the device performance by optimizing the fabrication method, precursor, and additive engineering.^{144, 311-313} Though the highest PCE of 3.2% has been achieved for Cs₃Bi₂I₉ cell,³¹⁴ rest of the reports have shown PCE below 1%.³⁰⁷ As the wide bandgap of A₃Bi₂X₉ was considered one of the factors that limit the performance, attempts have been made to decrease the bandgap. Sulfur incorporation is regarded as an effective way to decrease the bandgap of A₃Bi₂X₉ materials. For instance, Hayase et al. incorporated sulfur into MA₃Bi₂I₉ through in-situ thermal decomposition of Bi(xt)₃ (xt=ethyl xanthate), which remarkably reduced the E_g from 2.1 to 1.45 eV.³¹⁵ A similar process was reported by Yao et al., where E_g was decreased to 1.67 eV but the efficiency was still as low as 0.15%.³¹⁶ Therefore, E_g may not be the decisive factor for poor performance. Instead, the physical properties of A₃Bi₂X₉ materials including

low-dimensional structure, indirect bandgap, high Wannier-Mott exciton binding energy, and high background charge carrier densities make them not suitable light absorbers for photovoltaic applications.³¹⁷⁻³²¹

5.2 A₂AgBiX₆ double perovskite solar cells

In addition to A₃Bi₂I₉, A₂AgBiX₆ double perovskite where two B-site divalent cations are replaced with a monovalent cation (Ag⁺) and a trivalent cation (Bi³⁺) have attracted quite a good amount of attention in recent years.³²² A₂AgBiX₆, especially Cs₂AgBiBr₆, has been studied as a light absorber because of its merits of toxicity-free, good moisture stability, and more importantly, the expected similarities between its property and the properties of APbX₃ analogs, such as long carrier lifetime.^{323, 324} Cs₂AgBiBr₆ has been incorporated into both normal and inverted configuration, showing PCEs in the range of 1~3%.³⁰⁷ Perovskite film quality is an important factor determining the device's performance. For preparing good Cs₂AgBiBr₆ film, both spin-coating and vacuum deposition processes have been explored.³²⁵⁻³²⁷ In a comparative study, Yang et al. found that the solution-processed Cs₂AgBiBr₆ film has higher crystallinity, a narrower bandgap, longer photoexcitation lifetime, and higher mobility than those of the vacuum-sublimated one.³²⁷ As a result, an enhanced PCE of 2.51% was achieved, where J_{SC} was the main contributor while the V_{OC} (1.01 V) was slightly lower than the vacuum-processed one (1.05 V). Wang and co-workers reported several chlorophyll derivatives working as HTM or ETL in Cs₂AgBiBr₆ solar cells.^{328, 329} They achieved a champion PCE of over 3% where the main contribution also came from photocurrent rather than V_{OC}. However, a remarkable V_{OC} enhancement was realized using inorganic Cu₂O as the HTM.³³⁰ Because of its good electrical properties and well-matched energy level with Cs₂AgBiBr₆, the V_{OC} was promoted to a record-high value of 1.20 V from 1.08 V observed in the case of Spiro HTM. But the PCE (1.52%) in the case was not impressive due to lower J_{SC} than other reported values.^{307, 328} The high V_{OC} achieved with Cu₂O implies the importance of interface charge transportation, and the carrier extraction materials developed for Pb-based PSCs don't perfectly match with Pb-free materials. For instance, the energy offset at the Cs₂AgBiBr₆/Spiro interface approaches 1.0 eV.³²⁵ It is believed that by employing HTMs with suitable energy levels and excellent carrier extraction ability, higher V_{OC} and efficiency can be achieved. Cs₂AgBiBr₆ solar cells have also used an inverted structure. Wu and co-workers developed an inverted structure of ITO/Cu-NiO/Cs₂AgBiBr₆/C60/BCP/Ag achieving a remarkable PCE of 2.23% and a V_{OC} of 1.01 V.³³¹ Besides Cs₂AgBiBr₆, the formation of another double perovskite, Cs₂NaBiI₆, has been also reported.^{332, 333} However, this has not been used in the solar cell, except in one study, because of its poor stability. It has been observed that over half of the target material, Cs₂NaBiI₆ powder, synthesized by a hydrothermal method, easily decomposes to Cs₃Bi₂I₉ during the cooling process, indicating the thermal instability of Cs₂NaBiI₆. Finally, only a mixture of Cs₂NaBiI₆ and Cs₃Bi₂I₉ remains and this has been used as a light absorber. The device showed a PCE of 0.42%, which is quite similar to that of Cs₃Bi₂I₉ solar cells. In summary, double perovskite can be a promising Pb-free candidate, but the efficiency is still quite low. Though they have wide E_g, considerable J_{SC} should be achievable as long as efficient carrier separation and transport are promised. According to the S-Q limit, Cs₂AgBiBr₆ with a direct bandgap of ~ 2.2 eV should

be able to work with an efficiency of ~18%. The V_{OC} of ~1.0 V, which is a rather low value for a material that absorbs at energies > 2.2 eV and shows a PL peaking between 610 and 630 nm (2 eV), suggests high non-radiative recombination losses. In a recent study where Maximilian et al. compared the performance of $Cs_2AgBiBr_6$ solar cells made in different architecture and hole transport materials, it was evident that significant carrier loss (recombination) occurs at the selective contacts, i.e. the HTM or ETL.³³⁴ Hence, we believe that better interfacial energy alignment and suppressed recombination are critical to achieving higher V_{OC} , which may be realized by developing more suitable HTMs.

5.3 3D $Ag_aBi_bX_{a+3b}$ perovskite solar cells

5.3.1 Making high-quality $Ag_aBi_bX_{a+3b}$ film

$Ag_aBi_bX_{a+3b}$ materials, with a 3D crystal structure, are the most popular Bi-based light absorbers. According to the stoichiometric ratio of AgI/BiI_3 , $Ag_aBi_bX_{a+3b}$ has compositions of $AgBi_2I_7$, $AgBiI_4$, Ag_2BiI_5 , and Ag_3BiI_6 . Though these ternary bismuth iodides have different crystal structures (space groups),³⁰⁷ they have similar $E_g \sim 1.80$ eV, which makes them suitable for photovoltaic applications.³³⁵⁻³³⁷ Sargent et al. firstly reported $AgBi_2I_7$ based devices and obtained a PCE of 1.22%, where n-butylamine was used as the solvent for AgI and BiI_3 .³³⁸ However, the V_{OC} of 0.56 V achieved here was low and the efficiency was not reproducible because of the compositional change at the high annealing temperature.³³⁹ In one of our earlier studies, we changed the solvent to DMSO and annealed the active layer at a low temperature (100 °C).³⁴⁰ Compared with the case of n-butylamine, the film obtained using DMSO as the solvent showed uniform grains without pinholes and smooth interfaces with neighboring charge transport layers (Figure 31a). As a result, the PCE was promoted to 2.2% with a V_{OC} of 0.62 V (Figure 31b). It was also found that the remnant BiI_3 in the film plays an important role in enhancing efficiency and stability. While high-quality Ag-Bi-halide film preparation looked a little difficult by solution process, Mitzi et al. used a two-step co-evaporation/annealing approach to form high-quality $AgBi_2I_7$, $AgBiI_4$, and Ag_2BiI_5 films.³⁴¹ Initial studies on the photovoltaic performance showed that the $AgBiI_4$ ($E_g=1.80$ eV) based device exhibited quite a high V_{OC} of 0.84 V, but the PCE was only 0.89%. Xiao's group achieved a high V_{OC} of 0.83 V (maintaining high efficiency of 2.80%) by introducing Li-TFSI into the $AgBiI_4$ precursor for obtaining high-quality film and using PTAA as the HTM (Figure 32a and b).³⁴² Higher V_{OC} of 0.88 V was obtained with thicker $AgBiI_4$ film, but it showed lower J_{SC} , indicating the short carrier diffusion length of $AgBiI_4$.

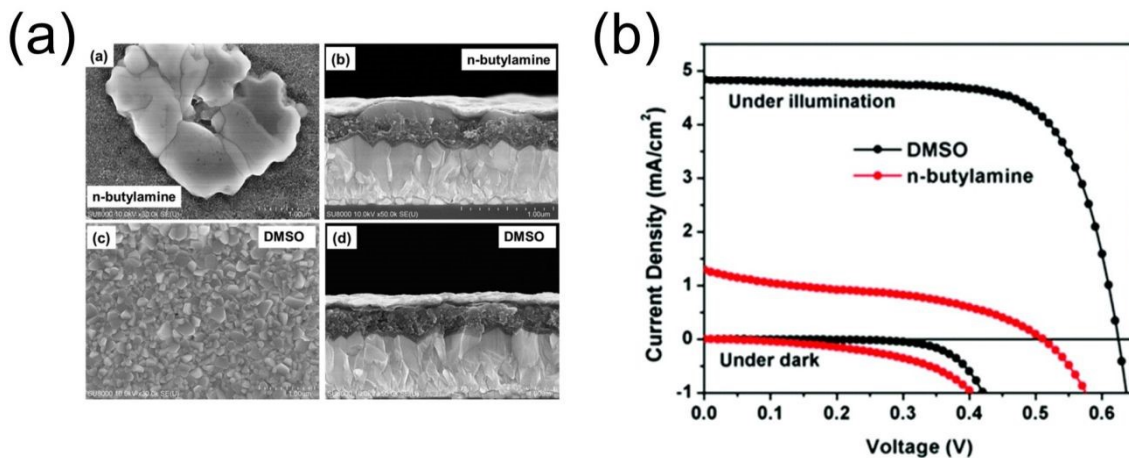


Figure 31 (a) The top and cross-sectional SEM image of AgBi₂I₇ film obtained from n-butylamine and DMSO. (b) J-V curves of the best performing devices based AgBi₂I₇ film obtained from n-butylamine and DMSO. (a) and (b),³⁴⁰ Copyright 2019, Royal Society of Chemistry.

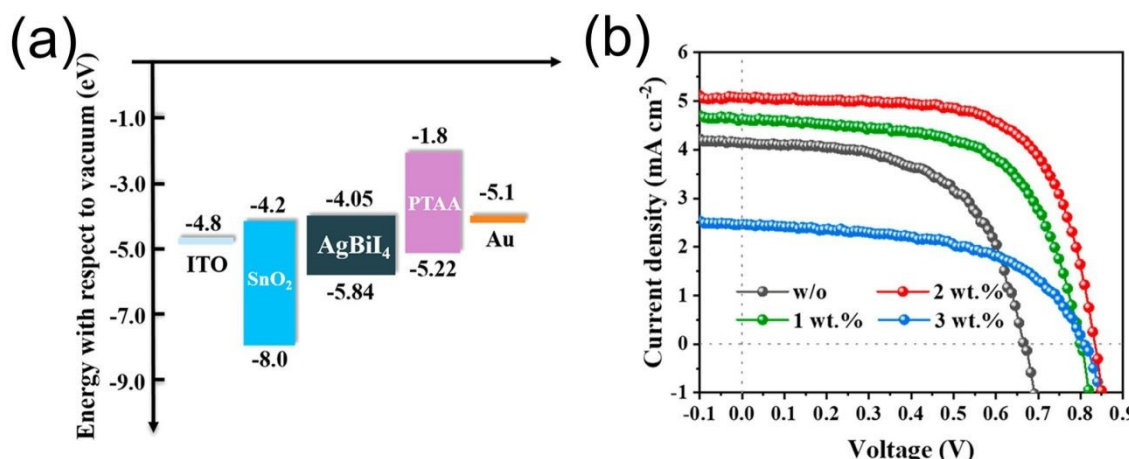


Figure 32 (a) Band alignment diagram of AgBiI₄ solar cells. (b) J-V curves of solar cells based on AgBiI₄ with various Li-TFSI additive concentrations. (a) and (b),³⁴² Copyright 2019, American Chemical Society.

5.3.2 Tuning energy alignment with CTls

Similarly, in our recent research, we found the semi-transparent (thin) Ag₂BiI₅ shows much better J_{SC} and V_{OC} than cells employing the non-transparent (thick) Ag₂BiI₅ film. With an amorphous SnO_x as the ETL and a polymer with proper HOMO level working as HTM, this semi-transparent Ag₂BiI₅ light absorber can work with a high V_{OC} of 0.88 V and PCE of 2.65%. It is to be noted that this SnO_x layer which produced high V_{OC} in our CsPbI₂Br cells also worked well for Ag₂BiI₅ cells, indicating the universality of the amorphous SnO_x ETL. More importantly, the energy alignment between the light absorber and HTM always plays a crucial role. Although we have not yet thoroughly verified the performance of this Ag₂BiI₅ solar cell with other HTMs like P3HT, some preliminary experiments show that polymer HTM with a better HOMO level matching with Ag₂BiI₅ works better than P3HT. Nevertheless, we also believe that the

optimum condition of any HTM on Ag_2BiI_5 can depend and vary with the other layers like ETL in the device. We are now trying to understand further this specificity of the device structure towards HTM/ETL. Nonetheless, the semitransparent Ag_2BiI_5 cells, which we considered good for indoor or windows applications, also showed an encouraging low-light performance. For example, a cell working with a PCE of 1.6% under one sun was found to work with an efficiency of 5.7% under 1000 lux. This PCE is comparable to that of recently reported $\text{Cs}_3\text{Sb}_2\text{Cl}_x\text{I}_{9-x}$ solar cells,³⁴³ but the Ag_2BiI_5 cells in our case demonstrated a higher V_{OC} (0.64 V). We are presently trying to further improve the performance of this semitransparent cell by improving the compositional/phase purity, which we suspect to be a major issue with this material. As indoor photovoltaics have a stringent requirement of non-toxic materials because the appliance would be closer to our daily life, and the bandgap of 1.8 eV of $\text{Ag}_a\text{Bi}_b\text{X}_{a+3b}$ is optimum for indoor light (spectrum match), more efforts should be put into the development of these materials/devices. Except for developing advanced encapsulation techniques for Pb-containing cells, developing Pb-free indoor photovoltaics is certainly a wise choice, considering the practical application.

In summary, bismuth halides, especially $\text{Ag}_a\text{Bi}_b\text{X}_{a+3b}$, are potential substitutions for lead perovskites because of their high environmental stability and non-toxicity. But, the incomparably low efficiency of the cells employing these halides creates a cloud over the actual potential of these materials. As of now, the highest efficiency for the device using pure bismuth-halide compound (Ag_3BiI_6) is 4.3%,³³⁵ which was improved to 5.56 % by doping sulfur, i.e. $\text{Ag}_3\text{BiI}_{5.92}\text{S}_{0.04}$.³⁴⁴ However, all these values fall far behind the theoretically estimated values for silver-bismuth halides. According to the S-Q limit, these halides with E_g of 1.8 eV can work with PCE of above 25%. Roughly, it can be estimated that these devices suffer a loss of 13 mA/cm² of photocurrent and 1.0 V of open-circuit voltage. Despite their strong absorption and E_g of 1.8 eV, such low performance can be due to intrinsic defects in the material. As we have observed, Ag_2BiI_5 which works with a PCE of 2% does not show any photoluminescence, indicating significant carrier loss by non-radiative recombination. Hence, investigation of possible defects and their generation during the processing of these halides is very important at the present stage. Besides, quite a few reports have presented measured band levels, carrier type, and the carrier density of these halides. This is also important to find more suitable ETL and HTM for making an efficient device. The V_{OC} is quite an important parameter for indoor photovoltaic because under indoor light, only a small quantity of carriers is generated and severe non-radiative recombination (reflected by low V_{OC} under sunlight) consumes most of them, leaving few carriers for the photovoltaic performance. Therefore, low V_{OC} of bismuth halides-based cells show that they still have a long way to go. For further improving the device performance, it is believed that the following aspects need to be considered. Firstly, the properties of light absorption materials should be modified by compositional engineerings, such as sulfur doping, for achieving narrower E_g and longer diffusion length. Secondly, a high-quality film with suppressed SRH recombination is necessary, which can be realized by more suitable fabrication processes. Most importantly, the phase purity and compositional homogeneity in the polycrystalline films, which we believe to be a serious issue with these halides, must be checked for finding correct approaches for further improvement. Finally, similar to the problem in tin PSCs, the charge

transporting materials, especially previously developed HTMs seem not to be suitable for bismuth-halide materials. The mismatched energy level between HTM and light absorber must be one reason for poor V_{OC} output. Novel HTMs with proper energy levels and good hole transporting ability should be developed to further enhance the performance. With increased V_{OC} output, bismuth halide cells will be more promising for indoor application than working under sunlight.

6 Summary and outlook

6.1 Current research summary

In comparison to PV technologies like CdTe, DSSC, and OPV that use absorbers with bandgap similar to perovskites, PSCs show remarkably high V_{OC} , or minimum energy loss. Figure 33 shows a summary of the reported champion V_{OC} for PSCs using perovskites with varied bandgaps. Pb-based hybrid PSCs have a substantially lower E_{loss} (< 0.4 eV) than other types of PSCs. The PSCs employing Sn and Sn/Pb-based perovskites with narrower bandgap and theoretically smaller E_{loss} than hybrid solar cells always show more severe E_{loss} (as large as 0.81 eV). The PSCs using wide bandgap all-inorganic perovskites, despite their high V_{OC} compared to PV cells with similar bandgaps (a-Si and DSSC), are still suffering from large E_{loss} (0.38~0.69 eV). Although it is anticipated that solution-processed perovskites would have a lot of defects and suffer from severe performance loss linked to these defects, their defects-tolerance nature helps them achieve high V_{OC} with minimum energy loss. However, it must be noted that the defect tolerance property of perovskites only refers to the intrinsic crystal defects in the perovskites but the extrinsic defects like pinholes and grain boundaries in the polycrystalline films, interfacial imperfections at ETL and HTM can influence the overall device performance significantly.

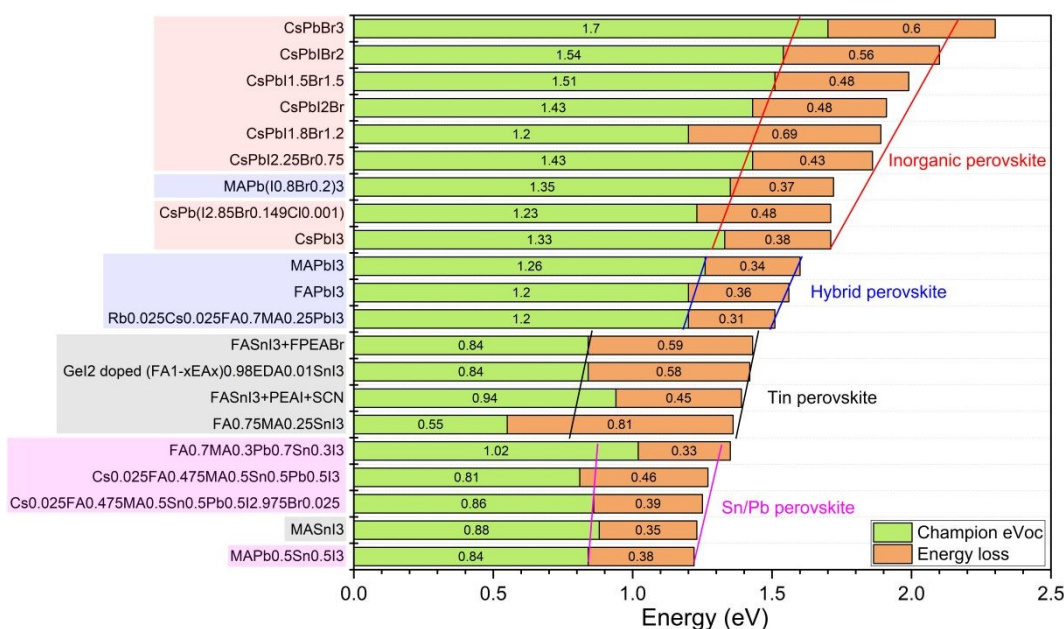


Figure 33 Summary of champion V_{OC} for various kinds of perovskite-based solar cells.

Hence, to minimize the energy loss (V_{OC} loss), methods have been developed to make high-quality perovskite films with no pinholes and fewer grain boundaries (large grains) and different strategies have been followed to passivate the surface and interfacial defects. Solvent and compositional engineering, controlled crystallization, and the use of additives in the precursors lead to the formation of films with large grains, resulting in improved V_{OC} . In many studies on hybrid perovskites, $MACl$ has been added in excess to improve the film quality and thereby the performance. We also found that the addition of $MACl$ to mixed-halide-mixed-cation perovskites could help in the incorporation of Ge into the mixed perovskites, resulting in better V_{OC} and PCE. Here, Ge at the grain boundaries and on the surface passivates the defects and thus improves the V_{OC} by suppressing the recombination loss. Many methods similar to those followed in the case of hybrid perovskites have been used for fabricating high-quality all-inorganic and Sn-based perovskites. For example, intermediate controlling, metal doping, and the use of additives like $MACl$, $EDAI_2$, NH_4SCN , etc., have been found to improve the morphology of the perovskite film by removing pinholes and enlarging the grains, and hence, have increased the V_{OC} . However, in general, the film quality of hybrid perovskites is often superior to that of all-inorganic and Sn-perovskites. One important reason is that a much larger number of studies have been done on hybrid perovskites than that undertaken for the latter, by improving the crystallization process to optimize the film morphology. This can partly explain why the V_{OC} of hybrid PSCs are approaching the theoretical values in some cases while the other perovskites are lagging. In other words, the recombination in other perovskite films is still a problem. For Sn and Sn/Pb perovskites, the fast crystallization results in poor film quality with a lot of defects, and the easy oxidation of Sn^{2+} to Sn^{4+} further aggravates the defect situation. Additionally, with the short lifetime and diffusion length of carriers in Sn perovskite, most photon-generated carriers are trapped and recombined in the perovskite film before being extracted, resulting in poor device performance. For the all-inorganic perovskites, careful control of the intermediate phase and stepwise annealing are critical to fabricating uniform films. Another challenge with all-inorganic perovskites is the easy transition of the perovskite phase to the non-perovskite phase, which can act as the carrier recombination center, harming the voltage output. Although a recent theoretical study shows that all-inorganic perovskites can be even more defect-tolerant than hybrid perovskites like $MAPbI_3$, relatively more energy loss in the former must be linked to the phase instability. Therefore, forming phase pure all-inorganic perovskites and keeping the photoactive phase under ambient operational conditions is going to be the key to enhancing the V_{OC} further. In the case of Bi-based halides like $Ag_aBi_bX_{a+3b}$, the energy loss is huge, even more than 1.0 eV. One of the reasons for such poor performance of Ag-Bi-halides is relatively poor film quality in comparison to perovskites. But, although there is hardly any study about the intrinsic defects in these materials, it seems that these materials suffer severely from intrinsic defects, which seek serious attention.

While suppressing non-radiative recombination in the bulk of the perovskite film is important to minimize the energy loss, recombination occurring at the interfaces between CTLs and perovskite, which lowers the QFLS and restricts the V_{OC} output, also holds great significance in improving the V_{OC} . Generally, the ETL should extract the electrons and block the holes at the perovskite/ETL interface. The small interfacial

Schottky barrier and the defects in ETLs can lead to poor blocking effect and more carrier recombination. We found that an ultra-thin dense SnO_x ETL with a higher CB could suppress the interface recombination. With the good hole blocking effect of SnO_x ETL, high V_{OC} is achievable in different cells using hybrid and all-inorganic perovskites, as well as bismuth-based light absorbers. Another factor giving rise to energy loss is the energy level mismatch between perovskite and CTls. The well-developed ETLs and HTMs are more suitable for hybrid perovskites but are not perfectly matching other light absorbers such as Sn-based, Sn/Pb-based, CsPbX_3 perovskites, and bismuth-based materials. The imperfect energy level alignment lowers the QFLS of the light absorber, generating poor V_{OC} output. In one of our studies, we found that P3HT with HOMO of -5.00 eV, when used as HTM for CsPbI_2Br (VB of -5.77 eV) solar cells, yields a champion V_{OC} of 1.32 V. While in the case of spiro-OMeTAD with a deeper HOMO of -5.22 eV, the V_{OC} increases to 1.37 V, and a newly developed HTM (PDTDT) with a HOMO of -5.44 eV promotes the V_{OC} to 1.42 V. This work convincingly verifies the importance of energy level matching between perovskite and CTls, which must be paid attention for reducing the energy loss. As a solution, new ETLs and HTMs that well match different light absorbers must be explored for suppressing the interfacial recombination and maintaining the QFLS from the light absorber. In other words, for reducing the energy loss, the carrier extraction from perovskite and transfer through the interfaces are equally important to the carrier separation and transport in the perovskite.

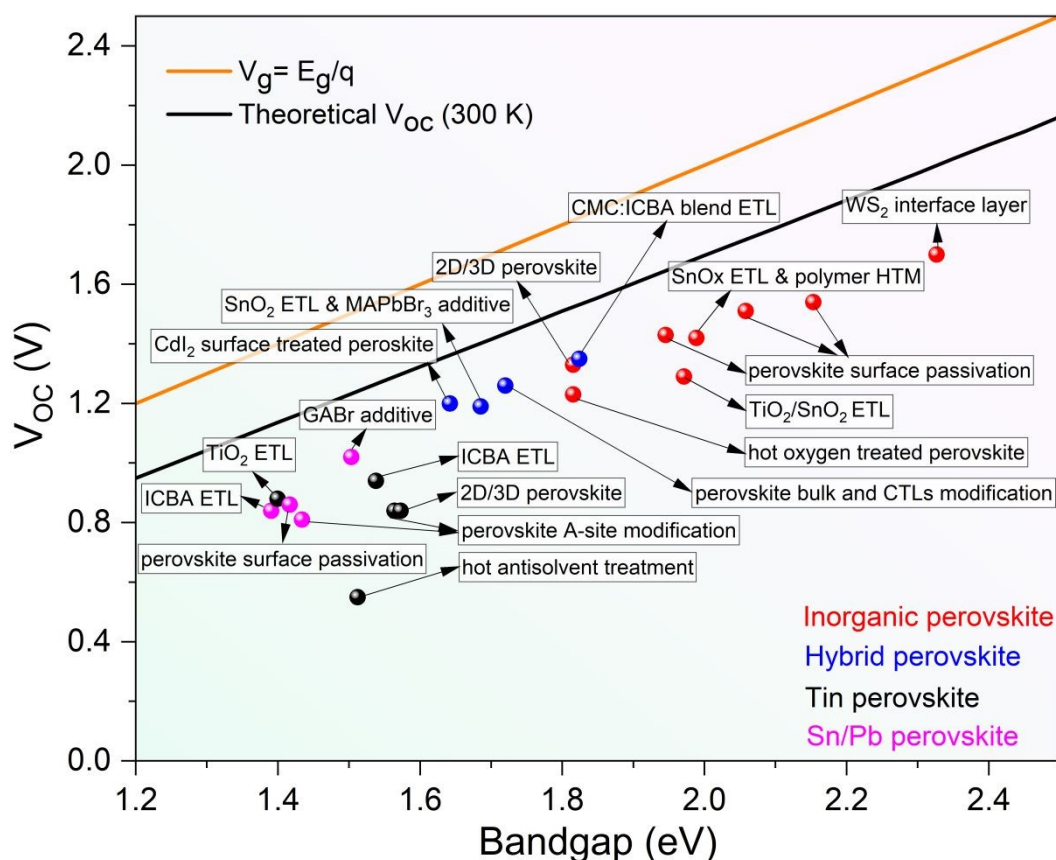


Figure 34 Approaches to achieving champion V_{OC} for various kinds of perovskite-based solar cells.

Figure 34 depicts the techniques for achieving champion V_{OC} for various types of perovskite-based solar cells. Though perovskite quality (composition, defects, and morphology) is significant, the perovskite surface and the interfaces with CTLs are becoming increasingly important in promoting the V_{OC} output. Many efforts have been made to passivate the perovskite surface defects, optimize the interface charge transport, and develop more appropriate CTLs. In the future, we anticipate that reducing carrier non-radiative recombination at interfaces will be more promising than that in light absorber bulk for increasing V_{OC} .

High V_{OC} is a prerequisite for developing high-performance perovskite module cells. As is known to all, when comparing the PCE values of small-area cells and large-area modules, a considerable discrepancy is observable. Although the V_{OC} gap is the smallest among the three photovoltaic parameters (J_{SC} , V_{OC} , and FF),³⁴⁵⁻³⁴⁷ it becomes severe when the module size exceeds 100 cm². The main reason for V_{OC} reduction is the reduced shunt resistance, which is caused by several factors, including 1) pinholes, 2) particulates, 3) interconnects (P1 and P3 are not clean/resistive enough; the P3 process damages the surrounding perovskite, causing leakage), 4) nonuniformity (if a particular area in a particular layer is too thin), and 5) a lack of proper edge isolation patterning (P4).³⁴⁷ Therefore, making uniform and pinhole-free perovskite film, as well as refining the structure and quality of module cells, would help to improve the V_{OC} for industrial-friendly deposition processes.

High V_{OC} will also benefit the application of PSCs as indoor photovoltaics. Under the weak indoor light (1% intensity of the sunlight), only a small number of carriers are generated, and most of them can be trapped by the defects, leaving few carriers for photovoltaic output. That is to say, indoor photovoltaics are more sensitive to defect levels (dark leakage current) and even a small leakage current can have a big influence on V_{OC} reduction. The high V_{OC} of PSCs (under sunlight) represents a low defect level and low dark leakage current, which means the indoor light-generated carriers can be collected and transported efficiently over the interfaces. Perovskite light absorbers with the advantage of E_g tunability can match well with the spectra of the various light sources such as a fluorescent lamp and LED light. It is known that E_g of 1.8 eV and 1.9 eV are optimum for indoor applications with LED and fluorescent lamps as illumination sources respectively. Several perovskite compositions match these values. As long as the high voltage of these PSCs is retained, the indoor perovskite photovoltaic will be a very promising application. We recently studied the indoor performance of CsPbI₂Br (1.91 eV) solar cells. Thanks to the highly suppressed recombination by the SnO_x layer (high V_{OC} of 1.42 V under the sunlight), we achieved 1.23 V V_{OC} under 1000 lux indoor LED light (300 μ W cm⁻²) and over 32% PCE. The value of PCE has been maintained at 34% under 200 lux illuminance (60 μ Wcm⁻²) with a V_{OC} of 1.14 V. Under indoor illumination, amorphous SnO_x is thought to act as an insulating thin layer, decreasing the leakage current. Notably, V_{OC} exceeding 1.1 V is rarely obtained for both indoor and commercialized high-performance PV cells. This situation manifests the potential of indoor PSCs as energy harvesters for the self-powered Internet of Things.

Measuring a reliable V_{OC} output for cells employing strategies to reduce interfacial recombination is

important because many studies reporting high V_{OC} also present the J-V curves with severe hysteresis, showing the substantial difference in the V_{OC} values measured under forward and reverse scan directions. This certainly leads to erroneous estimation of performance and unfair comparison to other studies. To reduce the non-radiative recombination in perovskite and at the interface, some extra layers, molecules, or ions are introduced into the device. These materials were proved to be effective in suppressing the recombination, but may also hinder the charge transfer and result in charge accumulation at the interface, causing unbalanced charge transport and finally severe hysteresis. Thus, in the development of strategies for promoting V_{OC} , the negative effects of the materials being employed in the device should also be considered.

In summary, improving V_{OC} is the key to further promoting the efficiency of PSCs and expanding their application prospects. Strategies that suppress the non-radiative recombination in the light absorber and the interfaces have been proven to be effective in reducing energy loss. We believe that with further enhancement of V_{OC} and efficiency, the commercial perspective of perovskite photovoltaic will be enhanced. It is believed that the serious non-radiative recombination caused by defects in perovskites and interfaces is the main reason for E_{loss} . Note that non-radiative recombination is also partly responsible for the FF loss. That is to say, suppressing recombination can lead to the improvement of V_{OC} and FF simultaneously. Therefore, V_{OC} enhancement is critical to further improvement of the PSCs' performance.

6.2 Future outlook

The GaAs crystalline cell ($E_g = 1.42$ eV) that shows V_{OC} (1.2 V) close to the S-Q limit, is the engineering model of high V_{OC} best PV cell. In the future, thoroughly reducing charge recombination loss inside the perovskite bulk by minimizing defect density (impurity) as well as at the hetero-junction interfaces is necessary to improve the V_{OC} of PSCs. Making high-quality light absorber film is still required, especially for all-inorganic and tin perovskites. For all-inorganic perovskites, the stepwise annealing, which is often followed for obtaining a uniform film, might generate compositional inhomogeneity as well as defects. Moreover, the phase transition to the photo-nonactive phase from the perovskite phase, even not detectable by XRD, must be critically affecting the V_{OC} output. Therefore, we believe, direct measurements of composition distribution and crystal phase impurity in the films, which have not received much attention, are going to help us find ways to improve V_{OC} as well as PCE of inorganic PSCs further. For Sn and Sn/Pb perovskites, the fast crystallization of perovskite results in low film quality, which needs to be improved. The suppression of Sn^{2+} oxidation to Sn^{4+} that introduces defects is another obstacle to be overcome for achieving higher V_{OC} and efficiency. The high quality of bismuth halides film is also important for developing efficient lead-free solar cells. While the intrinsic property studies of bismuth halides are more urgent to better understand how the big loss in V_{OC} and PCE generates. Though the E_{loss} in hybrid PSCs is quite low, further suppressing the non-radiative recombination is still meaningful to efficiency enhancement since the undesirable recombination is also partly responsible for the FF loss, which now is the biggest weakness of hybrid PSCs in achieving efficiency approaching the S-Q limit.

The equally important issue is interface recombination. Thermodynamically, the E_{loss} of ca. 0.2 eV is inevitable at room temperature for enabling unidirectional carrier transfer at the interface. As a result, the minimal E_{loss} that occurs at the ETL/perovskite and perovskite/HTM interfaces is 0.4 eV in total. In other words, we must reduce an interfacial E_{loss} to 0.2 eV to minimize the V_{OC} loss. One approach is to build a physically continuous heterojunction without producing defects or impurities, which also needs a flat perovskite polycrystal surface. The current (charge transfer) rectification ability of CTLs should also be enhanced to minimize interface recombination. The widely used ETLs and HTMs borrowed from other PVs such as DSSC and OPV are not perfectly matching perovskite photovoltaics. As previously stated, the hole blocking ability of ETL (such as amorphous SnO_x layer) as well as the electron blocking ability of HTM, and the energy level matching with perovskite are important in suppressing the recombination. Therefore, exploring more suitable CTLs that enable efficient extraction and suppress non-radiative recombination of photogenerated carriers would also be very helpful.

Though numerous strategies for producing high V_{OC} of various PSCs have been established, research on the mechanisms that drive such processes is still insufficient. For example, metal ion doping has been used to inhibit perovskite bulk recombination, and the same metals have been utilized in different types of perovskites. However, the fundamental question of where foreign ions are located remains unanswered and the actual working mechanisms are still unclear. Furthermore, trap passivation engineering has been widely documented for perovskite and CTL surfaces, but the mechanisms are unclear in most studies. “Passivation” is an over-used word in most research where people introduce some materials to the PSCs and show it helps to improve V_{OC} and attribute the result to “defect passivation”. In other words, most studies are methodologies and only a few reports go to the heart of the mechanism. We believe that understanding how perovskites or device interfaces evolve and what is exactly going on from a physical-chemical point of view is more essential than doing the same thing over and again in different PSCs.

Acknowledgment

Our studies discussed in this review were financially supported by the Japanese Society for Promotion of Science (JSPS) with Grant-in-Aid for Scientific Research (No. 20K15385, No. 19H05636).

Conflict of Interest

The authors declare no conflict of interest.

References

- | | | | |
|---------|---------------|------------|--------|
| 1. Best | Research-Cell | Efficiency | Chart, |
|---------|---------------|------------|--------|

- [https://www.nrel.gov/pv/assets/pdfs/best-research-cell-efficiencies-rev211214.pdf\).](https://www.nrel.gov/pv/assets/pdfs/best-research-cell-efficiencies-rev211214.pdf)
2. A. Kojima, K. Teshima, Y. Shirai and T. Miyasaka, *J. Am. Chem. Soc.*, 2009, **131**, 6050-6051.
 3. J. Huang, Y. Yuan, Y. Shao and Y. Yan, *Nat. Rev. Mater.*, 2017, **2**, 17042.
 4. J. J. Yoo, G. Seo, M. R. Chua, T. G. Park, Y. Lu, F. Rotermund, Y.-K. Kim, C. S. Moon, N. J. Jeon, J.-P. Correa-Baena, V. Bulović, S. S. Shin, M. G. Bawendi and J. Seo, *Nature*, 2021, **590**, 587-593.
 5. Z. Liu, L. Krückemeier, B. Krogmeier, B. Klingebiel, J. A. Márquez, S. Levchenko, S. Öz, S. Mathur, U. Rau, T. Unold and T. Kirchartz, *ACS Energy Lett.*, 2019, **4**, 110-117.
 6. G. M. Kim, H. Sato, Y. Ohkura, A. Ishii and T. Miyasaka, *Adv. Energy Mater.*, 2022, **12**, 2102856.
 7. W. Shockley and H. J. Queisser, *J. Appl. Phys.*, 1961, **32**, 510-519.
 8. C. Case, N. Beaumont and D. Kirk, *ACS Energy Lett.*, 2019, **4**, 2760-2762.
 9. S. D. Stranks, *ACS Energy Lett.*, 2017, **2**, 1515-1525.
 10. B. Ehrler, E. Alarcón-Lladó, S. W. Tabernig, T. Veeken, E. C. Garnett and A. Polman, *ACS Energy Lett.*, 2020, **5**, 3029-3033.
 11. Z. Wang, Q. Lin, B. Wenger, M. G. Christoforo, Y.-H. Lin, M. T. Klug, M. B. Johnston, L. M. Herz and H. J. Snaith, *Nat. Energy*, 2018, **3**, 855-861.
 12. PV Education Fill Factor, <https://www.pveducation.org/pvcldrom/solar-cell-operation/fill-factor>.
 13. PV Education Open-Circuit Voltage,
<https://www.pveducation.org/pvcldrom/solar-cell-operation/open-circuit-voltage>).
 14. M. Stolterfoht, P. Caprioglio, C. M. Wolff, J. A. Márquez, J. Nordmann, S. Zhang, D. Rothhardt, U. Hörmann, Y. Amir, A. Redinger, L. Kegelmann, F. Zu, S. Albrecht, N. Koch, T. Kirchartz, M. Saliba, T. Unold and D. Neher,

- Energy Environ. Sci.*, 2019, **12**, 2778-2788.
- 15. W. Tress, M. Yavari, K. Domanski, P. Yadav, B. Niesen, J. P. Correa Baena, A. Hagfeldt and M. Graetzel, *Energy Environ. Sci.*, 2018, **11**, 151-165.
 - 16. Z. Guo, A. K. Jena, I. Takei, G. M. Kim, M. A. Kamarudin, Y. Sanehira, A. Ishii, Y. Numata, S. Hayase and T. Miyasaka, *J. Am. Chem. Soc.*, 2020, **142**, 9725-9734.
 - 17. Q. Ye, F. Ma, Y. Zhao, S. Yu, Z. Chu, P. Gao, X. Zhang and J. You, *Small*, 2020, **16**, 2005246.
 - 18. X. Jiang, F. Wang, Q. Wei, H. Li, Y. Shang, W. Zhou, C. Wang, P. Cheng, Q. Chen, L. Chen and Z. Ning, *Nat. Commun.*, 2020, **11**, 1-7.
 - 19. H. Li, Q. Wei and Z. Ning, *Appl. Phys. Lett.*, 2020, **117**, 060502.
 - 20. J. Tian, Q. Xue, Q. Yao, N. Li, C. J. Brabec and H. L. Yip, *Adv. Energy Mater.*, 2020, **10**, 2000183.
 - 21. D. Luo, R. Su, W. Zhang, Q. Gong and R. Zhu, *Nat. Rev. Mater.*, 2020, **5**, 44-60.
 - 22. J. Chen and N. G. Park, *Adv. Mater.*, 2019, **31**, 1803019.
 - 23. V. Sarritzu, N. Sestu, D. Marongiu, X. Chang, S. Masi, A. Rizzo, S. Colella, F. Quochi, M. Saba, A. Mura and G. Bongiovanni, *Sci. Rep.*, 2017, **7**, 44629.
 - 24. L. M. Pazos-Outón, T. P. Xiao and E. Yablonovitch, *J. Phys. Chem. Lett.*, 2018, **9**, 1703-1711.
 - 25. D. W. De Quilettes, S. M. Vorpahl, S. D. Stranks, H. Nagaoka, G. E. Eperon, M. E. Ziffer, H. J. Snaith and D. S. Ginger, *Science*, 2015, **348**, 683-686.
 - 26. A. D. Wright, R. L. Milot, G. E. Eperon, H. J. Snaith, M. B. Johnston and L. M. Herz, *Adv. Funct. Mater.*, 2017, **27**, 1700860.
 - 27. E. J. Juarez-Perez, R. S. Sanchez, L. Badia, G. Garcia-Belmonte, Y. S. Kang, I. Mora-Sero and J. Bisquert, *J. Phys. Chem. Lett.*, 2014, **5**, 2390-2394.

28. T. Du, J. Kim, J. Ngiam, S. Xu, P. R. F. Barnes, J. R. Durrant and M. A. McLachlan, *Adv. Funct. Mater.*, 2018, **28**, 1801808.
29. J. Fu, N. F. Jamaludin, B. Wu, M. Li, A. Solanki, Y. F. Ng, S. Mhaisalkar, C. H. A. Huan and T. C. Sum, *Adv. Energy Mater.*, 2019, **9**, 1803119.
30. C. Ran, J. Xu, W. Gao, C. Huang and S. Dou, *Chem. Soc. Rev.*, 2018, **47**, 4581-4610.
31. L. Li, Y. Chen, Z. Liu, Q. Chen, X. Wang and H. Zhou, *Adv. Mater.*, 2016, **28**, 9862-9868.
32. X. Zheng, B. Chen, J. Dai, Y. Fang, Y. Bai, Y. Lin, H. Wei, Xiao and J. Huang, *Nat. Energy*, 2017, **2**, 17102.
33. B. Chen, P. N. Rudd, S. Yang, Y. Yuan and J. Huang, *Chem. Soc. Rev.*, 2019, **48**, 3842-3867.
34. E. Aydin, M. Bastiani and S. Wolf, *Adv. Mater.*, 2019, **31**, 1900428.
35. F. Gao, Y. Zhao, X. Zhang and J. You, *Adv. Energy Mater.*, 2020, **10**, 1902650.
36. A. R. B. Mohd Yusoff, M. Vasilopoulou, D. G. Georgiadou, L. C. Palilis, A. Abate and M. K. Nazeeruddin, *Energy Environ. Sci.*, 2021, **14**, 2906-2953.
37. L. Fu, H. Li, L. Wang, R. Yin, B. Li and L. Yin, *Energy Environ. Sci.*, 2020, **13**, 4017-4056.
38. C. M. Wolff, P. Caprioglio, M. Stolterfoht and D. Neher, *Adv. Mater.*, 2019, **31**, 1902762.
39. D. Głowienka, D. Zhang, F. Di Giacomo, M. Najafi, S. Veenstra, J. Szmytkowski and Y. Galagan, *Nano Energy*, 2020, **67**, 104186.
40. T. S. Sherkar, C. Momblona, L. Gil-Escríg, J. Ávila, M. Sessolo, H. J. Bolink and L. J. A. Koster, *ACS Energy Lett.*, 2017, **2**, 1214-1222.
41. P. Caprioglio, M. Stolterfoht, C. M. Wolff, T. Unold, B. Rech, S. Albrecht and D. Neher, *Adv. Energy Mater.*, 2019, **9**, 1901631.
42. S. Wang, Y. Zhu, W. Sun, X. Miao, Z. Ma, C. Yang, B. Liu, S. Li, R. Ma and C. Wang, *Sol. Energy*, 2018, **176**, 118-125.

- Published on 20 June 2022. Downloaded on 6/30/2022 1:33:51 PM.
43. X.-K. Chen, D. Qian, Y. Wang, T. Kirchartz, W. Tress, H. Yao, J. Yuan, M. Hülsbeck, M. Zhang and Y. Zou, *Nat. Energy*, 2021, **6**, 799-806.
44. A. Krishna, H. Zhang, Z. Zhou, T. Gallet, M. Dankl, O. Ouellette, F. T. Eickemeyer, F. Fu, S. Sanchez, M. Mensi, S. M. Zakeeruddin, U. Rothlisberger, G. N. Manjunatha Reddy, A. Redinger, M. Grätzel and A. Hagfeldt, *Energy Environ. Sci.*, 2021, **14**, 5552–5562.
45. R. E. Brandt, J. R. Poindexter, P. Gorai, R. C. Kurchin, R. L. Z. Hoye, L. Nienhaus, M. W. B. Wilson, J. A. Polizzotti, R. Sereika, R. Žaltauskas, L. C. Lee, J. L. Macmanus-Driscoll, M. Bawendi, V. Stevanović and T. Buonassisi, *Chem. Mater.*, 2017, **29**, 4667-4674.
46. L. K. Ono, S. Liu and Y. Qi, *Angew. Chem. Int. Ed.*, 2020, **59**, 6676-6698.
47. W.-J. Yin, T. Shi and Y. Yan, *Appl. Phys. Lett.*, 2014, **104**, 063903.
48. W. J. Yin, T. Shi and Y. Yan, *Adv. Mater.*, 2014, **26**, 4653-4658.
49. G. Landi, H. C. Neitzert, C. Barone, C. Mauro, F. Lang, S. Albrecht, B. Rech and S. Pagano, *Adv. Sci.*, 2017, **4**, 1700183.
50. K. Frohma, M. Anaya, S. Macpherson, J. Sung, T. A. S. Doherty, Y.-H. Chiang, A. J. Winchester, K. W. P. Orr, J. E. Parker, P. D. Quinn, K. M. Dani, A. Rao and S. D. Stranks, *Nat. Nanotechnol.*, 2021, 1-7.
51. J. Xu, A. Maxwell, M. Wei, Z. Wang, B. Chen, T. Zhu and E. H. Sargent, *ACS Energy Lett.*, 2021, **6**, 4220-4227.
52. X. Zhang, M. E. Turiansky and C. G. Van de Walle, *Cell Rep. Phys. Sci.*, 2021, **2**, 100604.
53. H. Zhou, Q. Chen, G. Li, S. Luo, T.-b. Song, H.-S. Duan, Z. Hong, J. You, Y. Liu and Y. Yang, *Science*, 2014, **345**, 542-546.
54. T. Kirchartz, L. Krückemeier and E. L. Unger, *APL Mater.*, 2018, **6**, 100702.
55. H. Li, Y. Xia, C. Wang, G. Wang, Y. Chen, L. Guo, D. Luo and S. Wen, *ACS Appl. Mater. Interfaces*, 2019, **11**, 34989-34996.

56. J.-H. Im, H.-S. Kim and N.-G. Park, *APL Mater.*, 2014, **2**, 081510.
57. M. Adnan and J. K. Lee, *Sci. Rep.*, 2018, **8**, 1-10.
58. M. R. Leyden, L. K. Ono, S. R. Raga, Y. Kato, S. Wang and Y. Qi, *J. Mater. Chem. A*, 2014, **2**, 18742-18745.
59. M. Stolterfoht, C. M. Wolff, Y. Amir, A. Paulke, L. Perdigón-Toro, P. Caprioglio and D. Neher, *Energy Environ. Sci.*, 2017, **10**, 1530-1539.
60. Z. Bi, X. Rodríguez-Martínez, C. Aranda, E. Pascual-San-José, A. R. Goñi, M. Campoy-Quiles, X. Xu and A. Guerrero, *J. Mater. Chem. A*, 2018, **6**, 19085-19093.
61. J. Kang and L.-W. Wang, *J. Phys. Chem. Lett.*, 2017, **8**, 489-493.
62. Y. Numata, Y. Sanehira and T. Miyasaka, *ACS Appl. Energy Mater.*, 2021, **4**, 1069-1077.
63. A. D. Taylor, Q. Sun, K. P. Goetz, Q. An, T. Schramm, Y. Hofstetter, M. Litterst, F. Paulus and Y. Vaynzof, *Nat. Commun.*, 2021, **12**, 1-11.
64. Y. Huang, T. Liu, B. Wang, J. Li, D. Li, G. Wang, Q. Lian, A. Amini, S. Chen and C. Cheng, *Adv. Mater.*, 2021, **33**, 2102816.
65. G. Li, T. Zhang and Y. Zhao, *J. Mater. Chem. A*, 2015, **3**, 19674-19678.
66. W. Zhou, P. Zhou, X. Lei, Z. Fang, M. Zhang, Q. Liu, T. Chen, H. Zeng, L. Ding and J. Zhu, *ACS Appl. Mater. Interfaces*, 2018, **10**, 1897-1908.
67. S. Yang, Q. Han, L. Wang, Y. Zhou, F. Yu, C. Li, X. Cai, L. Gao, C. Zhang and T. Ma, *Chem. Eng. J.*, 2021, **426**, 131838.
68. Z. Guo, L. Gao, Z. Xu, S. Teo, C. Zhang, Y. Kamata, S. Hayase and T. Ma, *Small*, 2018, **14**, 1802738.
69. L. Yang, Q. Xiong, Y. Li, P. Gao, B. Xu, H. Lin, X. Li and T. Miyasaka, *J. Mater. Chem. A*, 2021, **9**, 1574-1582.
70. H. Zheng, X. Xu, S. Xu, G. Liu, S. Chen, X. Zhang, T. Chen and X. Pan, *J. Mater. Chem. C*, 2019, **7**, 4441-4448.
71. F. Liu, Q. Dong, M. K. Wong, A. B. Djurišić, A. Ng, Z. Ren, Q. Shen, C. Surya, W. K. Chan, J. Wang, A. M. C. Ng, C. Liao, H. Li, K. Shih, C. Wei,

- H. Su and J. Dai, *Adv. Energy Mater.*, 2016, **6**, 1502206.
72. Z. Ma, D. Huang, Q. Liu, G. Yan, Z. Xiao, D. Chen, J. Zhao, Y. Xiang, C. Peng, H. Li, M. Zhang, W. Zhang, L. Duan and Y. Huang, *J. Energy Chem.*, 2022, **66**, 152-160.
73. D. Zhang, H. Zhang, H. Guo, F. Ye, S. Liu and Y. Wu, *Adv. Funct. Mater.*, 2022, 2200174.
74. G. M. Kim, A. Ishii, S. Öz and T. Miyasaka, *Adv. Energy Mater.*, 2020, **10**, 1903299.
75. K. Liao, J.-a. Yang, C. Li, T. Li and F. Hao, *ACS Appl. Mater. Interfaces*, 2019, **11**, 39882-39889.
76. K. Odysseas Kosmatos, L. Theofylaktos, E. Giannakaki, D. Deligiannis, M. Konstantakou and T. Stergiopoulos, *Energy Environ. Sci.*, 2019, **2**, 79-92.
77. M. Kim, G.-H. Kim, T. K. Lee, I. W. Choi, H. W. Choi, Y. Jo, Y. J. Yoon, J. W. Kim, J. Lee, D. Huh, H. Lee, S. K. Kwak, J. Y. Kim and D. S. Kim, *Joule*, 2019, **3**, 2179-2192.
78. J. J. Yoo, G. Seo, M. R. Chua, T. G. Park, Y. Lu, F. Rotermund, Y.-K. Kim, C. S. Moon, N. J. Jeon and J.-P. Correa-Baena, *Nature*, 2021, **590**, 587-593.
79. H. Zhu, L. Pan, F. T. Eickemeyer, M. A. Hope, O. Ouellette, A. Q. M. Alanazi, J. Gao, T. P. Baumeler, X. Li, S. Wang, S. M. Zakeeruddin, Y. Liu, L. Emsley and M. Grätzel, *ACS Energy Lett.*, 2022, **7**, 1112-1119.
80. C.-G. Wu, C.-H. Chiang and S. H. Chang, *Nanoscale*, 2016, **8**, 4077-4085.
81. Y. Liang, Y. Wang, C. Mu, S. Wang, X. Wang, D. Xu and L. Sun, *Adv. Energy Mater.*, 2018, **8**, 1701159.
82. I. S. Yang and N. G. Park, *Adv. Funct. Mater.*, 2021, **31**, 2100396.
83. B.-w. Park, H. W. Kwon, Y. Lee, M. G. Kim, G. Kim, K.-j. Kim, Y. K. Kim, J. Im, T. J. Shin and S. I. Seok, *Nat. Energy*, 2021, **6**, 419-428.
84. G. KIM, E. S. Oh, A. K. Jena and T. Miyasaka, *J. Mater. Chem. A*, 2021,

- 9, 26248-26255.
85. F. Zhang, Q. Huang, J. Song, S. Hayase, J. Qu and Q. Shen, *Sol. RRL*, 2020, **4**, 2000149.
86. Y. Numata, A. Kogo, Y. Udagawa, H. Kunugita, K. Ema, Y. Sanehira and T. Miyasaka, *ACS Appl. Mater. Interfaces*, 2017, **9**, 18739-18747.
87. N. D. Pham, V. T. Tiong, D. Yao, W. Martens, A. Guerrero, J. Bisquert and H. Wang, *Nano Energy*, 2017, **41**, 476-487.
88. M. A. Mahmud, N. K. Elumalai, M. B. Upama, D. Wang, B. Puthen-Veettil, F. Haque, M. Wright, C. Xu, A. Pivrikas and A. Uddin, *Sol. Energy Mater. Sol. Cells*, 2017, **167**, 87-101.
89. W. Zhu, C. Bao, Y. Wang, F. Li, X. Zhou, J. Yang, B. Lv, X. Wang, T. Yu and Z. Zou, *Dalton Trans.*, 2016, **45**, 7856-7865.
90. Y. Yang, J. Wu, X. Wang, Q. Guo, X. Liu, W. Sun, Y. Wei, Y. Huang, Z. Lan, M. Huang, J. Lin, H. Chen and Z. Wei, *Adv. Mater.*, 2020, **32**, 1904347.
91. R. D. Chavan, N. Parikh, M. M. Tavakoli, D. Prochowicz, A. Kalam, P. Yadav, P. H. Bhoite and C. K. Hong, *Adv. Mater. Interfaces*, 2021, **8**, 2100177.
92. C. Aranda, A. Guerrero and J. Bisquert, *ACS Energy Lett.*, 2019, **4**, 741-746.
93. A. O. Alvarez, R. Arcas, C. A. Aranda, L. Bethencourt, E. Mas-Marzá, M. Saliba and F. Fabregat-Santiago, *J. Phys. Chem. Lett.*, 2020, **11**, 8417-8423.
94. W. Ke, G. Fang, J. Wang, P. Qin, H. Tao, H. Lei, Q. Liu, X. Dai and X. Zhao, *ACS Appl. Mater. Interfaces*, 2014, **6**, 15959-15965.
95. Y. Sanehira, N. Shibayama, Y. Numata, M. Ikegami and T. Miyasaka, *ACS Appl. Mater. Interfaces*, 2020, **12**, 15175-15182.
96. T. Singh, S. Öz, A. Sasinska, R. Frohnoven, S. Mathur and T. Miyasaka, *Adv. Funct. Mater.*, 2018, **28**, 1706287.

97. Z. Guo, L. Gao, C. Zhang, Z. Xu and T. Ma, *J. Mater. Chem. A*, 2018, **6**, 4572-4589.
98. Q. Jiang, X. Zhang and J. You, *Small*, 2018, **14**, 1801154.
99. J. Zhuang, P. Mao, Y. Luan, N. Chen, X. Cao, G. Niu, F. Jia, F. Wang, S. Cao and J. Wang, *Adv. Funct. Mater.*, 2021, **31**, 2010385.
100. P. Wang, R. Li, B. Chen, F. Hou, J. Zhang, Y. Zhao and X. Zhang, *Adv. Mater.*, 2020, **32**, 1905766.
101. C. Wang, J. Wu, X. Liu, S. Wang, Z. Yan, L. Chen, G. Li, X. Zhang, W. Sun and Z. Lan, *J. Alloys Compd.*, 2021, **886**, 161352.
102. J. Zhang, R. Li, S. Apergi, P. Wang, B. Shi, J. Jiang, N. Ren, W. Han, Q. Huang and G. Brocks, *Sol. RRL*, 2021, **5**, 2100464.
103. B. Cao, L. Yang, S. Jiang, H. Lin, N. Wang and X. Li, *J. Mater. Chem. A*, 2019, **7**, 4960-4970.
104. Z. Ren, K. Liu, H. Hu, X. Guo, Y. Gao, P. W. Fong, Q. Liang, H. Tang, J. Huang and H. Zhang, *Light Sci. Appl.*, 2021, **10**, 1-15.
105. G. Yang, H. Tao, P. Qin, W. Ke and G. Fang, *J. Mater. Chem. A*, 2016, **4**, 3970-3990.
106. J. Zhang, W. Mao, X. Hou, J. Duan, J. Zhou, S. Huang, W. Ou-Yang, X. Zhang, Z. Sun and X. Chen, *Sol. Energy*, 2018, **174**, 1133-1141.
107. W. J. Scheideler, N. Rolston, O. Zhao, J. Zhang and R. H. Dauskardt, *Adv. Energy Mater.*, 2019, **9**, 1803600.
108. T. Wang, D. Ding, H. Zheng, X. Wang, J. Wang, H. Liu and W. Shen, *Sol. RRL*, 2019, **3**, 1900045.
109. T. H. Schloemer, J. A. Christians, J. M. Luther and A. Sellinger, *Chem. Sci.*, 2019, **10**, 1904-1935.
110. X. Niu, N. Li, C. Zhu, L. Liu, Y. Zhao, Y. Ge, Y. Chen, Z. Xu, Y. Lu and M. Sui, *J. Mater. Chem. A*, 2019, **7**, 7338-7346.
111. X. Wen, J. Wu, M. Ye, D. Gao and C. Lin, *Chem. Commun.*, 2016, **52**, 11355-11358.

112. N. J. Jeon, H. Na, E. H. Jung, T.-Y. Yang, Y. G. Lee, G. Kim, H.-W. Shin, S. I. Seok, J. Lee and J. Seo, *Nat. Energy*, 2018, **3**, 682-689.
113. M. Jeong, I. W. Choi, E. M. Go, Y. Cho, M. Kim, B. Lee, S. Jeong, Y. Jo, H. W. Choi, J. Lee, J.-H. Bae, S. K. Kwak, D. S. Kim and C. Yang, *Science*, 2020, **369**, 1615-1620.
114. J. Y. Seo, S. Akin, M. Zalibera, M. A. R. Preciado, H. S. Kim, S. M. Zakeeruddin, J. V. Milić and M. Grätzel, *Adv. Funct. Mater.*, 2021, **31**, 2102124.
115. N. D. Pham, J. Shang, Y. Yang, M. T. Hoang, V. T. Tiong, X. Wang, L. Fan, P. Chen, L. Kou and L. Wang, *Nano Energy*, 2020, **69**, 104412.
116. M. Hu, X. Wu, W. L. Tan, B. Tan, A. D. Scully, L. Ding, C. Zhou, Y. Xiong, F. Huang and A. N. Simonov, *ACS Appl. Mater. Interfaces*, 2020, **12**, 8260-8270.
117. H. Nishimura, I. Okada, T. Tanabe, T. Nakamura, R. Murdey and A. Wakamiya, *ACS Appl. Mater. Interfaces*, 2020, **12**, 32994-33003.
118. Q. Jiang, Y. Zhao, X. Zhang, X. Yang, Y. Chen, Z. Chu, Q. Ye, X. Li, Z. Yin and J. You, *Nat. Photon.*, 2019, **13**, 460-466.
119. H. Uratani and K. Yamashita, *J. Phys. Chem. Lett.*, 2017, **8**, 742-746.
120. W. Peng, B. Anand, L. Liu, S. Sampat, B. E. Bearden, A. V. Malko and Y. J. Chabal, *Nanoscale*, 2016, **8**, 1627-1634.
121. Y. Liu, K. Palotas, X. Yuan, T. Hou, H. Lin, Y. Li and S.-T. Lee, *ACS Nano*, 2017, **11**, 2060-2065.
122. G. Han, T. M. Koh, S. S. Lim, T. W. Goh, X. Guo, S. W. Leow, R. Begum, T. C. Sum, N. Mathews and S. Mhaisalkar, *ACS Appl. Mater. Interfaces*, 2017, **9**, 21292-21297.
123. J. Ding, Z. Lian, Y. Li, S. Wang and Q. Yan, *J. Phys. Chem. Lett.*, 2018, **9**, 4221-4226.
124. H. Kanda, N. Shibayama, A. J. Huckaba, Y. Lee, S. Paek, N. Klipfel, C. Roldán-Carmona, V. I. E. Queloz, G. Grancini, Y. Zhang, M. Abuhelaiqa,

- K. T. Cho, M. Li, M. D. Mensi, S. Kinge and M. K. Nazeeruddin, *Energy Environ. Sci.*, 2020, **13**, 1222-1230.
125. H. Kanda, N. Shibayama, M. Abuhelaiqa, S. Paek, R. Kaneko, N. Klipfel, A. A. Sutanto, C. R. Carmona, A. J. Huckaba, H. Kim, C. Momblona, A. M. Asiri and M. K. Nazeeruddin, *J. Mater. Chem. A*, 2020, **8**, 17113-17119.
126. L. Zeng, Z. Chen, S. Qiu, J. Hu, C. Li, X. Liu, G. Liang, C. J. Brabec, Y. Mai and F. Guo, *Nano Energy*, 2019, **66**, 104099.
127. C. Zervos, M. Tountas, K. Chatzimanolis, C. Polyzoidis and E. Kymakis, *J. Mater. Chem. C*, 2020, **8**, 7143-7148.
128. S. Wu, Z. Li, J. Zhang, X. Wu, X. Deng, Y. Liu, J. Zhou, C. Zhi, X. Yu, W. C. H. Choy, Z. Zhu and A. K. Y. Jen, *Adv. Mater.*, 2021, **33**, 2105539.
129. W. S. Yang, B.-W. Park, E. H. Jung, N. J. Jeon, Y. C. Kim, D. U. Lee, S. S. Shin, J. Seo, E. K. Kim and J. H. Noh, *Science*, 2017, **356**, 1376-1379.
130. J. Luo, F. Lin, J. Xia, H. Yang, R. Zhang, H. A. Malik, H. Shu, Z. Wan, K. Han, R. Wang, X. Yao and C. Jia, *Nano Energy*, 2021, **82**, 105751.
131. S. Wu, J. Zhang, Z. Li, D. Liu, M. Qin, S. H. Cheung, X. Lu, D. Lei, S. K. So, Z. Zhu and A. K. Y. Jen, *Joule*, 2020, **4**, 1248-1262.
132. Q. Wang, C. Bi and J. Huang, *Nano Energy*, 2015, **15**, 275-280.
133. M. Degani, Q. An, M. Albaladejo-Siguan, Y. J. Hofstetter, C. Cho, F. Paulus, G. Grancini and Y. Vaynzof, *Sci. Adv.*, 2021, **7**, eabj7930.
134. S. Song, E. Y. Park, B. S. Ma, D. J. Kim, H. H. Park, Y. Y. Kim, S. S. Shin, N. J. Jeon, T. S. Kim and J. Seo, *Adv. Energy Mater.*, 2021, **11**, 2003382.
135. H. Liu, H.-R. Liu, F. Yang, J.-E. Yang, J. Song, M. Li, Z. Li, W. C. Tsoi, M. Chinweokwu Eze, Z.-Y. Liu, H. Ma, M. Gao and Z.-K. Wang, *J. Power Sources*, 2020, **448**, 227420.
136. A. Al-Ashouri, A. Magomedov, M. Roß, M. Jošt, M. Talaikis, G. Chistiakova, T. Bertram, J. A. Márquez, E. Köhnen, E. Kasparavičius, S. Levencenco, L. Gil-Escríg, C. J. Hages, R. Schlatmann, B. Rech, T. Malinauskas, T. Unold,

- C. A. Kaufmann, L. Korte, G. Niaura, V. Getautis and S. Albrecht, *Energy Environ. Sci.*, 2019, **12**, 3356-3369.
137. G. Kapil, T. Bessho, Y. Sanehira, S. R. Sahamir, M. Chen, A. K. Baranwal, D. Liu, Y. Sono, D. Hirotani, D. Nomura, K. Nishimura, M. A. Kamarudin, Q. Shen, H. Segawa and S. Hayase, *ACS Energy Lett.*, 2022, **7**, 966-974.
138. A. K. Jena, M. Ikegami and T. Miyasaka, *ACS Energy Lett.*, 2017, **2**, 1760-1761.
139. X. Hu, X.-F. Jiang, X. Xing, L. Nian, X. Liu, R. Huang, K. Wang, H.-L. Yip and G. Zhou, *Sol. RRL*, 2018, **2**, 1800083.
140. N.-K. Kim, Y. H. Min, S. Noh, E. Cho, G. Jeong, M. Joo, S.-W. Ahn, J. S. Lee, S. Kim, K. Ihm, H. Ahn, Y. Kang, H.-S. Lee and D. Kim, *Sci. Rep.*, 2017, **7**, 1-9.
141. E. Smecca, Y. Numata, I. Deretzis, G. Pellegrino, S. Boninelli, T. Miyasaka, A. La Magna and A. Alberti, *Phys. Chem. Chem. Phys.*, 2016, **18**, 13413-13422.
142. B. Conings, J. Drijkoningen, N. Gauquelin, A. Babayigit, J. D'Haen, L. D'Olieslaeger, A. Ethirajan, J. Verbeeck, J. Manca and E. Mosconi, *Adv. Energy Mater.*, 2015, **5**, 1500477.
143. G. Zhou, J. Wu, Y. Zhao, Y. Li, J. Shi, Y. Li, H. Wu, D. Li, Y. Luo and Q. Meng, *ACS Appl. Mater. Interfaces*, 2018, **10**, 9503-9513.
144. T. Miyasaka, A. Kulkarni, G. M. Kim, S. Öz and A. K. Jena, *Adv. Energy Mater.*, 2020, **10**, 1902500.
145. G. E. Eperon, G. M. Paternò, R. J. Sutton, A. Zampetti, A. A. Haghimirad, F. Cacialli and H. J. Snaith, *J. Mater. Chem. A*, 2015, **3**, 19688-19695.
146. S. M. Yoon, H. Min, J. B. Kim, G. Kim, K. S. Lee and S. I. Seok, *Joule*, 2021, **5**, 183-196.
147. B. Yu, J. Shi, S. Tan, Y. Cui, W. Zhao, H. Wu, Y. Luo, D. Li and Q. Meng, *Angew. Chem. Int. Ed.*, 2021, **60**, 13436-13443.
148. W. Xiang, S. Liu and W. Tress, *Energy Environ. Sci.*, 2021, **14**, 2090-

- 2113.
149. W. Chen, H. Chen, G. Xu, R. Xue, S. Wang, Y. Li and Y. Li, *Joule*, 2019, **3**, 191-204.
150. W. Zhu, W. Chai, D. Chen, J. Ma, D. Chen, H. Xi, J. Zhang, C. Zhang and Y. Hao, *ACS Energy Lett.*, 2021, **6**, 1500-1510.
151. D.-J. Xue, Y. Hou, S.-C. Liu, M. Wei, B. Chen, Z. Huang, Z. Li, B. Sun, A. H. Proppe, Y. Dong, M. I. Saidaminov, S. O. Kelley, J.-S. Hu and E. H. Sargent, *Nat. Commun.*, 2020, **11**, 1-8.
152. P. Wang, X. Zhang, Y. Zhou, Q. Jiang, Q. Ye, Z. Chu, X. Li, X. Yang, Z. Yin and J. You, *Nat. Commun.*, 2018, **9**, 1-7.
153. C. Liu, W. Li, C. Zhang, Y. Ma, J. Fan and Y. Mai, *J. Am. Chem. Soc.*, 2018, **140**, 3825-3828.
154. M. H. Li, S. C. Liu, F. Z. Qiu, Z. Y. Zhang, D. J. Xue and J. S. Hu, *Adv. Energy Mater.*, 2020, **10**, 2000501.
155. Z. Guo, S. Teo, Z. Xu, C. Zhang, Y. Kamata, S. Hayase and T. Ma, *J. Mater. Chem. A*, 2019, **7**, 1227-1232.
156. Z. Guo, S. Zhao, A. Liu, Y. Kamata, S. Teo, S. Yang, Z. Xu, S. Hayase and T. Ma, *ACS Appl. Mater. Interfaces*, 2019, **11**, 19994-20003.
157. H. Li, X. Hao, B. Chang, Z. Li, L. Wang, L. Pan, X. Chen and L. Yin, *ACS Appl. Mater. Interfaces*, 2021, **13**, 40489-40501.
158. X. Wang, X. Ran, X. Liu, H. Gu, S. Zuo, W. Hui, H. Lu, B. Sun, X. Gao, J. Zhang, Y. Xia, Y. Chen and W. Huang, *Angew. Chem. Int. Ed.*, 2020, **59**, 13354-13361.
159. S. Yang, J. Wen, Z. Liu, Y. Che, J. Xu, J. Wang, D. Xu, N. Yuan, J. Ding, Y. Duan and S. Liu, *Adv. Energy Mater.*, 2021, **12**, 2103019.
160. S.-C. Liu, Z. Li, Y. Yang, X. Wang, Y.-X. Chen, D.-J. Xue and J.-S. Hu, *J. Am. Chem. Soc.*, 2019, **141**, 18075-18082.
161. H.-H. Fang, S. Adjokatse, H. Wei, J. Yang, G. R. Blake, J. Huang, J. Even and M. A. Loi, *Sci. Adv.*, 2016, **2**, e1600534.

162. M. Anaya, J. F. Galisteo-López, M. E. Calvo, J. P. Espinós and H. Míguez, *J. Phys. Chem. Lett.*, 2018, **9**, 3891-3896.
163. Y. Tian, M. Peter, E. Unger, M. Abdellah, K. Zheng, T. Pullerits, A. Yartsev, V. Sundström and I. G. Scheblykin, *Phys. Chem. Chem. Phys.*, 2015, **17**, 24978-24987.
164. N. Aristidou, I. Sanchez-Molina, T. Chotchuangchutchaval, M. Brown, L. Martinez, T. Rath and S. A. Haque, *Angew. Chem. Int. Ed.*, 2015, **54**, 8208-8212.
165. N. Aristidou, C. Eames, I. Sanchez-Molina, X. Bu, J. Kosco, M. S. Islam and S. A. Haque, *Nat. Commun.*, 2017, **8**, 15218.
166. K. Wang, C. Gao, Z. Xu, Q. Tian, X. Gu, L. Zhang, S. Zhang, K. Zhao and S. Liu, *Adv. Funct. Mater.*, 2021, **31**, 2101568.
167. S. Öz, A. K. Jena, A. Kulkarni, K. Mouri, T. Yokoyama, I. Takei, F. Ünlü, S. Mathur and T. Miyasaka, *ACS Energy Lett.*, 2020, **5**, 1292-1299.
168. K. Wang, W. S. Subhani, Y. Wang, X. Zuo, H. Wang, L. Duan and S. Liu, *Adv. Mater.*, 2019, **31**, 1902037.
169. A. Swarnkar, W. J. Mir and A. Nag, *ACS Energy Lett.*, 2018, **3**, 286-289.
170. J. Liang, P. Zhao, C. Wang, Y. Wang, Y. Hu, G. Zhu, L. Ma, J. Liu and Z. Jin, *J. Am. Chem. Soc.*, 2017, **139**, 14009-14012.
171. F. Yang, D. Hirotani, G. Kapil, M. A. Kamarudin, C. H. Ng, Y. Zhang, Q. Shen and S. Hayase, *Angew. Chem.*, 2018, **130**, 12927-12931.
172. M. Chen, M.-G. Ju, H. F. Garces, A. D. Carl, L. K. Ono, Z. Hawash, Y. Zhang, T. Shen, Y. Qi, R. L. Grimm, D. Pacifici, X. C. Zeng, Y. Zhou and N. P. Padture, *Nat. Commun.*, 2019, **10**, 1-8.
173. A. K. Jena, A. Kulkarni, Y. Sanehira, M. Ikegami and T. Miyasaka, *Chem. Mater.*, 2018, **30**, 6668-6674.
174. J. Liang, Z. Liu, L. Qiu, Z. Hawash, L. Meng, Z. Wu, Y. Jiang, L. K. Ono and Y. Qi, *Adv. Energy Mater.*, 2018, **8**, 1800504.
175. Z. Yao, W. Zhao, S. Chen, Z. Jin and S. F. Liu, *ACS Appl. Energy Mater.*,

- 2020, **3**, 5190-5197.
176. C. F. J. Lau, M. Zhang, X. Deng, J. Zheng, J. Bing, Q. Ma, J. Kim, L. Hu, M. A. Green, S. Huang and A. Ho-Baillie, *ACS Energy Lett.*, 2017, **2**, 2319-2325.
177. K. Zhang, W. Li, J. Yu and X. Han, *Sol. Energy*, 2021, **222**, 186-192.
178. S. Kajal, G.-H. Kim, C. W. Myung, Y. S. Shin, J. Kim, J. Jeong, A. Jana, J. Y. Kim and K. S. Kim, *J. Mater. Chem. A*, 2019, **7**, 21740-21746.
179. T. Ozturk, E. Akman, A. E. Shalan and S. Akin, *Nano Energy*, 2021, 106157.
180. Y. Long, C. Wang, X. Liu, J. Wang, S. Fu, J. Zhang, Z. Hu and Y. Zhu, *J. Mater. Chem. C*, 2021, **9**, 2145-2155.
181. W. Xiang, Z. Wang, D. J. Kubicki, W. Tress, J. Luo, D. Prochowicz, S. Akin, L. Emsley, J. Zhou, G. Dietler, M. Grätzel and A. Hagfeldt, *Joule*, 2019, **3**, 205-214.
182. E. T. Hoke, D. J. Slotcavage, E. R. Dohner, A. R. Bowring, H. I. Karunadasa and M. D. McGehee, *Chem. Sci.*, 2015, **6**, 613-617.
183. L. A. Frolova, S. Y. Luchkin, Y. Lekina, L. G. Gutsev, S. A. Tsarev, I. S. Zhidkov, E. Z. Kurmaev, Z. X. Shen, K. J. Stevenson and S. M. Aldoshin, *Adv. Energy Mater.*, 2021, **11**, 2002934.
184. Y. Hu, F. Bai, X. Liu, Q. Ji, X. Miao, T. Qiu and S. Zhang, *ACS Energy Lett.*, 2017, **2**, 2219-2227.
185. C. Yang, Q. Han, S. Liu, J. Liao, C. Long, Y. Li, G. Dai, J. Yang and X. Liu, *J. Phys. Chem. Lett.*, 2021, **12**, 6927-6933.
186. S. Xiang, W. Li, Y. Wei, J. Liu, H. Liu, L. Zhu and H. Chen, *Nanoscale*, 2018, **10**, 9996-10004.
187. C. Liu, W. Li, H. Li, H. Wang, C. Zhang, Y. Yang, X. Gao, Q. Xue, H.-L. Yip, J. Fan, R. E. I. Schropp and Y. Mai, *Adv. Energy Mater.*, 2019, **9**, 1803572.
188. Z. Wang, A. K. Baranwal, M. A. Kamarudin, Y. Kamata, C. H. Ng, M.

- Pandey, T. Ma and S. Hayase, *J. Mater. Chem. A*, 2019, **7**, 20390-20397.
189. J. Duan, Y. Zhao, X. Yang, Y. Wang, B. He and Q. Tang, *Adv. Energy Mater.*, 2018, **8**, 1802346.
190. A. Alberti, E. Smecca, I. Deretzis, G. Mannino, C. Bongiorno, S. Valastro, S. Sanzaro, G. Fisicaro, A. K. Jena, Y. Numata, Z. Guo, C. Spinella, T. Miyasaka and A. La Magna, *Adv. Energy Sustain. Res.*, 2021, **2**, 2100091.
191. S. Yang, H. Zhao, Y. Han, C. Duan, Z. Liu and S. Liu, *Small*, 2019, **15**, 1904387.
192. S. Kajal, J. Kim, Y. S. Shin, A. N. Singh, C. W. Myung, J. Y. Kim and K. S. Kim, *Small Methods*, 2020, **4**, 2000296.
193. J. V. Patil, S. S. Mali and C. K. Hong, *ACS Appl. Mater. Interfaces*, 2020, **12**, 27176-27183.
194. Y. Li, J. Duan, H. Yuan, Y. Zhao, B. He and Q. Tang, *Sol. RRL*, 2018, **2**, 1800164.
195. D.-Y. Son, S.-G. Kim, J.-Y. Seo, S.-H. Lee, H. Shin, D. Lee and N.-G. Park, *J. Am. Chem. Soc.*, 2018, **140**, 1358-1364.
196. J. V. Patil, S. S. Mali and C. K. Hong, *Sol. RRL*, 2020, **4**, 2000164.
197. Y. Wang, T. Zhang, M. Kan, Y. Li, T. Wang and Y. Zhao, *Joule*, 2018, **2**, 2065-2075.
198. M. Tai, Y. Zhou, X. Yin, J. Han, Q. Zhang, Y. Zhou and H. Lin, *J. Mater. Chem. A*, 2019, **7**, 22675-22682.
199. Z. Li, X. Liu, J. Xu, S. Yang, H. Zhao, H. Huang, S. F. Liu and J. Yao, *J. Phys. Chem. Lett.*, 2020, **11**, 4138-4146.
200. S. Yang, W. Liu, Y. Han, Z. Liu, W. Zhao, C. Duan, Y. Che, H. Gu, Y. Li and S. Liu, *Adv. Energy Mater.*, 2020, **10**, 2002882.
201. J. Zhang, D. Bai, Z. Jin, H. Bian, K. Wang, J. Sun, Q. Wang and S. F. Liu, *Adv. Energy Mater.*, 2018, **8**, 1703246.
202. H. Tsai, W. Nie, J.-C. Blancon, C. C. Stoumpos, R. Asadpour, B. Harutyunyan, A. J. Neukirch, R. Verduzco, J. J. Crochet, S. Tretiak, L.

- Pedesseau, J. Even, M. A. Alam, G. Gupta, J. Lou, P. M. Ajayan, M. J. Bedzyk, M. G. Kanatzidis and A. D. Mohite, *Nature*, 2016, **536**, 312-316.
203. J. M. Ball and A. Petrozza, *Nat. Energy*, 2016, **1**, 16149.
204. S. Mahesh, J. M. Ball, R. D. J. Oliver, D. P. McMeekin, P. K. Nayak, M. B. Johnston and H. J. Snaith, *Energy Environ. Sci.*, 2020, **13**, 258-267.
205. T. Leijtens, G. E. Eperon, A. J. Barker, G. Grancini, W. Zhang, J. M. Ball, A. R. S. Kandada, H. J. Snaith and A. Petrozza, *Energy Environ. Sci.*, 2016, **9**, 3472-3481.
206. D. Bi, C. Yi, J. Luo, J.-D. Décoppet, F. Zhang, Shaik, X. Li, A. Hagfeldt and M. Grätzel, *Nat. Energy*, 2016, **1**, 16142.
207. F. Yu, Q. Han, L. Wang, S. Yang, X. Cai, C. Zhang and T. Ma, *Sol. RRL*, 2021, **5**, 2100404.
208. J. He, J. Liu, Y. Hou, Y. Wang, S. Yang and H. G. Yang, *Nat. Commun.*, 2020, **11**, 1-8.
209. X. Gu, W. Xiang, Q. Tian and S. Liu, *Angew. Chem.*, 2021, **133**, 23348-23354.
210. J. Wang, J. Zhang, Y. Zhou, H. Liu, Q. Xue, X. Li, C.-C. Chueh, H.-L. Yip, Z. Zhu and A. K. Y. Jen, *Nat. Commun.*, 2020, **11**, 1-9.
211. Z. Wang, A. K. Baranwal, M. Akmal Kamarudin, P. Zhang, G. Kapil, T. Ma and S. Hayase, *Nano Energy*, 2019, **66**, 104180.
212. Y. X. Luo, F. M. Xie, J. D. Chen, H. Ren, J. K. Wang, X. Y. Cai, K. C. Shen, L. Y. Lu, Y. Q. Li, Y. N. Luponosov and J. X. Tang, *Adv. Funct. Mater.*, 2021, **31**, 2103316.
213. M.-H. Li, H.-H. Yeh, Y.-H. Chiang, U. S. Jeng, C.-J. Su, H.-W. Shiu, Y.-J. Hsu, N. Kosugi, T. Ohigashi, Y.-A. Chen, P.-S. Shen, P. Chen and T.-F. Guo, *Adv. Mater.*, 2018, **30**, 1801401.
214. S.-C. Chen, D. Wang and Q. Zheng, *Sol. RRL*, 2020, **4**, 2000321.
215. S.-C. Chen, S. Zhang and Q. Zheng, *Sci. China Mater.*, 2020, **63**, 719-727.

216. Y. Wang, M. I. Dar, L. K. Ono, T. Zhang, M. Kan, Y. Li, L. Zhang, X. Wang, Y. Yang and X. Gao, *Science*, 2019, **365**, 591-595.
217. Y. Wang, T. Zhang, M. Kan and Y. Zhao, *J. Am. Chem. Soc.*, 2018, **140**, 12345-12348.
218. J. Ma, Z. Lin, X. Guo, L. Zhou, J. He, Z. Yang, J. Zhang, Y. Hao, S. Liu and J. Chang, *J. Energy Chem.*, 2021, **63**, 558-565.
219. Y. Wang, X. Liu, T. Zhang, X. Wang, M. Kan, J. Shi and Y. Zhao, *Angew. Chem. Int. Ed.*, 2019, **58**, 16691-16696.
220. Q. Ye, Y. Zhao, S. Mu, F. Ma, F. Gao, Z. Chu, Z. Yin, P. Gao, X. Zhang and J. You, *Adv. Mater.*, 2019, **31**, 1905143.
221. Q. Zhou, J. Duan, X. Yang, Y. Duan and Q. Tang, *Angew. Chem.*, 2020, **132**, 22181-22185.
222. W. Meng, Y. Hou, A. Karl, E. Gu, X. Tang, A. Osvet, K. Zhang, Y. Zhao, X. Du, J. Garcia Cerrillo, N. Li and C. J. Brabec, *ACS Energy Lett.*, 2020, **5**, 271-279.
223. L. Zhou, X. Guo, Z. Lin, J. Ma, J. Su, Z. Hu, C. Zhang, S. Liu, J. Chang and Y. Hao, *Nano Energy*, 2019, **60**, 583-590.
224. Y. Rong, Y. Hu, S. Ravishankar, H. Liu, X. Hou, Y. Sheng, A. Mei, Q. Wang, D. Li, M. Xu, J. Bisquert and H. Han, *Energy Environ. Sci.*, 2017, **10**, 2383-2391.
225. X. Chang, J. Fang, Y. Fan, T. Luo, H. Su, Y. Zhang, J. Lu, L. Tsetseris, T. D. Anthopoulos and S. Liu, *Adv. Mater.*, 2020, **32**, 2001243.
226. S. Yang, Z. Guo, L. Gao, F. Yu, C. Zhang, M. Fan, G. Wei and T. Ma, *Sol. RRL*, 2019, **3**, 1900212.
227. S. Yang, L. Wang, L. Gao, J. Cao, Q. Han, F. Yu, Y. Kamata, C. Zhang, M. Fan, G. Wei and T. Ma, *ACS Appl. Mater. Interfaces*, 2020, **12**, 13931-13940.
228. K. Jiang, J. Wang, F. Wu, Q. Xue, Q. Yao, J. Zhang, Y. Chen, G. Zhang, Z. Zhu, H. Yan, L. Zhu and H. L. Yip, *Adv. Mater.*, 2020, **32**, 1908011.

229. S. S. Mali, J. V. Patil, P. S. Shinde, G. de Miguel and C. K. Hong, *Matter*, 2020, 1-19.
230. Q. Wang, F. Zu, P. Caprioglio, C. M. Wolff, M. Stolterfoht, M. Li, S.-H. Turren-Cruz, N. Koch, D. Neher and A. Abate, *ACS Energy Lett.*, 2020, **5**, 2343-2348.
231. L. Yan, Q. Xue, M. Liu, Z. Zhu, J. Tian, Z. Li, Z. Chen, Z. Chen, H. Yan, H.-L. Yip and Y. Cao, *Adv. Mater.*, 2018, **30**, 1802509.
232. Z. Li, R. Wang, J. Xue, X. Xing, C. Yu, T. Huang, J. Chu, K.-L. Wang, C. Dong, Z. Wei, Y. Zhao, Z.-K. Wang and Y. Yang, *J. Am. Chem. Soc.*, 2019, **141**, 17610-17616.
233. Y. Sun, J. H. Seo, C. J. Takacs, J. Seifter and A. J. Heeger, *Adv. Mater.*, 2011, **23**, 1679-1683.
234. K. Schutt, P. K. Nayak, A. J. Ramadan, B. Wenger, Y. H. Lin and H. J. Snaith, *Adv. Funct. Mater.*, 2019, **29**, 1900466.
235. R. Azmi, S. Hwang, W. Yin, T.-W. Kim, T. K. Ahn and S.-Y. Jang, *ACS Energy Lett.*, 2018, **3**, 1241-1246.
236. P. Wang, H. Wang, Y. Mao, H. Zhang, F. Ye, D. Liu and T. Wang, *Adv. Sci.*, 2020, **7**, 2000421.
237. E. C. Shen, J. D. Chen, Y. Tian, Y. X. Luo, Y. Shen, Q. Sun, T. Y. Jin, G. Z. Shi, Y. Q. Li and J. X. Tang, *Adv. Sci.*, 2020, **7**, 1901952.
238. B. Chen, M. Yang, S. Priya and K. Zhu, *J. Phys. Chem. Lett.*, 2016, **7**, 905-917.
239. S. Liu, W. Chen, Y. Shen, S. Wang, M. Zhang, Y. Li and Y. Li, *J. Mater. Chem. A*, 2020, **8**, 14555-14565.
240. Y. Han, H. Zhao, C. Duan, S. Yang, Z. Yang, Z. Liu and S. Liu, *Adv. Funct. Mater.*, 2020, **30**, 1909972.
241. Q. Xiao, J. Tian, Q. Xue, J. Wang, B. Xiong, M. Han, Z. Li, Z. Zhu, H. L. Yip and Z. A. Li, *Angew. Chem. Int. Ed.*, 2019, **58**, 17724-17730.
242. M.-H. Li, J.-Y. Shao, Y. Jiang, F.-Z. Qiu, S. Wang, J. Zhang, G. Han, J.

- Tang, F. Wang, Z. Wei, Y. Yi, Y.-W. Zhong and J.-S. Hu, *Angew. Chem. Int. Ed.*, 2021, **133**, 16524-16529.
243. N. K. Elumalai and A. Uddin, *Sol. Energy Mater. Sol. Cells*, 2016, **157**, 476-509.
244. Z. Guo, A. K. Jena, I. Takei, M. Ikegami, A. Ishii, Y. Numata, N. Shibayama and T. Miyasaka, *Adv. Funct. Mater.*, 2021, **31**, 2103614.
245. Y. Wu, H. Shen, D. Walter, D. Jacobs, T. Duong, J. Peng, L. Jiang, Y. B. Cheng and K. Weber, *Adv. Funct. Mater.*, 2016, **26**, 6807-6813.
246. B. Chen, M. Yang, S. Priya and K. Zhu, *J. Phys. Chem. Lett.*, 2016, **7**, 905-917.
247. P. Wang, H. Wang, M. Jeong, S. M. Lee, B. Du, Y. Mao, F. Ye, H. Zhang, D. Li, D. Liu, C. Yang and T. Wang, *J. Mater. Chem. C*, 2020, **8**, 8507-8514.
248. X. Li, W. Chen, S. Wang, G. Xu, S. Liu, Y. Li and Y. Li, *Adv. Funct. Mater.*, 2021, **31**, 2010696.
249. S. S. Mali, J. V. Patil, J. A. Steele, S. R. Rondiya, N. Y. Dzade and C. K. Hong, *ACS Energy Lett.*, 2021, **6**, 778-788.
250. J. Yuan, X. Ling, D. Yang, F. Li, S. Zhou, J. Shi, Y. Qian, J. Hu, Y. Sun, Y. Yang, X. Gao, S. Duhm, Q. Zhang and W. Ma, *Joule*, 2018, **2**, 2450-2463.
251. Q. Tang, J. Duan, Y. Zhao, Y. Wang and X. Yang, *Angew. Chem.*, 2019, **58**, 16147-16151.
252. Z. Yang, Z. Yu, H. Wei, X. Xiao, Z. Ni, B. Chen, Y. Deng, S. N. Haberreutinger, X. Chen, K. Wang, J. Zhao, P. N. Rudd, J. J. Berry, M. C. Beard and J. Huang, *Nat. Commun.*, 2019, **10**, 4498.
253. R. Lin, K. Xiao, Z. Qin, Q. Han, C. Zhang, M. Wei, M. I. Saidaminov, Y. Gao, J. Xu, M. Xiao, A. Li, J. Zhu, E. H. Sargent and H. Tan, *Nat. Energy*, 2019, **4**, 864-873.
254. J. Wang, L. Chen, Z. Qian, G. Ren, J. Wu and H. Zhang, *J. Mater. Chem. A*, 2020, **8**, 25336-25344.

255. L. Chen, L. Wan, X. Li, W. Zhang, S. Fu, Y. Wang, S. Li, H.-Q. Wang, W. Song and J. Fang, *Chem. Mater.*, 2019, **31**, 9032-9039.
256. S. Fu, W. Zhang, X. Li, J. Guan, W. Song and J. Fang, *ACS Energy Lett.*, 2021, **6**, 3661-3668.
257. L. Liang and P. Gao, *Adv. Sci.*, 2018, **5**, 1700331.
258. F. Gu, S. Ye, Z. Zhao, H. Rao, Z. Liu, Z. Bian and C. Huang, *Sol. RRL*, 2018, **2**, 1800136.
259. F. Hao, C. C. Stoumpos, D. H. Cao, R. P. H. Chang and M. G. Kanatzidis, *Nat. Photon.*, 2014, **8**, 489-494.
260. N. K. Noel, S. D. Stranks, A. Abate, C. Wehrenfennig, S. Guarnera, A.-A. Haghimirad, A. Sadhanala, G. E. Eperon, S. K. Pathak, M. B. Johnston, A. Petrozza, L. M. Herz and H. J. Snaith, *Energy Environ. Sci.*, 2014, **7**, 3061-3068.
261. X. Jiang, H. Li, Q. Zhou, Q. Wei, M. Wei, L. Jiang, Z. Wang, Z. Peng, F. Wang, Z. Zang, K. Xu, Y. Hou, S. Teale, W. Zhou, R. Si, X. Gao, E. H. Sargent and Z. Ning, *J. Am. Chem. Soc.*, 2021, **143**, 10970-10976.
262. J. Liu, M. Ozaki, S. Yakumaru, T. Handa, R. Nishikubo, Y. Kanemitsu, A. Saeki, Y. Murata, R. Murdey and A. Wakamiya, *Angew. Chem.*, 2018, **130**, 13405-13409.
263. T. Wu, X. Liu, X. Luo, X. Lin, D. Cui, Y. Wang, H. Segawa, Y. Zhang and L. Han, *Joule*, 2021, **5**, 863-886.
264. T. Nakamura, S. Yakumaru, M. A. Truong, K. Kim, J. Liu, S. Hu, K. Otsuka, R. Hashimoto, R. Murdey, T. Sasamori, H. D. Kim, H. Ohkita, T. Handa, Y. Kanemitsu and A. Wakamiya, *Nat. Commun.*, 2020, **11**, 1-8.
265. D. Cui, X. Liu, T. Wu, X. Lin, X. Luo, Y. Wu, H. Segawa, X. Yang, Y. Zhang, Y. Wang and L. Han, *Adv. Funct. Mater.*, 2021, **31**, 2100931.
266. B. B. Yu, Z. Chen, Y. Zhu, Y. Wang, B. Han, G. Chen, X. Zhang, Z. Du and Z. He, *Adv. Mater.*, 2021, **33**, 2102055.
267. G. Li, Z. Su, M. Li, F. Yang, M. H. Aldamasy, J. Pascual, F. Yang, H. Liu,

- W. Zuo and D. D. Girolamo, *Adv. Energy Mater.*, 2021, **11**, 2101539.
268. R. Xu, H. Dong, P. Li, X. Cao, H. Li, J. Li and Z. Wu, *ACS Appl. Mater. Interfaces*, 2021, **13**, 33218-33225.
269. E. Jokar, C.-H. Chien, A. Fathi, M. Rameez, Y.-H. Chang and E. W.-G. Diau, *Energy Environ. Sci.*, 2018, **11**, 2353-2362.
270. K. Nishimura, D. Hirotani, M. A. Kamarudin, Q. Shen, T. Toyoda, S. Iikubo, T. Minemoto, K. Yoshino and S. Hayase, *ACS Appl. Mater. Interfaces*, 2019, **11**, 31105-31110.
271. K. Nishimura, M. A. Kamarudin, D. Hirotani, K. Hamada, Q. Shen, S. Iikubo, T. Minemoto, K. Yoshino and S. Hayase, *Nano Energy*, 2020, **74**, 104858.
272. M. Li, W.-W. Zuo, Y.-G. Yang, M. H. Aldamasy, Q. Wang, S. H. T. Cruz, S.-L. Feng, M. Saliba, Z.-K. Wang and A. Abate, *ACS Energy Lett.*, 2020, **5**, 1923-1929.
273. J. Sanchez-Diaz, R. S. Sánchez, S. Masi, M. Krećmarová, A. O. Alvarez, E. M. Barea, J. Rodriguez-Romero, V. S. Chirvony, J. F. Sánchez-Royo and J. P. Martinez-Pastor, *Joule*, 2022, **6**, 861–883.
274. S. Sandhu, R. Singh, K. Yoo, M. Kumar and J.-J. Lee, *J. Power Sources*, 2021, **491**, 229574.
275. Y. Liao, H. Liu, W. Zhou, D. Yang, Y. Shang, Z. Shi, B. Li, X. Jiang, L. Zhang, L. N. Quan, R. Quintero-Bermudez, B. R. Sutherland, Q. Mi, E. H. Sargent and Z. Ning, *J. Am. Chem. Soc.*, 2017, **139**, 6693-6699.
276. C. Ran, J. Xi, W. Gao, F. Yuan, T. Lei, B. Jiao, X. Hou and Z. Wu, *ACS Energy Lett.*, 2018, **3**, 713-721.
277. W.-G. Choi, C.-G. Park, Y. Kim and T. Moon, *ACS Energy Lett.*, 2020, **5**, 3461-3467.
278. X. Liu, T. Wu, J.-Y. Chen, X. Meng, X. He, T. Noda, H. Chen, X. Yang, H. Segawa, Y. Wang and L. Han, *Energy Environ. Sci.*, 2020, **13**, 2896-2902.
279. D. H. Cao, C. C. Stoumpos, T. Yokoyama, J. L. Logsdon, T.-B. Song, O.

- K. Farha, M. R. Wasielewski, J. T. Hupp and M. G. Kanatzidis, *ACS Energy Lett.*, 2017, **2**, 982-990.
280. J.-T. Lin, T.-C. Chu, D.-G. Chen, Z.-X. Huang, H.-C. Chen, C.-S. Li, C.-I. Wu, P.-T. Chou, C.-W. Chiu and H. M. Chen, *ACS Appl. Energy Mater.*, 2021, **4**, 2041-2048.
281. F. Wang, X. Jiang, H. Chen, Y. Shang, H. Liu, J. Wei, W. Zhou, H. He, W. Liu and Z. Ning, *Joule*, 2018, **2**, 2732-2743.
282. M. A. Kamarudin, D. Hirotani, Z. Wang, K. Hamada, K. Nishimura, Q. Shen, T. Toyoda, S. Iikubo, T. Minemoto, K. Yoshino and S. Hayase, *J. Phys. Chem. Lett.*, 2019, **10**, 5277-5283.
283. M. Ozaki, Y. Katsuki, J. Liu, T. Handa, R. Nishikubo, S. Yakumaru, Y. Hashikawa, Y. Murata, T. Saito, Y. Shimakawa, Y. Kanemitsu, A. Saeki and A. Wakamiya, *ACS Omega*, 2017, **2**, 7016-7021.
284. J. Pascual, M. Flatken, R. Félix, G. Li, S.-H. Turren-Cruz, M. H. Aldamasy, C. Hartmann, M. Li, D. Di Girolamo, G. Nasti, E. Hüsam, R. G. Wilks, A. Dallmann, M. Bär, A. Hoell and A. Abate, *Angew. Chem. Int. Ed.*, 2021, **60**, 21583-21591.
285. T. J. Jacobsson, J.-P. Correa-Baena, E. Halvani Anaraki, B. Philippe, S. D. Stranks, M. E. F. Bouduban, W. Tress, K. Schenk, J. Teuscher, J.-E. Moser, H. Rensmo and A. Hagfeldt, *J. Am. Chem. Soc.*, 2016, **138**, 10331-10343.
286. C. Liu, J. Tu, X. Hu, Z. Huang, X. Meng, J. Yang, X. Duan, L. Tan, Z. Li and Y. Chen, *Adv. Funct. Mater.*, 2019, **29**, 1808059.
287. E. Jokar, C.-H. Chien, C.-M. Tsai, A. Fathi and E. W.-G. Diau, *Adv. Mater.*, 2019, **31**, 1804835.
288. W. Ke, C. C. Stoumpos, M. Zhu, L. Mao, I. Spanopoulos, J. Liu, O. Y. Kontsevoi, M. Chen, D. Sarma, Y. Zhang, M. R. Wasielewski and M. G. Kanatzidis, *Sci. Adv.*, 2017, **3**, e1701293.
289. W. Ke, C. C. Stoumpos, I. Spanopoulos, L. Mao, M. Chen, M. R. Wasielewski and M. G. Kanatzidis, *J. Am. Chem. Soc.*, 2017, **139**, 14800-

- 14806.
290. W. Ke, I. Spanopoulos, Q. Tu, I. Hadar, X. Li, G. S. Shekhawat, V. P. Dravid and M. G. Kanatzidis, *J. Am. Chem. Soc.*, 2019, **141**, 8627-8637.
291. T. Wu, D. Cui, X. Liu, X. Meng, Y. Wang, T. Noda, H. Segawa, X. Yang, Y. Zhang and L. Han, *Sol. RRL*, 2020, **4**, 2000240.
292. M. Chen, Q. Dong, F. T. Eickemeyer, Y. Liu, Z. Dai, A. D. Carl, B. Bahrami, A. H. Chowdhury, R. L. Grimm, Y. Shi, Q. Qiao, S. M. Zakeeruddin, M. Grätzel and N. P. Padture, *ACS Energy Lett.*, 2020, **5**, 2223-2230.
293. Y. Chen, K. Cao, Y. Cheng, H. Shen, C. Du, Q. Wang, C. Chen, H. Cui, T. Lan, L. Liu, W. Shen and S. Chen, *Sol. RRL*, 2021, **5**, 2100068.
294. L. Ma, F. Hao, C. C. Stoumpos, B. T. Phelan, M. R. Wasielewski and M. G. Kanatzidis, *J. Am. Chem. Soc.*, 2016, **138**, 14750-14755.
295. S. Wheeler, D. Bryant, J. Troughton, T. Kirchartz, T. Watson, J. Nelson and J. R. Durrant, *J. Phys. Chem. C*, 2017, **121**, 13496-13506.
296. A. Rajagopal, Z. Yang, S. B. Jo, I. L. Braly, P. W. Liang, H. W. Hillhouse and A. K. Y. Jen, *Adv. Mater.*, 2017, **29**, 1702140.
297. Y. He, H.-Y. Chen, J. Hou and Y. Li, *J. Am. Chem. Soc.*, 2010, **132**, 1377-1382.
298. C. M. Wolff, F. Zu, A. Paulke, L. P. Toro, N. Koch and D. Neher, *Adv. Mater.*, 2017, **29**, 1700159.
299. Z. Yang, M. Zhong, Y. Liang, L. Yang, X. Liu, Q. Li, J. Zhang and D. Xu, *Adv. Funct. Mater.*, 2019, **29**, 1903621.
300. T. Yokoyama, Y. Nishitani, Y. Miyamoto, S. Kusumoto, R. Uchida, T. Matsui, K. Kawano, T. Sekiguchi and Y. Kaneko, *ACS Appl. Mater. Interfaces*, 2020, **12**, 27131-27139.
301. W. Ke, C. C. Stoumpos, J. L. Logsdon, M. R. Wasielewski, Y. Yan, G. Fang and M. G. Kanatzidis, *J. Am. Chem. Soc.*, 2016, **138**, 14998-15003.
302. K. Hamada, R. Tanaka, M. A. Kamarudin, Q. Shen, S. Iikubo, T. Minemoto, K. Yoshino, T. Toyoda, T. Ma, D.-W. Kang and S. Hayase, *ACS Appl.*

- Mater. Interfaces*, 2020, **12**, 17776-17782.
303. E. W.-G. Diau, E. Jokar and M. Rameez, *ACS Energy Lett.*, 2019, **4**, 1930-1937.
304. W. Ke, P. Priyanka, S. Vegiraju, C. C. Stoumpos, I. Spanopoulos, C. M. M. Soe, T. J. Marks, M.-C. Chen and M. G. Kanatzidis, *J. Am. Chem. Soc.*, 2018, **140**, 388-393.
305. Z. Zhao, F. Gu, Y. Li, W. Sun, S. Ye, H. Rao, Z. Liu, Z. Bian and C. Huang, *Adv. Sci.*, 2017, **4**, 1700204.
306. Y. Kang, S. Kang and S. Han, *Mater. Today Adv.*, 2019, **3**, 100019.
307. C. Wu, Q. Zhang, G. Liu, Z. Zhang, D. Wang, B. Qu, Z. Chen and L. Xiao, *Adv. Energy Mater.*, 2020, **10**, 1902496.
308. Z. Jin, Z. Zhang, J. Xiu, H. Song, T. Gatti and Z. He, *J. Mater. Chem. A*, 2020, **8**, 16166-16188.
309. D. Tiwari, D. Alibhai and D. J. Fermin, *ACS Energy Lett.*, 2018, **3**, 1882-1886.
310. R. E. Brandt, R. C. Kurchin, R. L. Z. Hoye, J. R. Poindexter, M. W. B. Wilson, S. Sulekar, F. Lenahan, P. X. T. Yen, V. Stevanović, J. C. Nino, M. G. Bawendi and T. Buonassisi, *J. Phys. Chem. Lett.*, 2015, **6**, 4297-4302.
311. C. Lan, J. Luo, S. Zhao, C. Zhang, W. Liu, S. Hayase and T. Ma, *J. Alloys Compd*, 2017, **701**, 834-840.
312. C. Lan, G. Liang, S. Zhao, H. Lan, H. Peng, D. Zhang, H. Sun, J. Luo and P. Fan, *Sol. Energy*, 2019, **177**, 501-507.
313. F. Ünlü, A. Kulkarni, K. Lê, C. Bohr, A. Bliesener, S. D. Öz, A. K. Jena, Y. Ando, T. Miyasaka, T. Kirchartz and S. Mathur, *J. Mater. Res.*, 2021, **36**, 1794-1804.
314. F. Bai, Y. Hu, Y. Hu, T. Qiu, X. Miao and S. Zhang, *Sol. Energy Mater. Sol. Cells*, 2018, **184**, 15-21.
315. M. Vigneshwaran, T. Ohta, S. Iikubo, G. Kapil, T. S. Ripolles, Y. Ogomi,

- T. Ma, S. S. Pandey, Q. Shen, T. Toyoda, K. Yoshino, T. Minemoto and S. Hayase, *Chem. Mater.*, 2016, **28**, 6436-6440.
316. J. Li, X. Liu, J. Xu, J. Chen, C. Zhao, M. Salma Maneno, B. Zhang and J. Yao, *Sol. RRL*, 2019, **3**, 1900218.
317. A. K. Jena, A. Kulkarni and T. Miyasaka, *Chem. Rev.*, 2019, **119**, 3036-3103.
318. B. Ghosh, B. Wu, H. K. Mulmudi, C. Guet, K. Weber, T. C. Sum, S. Mhaisalkar and N. Mathews, *ACS Appl. Mater. Interfaces*, 2018, **10**, 35000-35007.
319. B.-W. Park, B. Philippe, X. Zhang, H. Rensmo, G. Boschloo and E. M. J. Johansson, *Adv. Mater.*, 2015, **27**, 6806-6813.
320. A. J. Lehner, D. H. Fabini, H. A. Evans, C.-A. Hébert, S. R. Smock, J. Hu, H. Wang, J. W. Zwanziger, M. L. Chabinyc and R. Seshadri, *Chem. Mater.*, 2015, **27**, 7137-7148.
321. S. Öz, J.-C. Hebig, E. Jung, T. Singh, A. Lepcha, S. Olthof, F. Jan, Y. Gao, R. German and P. H. van Loosdrecht, *Sol. Energy Mater. Sol. Cells*, 2016, **158**, 195-201.
322. X.-G. Zhao, J.-H. Yang, Y. Fu, D. Yang, Q. Xu, L. Yu, S.-H. Wei and L. Zhang, *J. Am. Chem. Soc.*, 2017, **139**, 2630-2638.
323. E. T. McClure, M. R. Ball, W. Windl and P. M. Woodward, *Chem. Mater.*, 2016, **28**, 1348-1354.
324. R. L. Z. Hoye, L. Eyre, F. Wei, F. Brivio, A. Sadhanala, S. Sun, W. Li, K. H. L. Zhang, J. L. Macmanus-Driscoll, P. D. Bristowe, R. H. Friend, A. K. Cheetham and F. Deschler, *Adv. Mater. Interfaces*, 2018, **5**, 1800464.
325. E. Greul, Michiel, A. Binek, P. Docampo and T. Bein, *J. Mater. Chem. A*, 2017, **5**, 19972-19981.
326. M. Wang, P. Zeng, S. Bai, J. Gu, F. Li, Z. Yang and M. Liu, *Sol. RRL*, 2018, **2**, 1800217.
327. F. Igbari, R. Wang, Z.-K. Wang, X.-J. Ma, Q. Wang, K.-L. Wang, Y. Zhang,

- L.-S. Liao and Y. Yang, *Nano Lett.*, 2019, **19**, 2066-2073.
328. B. Wang, L. Yang, C. Dall'Agnese, A. K. Jena, S.-I. Sasaki, T. Miyasaka, H. Tamiaki and X.-F. Wang, *Sol. RRL*, 2020, **4**, 2000166.
329. B. Wang, N. Li, L. Yang, C. Dall'Agnese, A. K. Jena, S.-I. Sasaki, T. Miyasaka, H. Tamiaki and X.-F. Wang, *J. Am. Chem. Soc.*, 2021, **143**, 2207-2211.
330. B. Xiao, Y. Tan, Z. Yi, Y. Luo, Q. Jiang and J. Yang, *ACS Appl. Mater. Interfaces*, 2021, **13**, 37027-37034.
331. W. Gao, C. Ran, J. Xi, B. Jiao, W. Zhang, M. Wu, X. Hou and Z. Wu, *ChemPhysChem*, 2018, **19**, 1696-1700.
332. S. Zhao, K. Yamamoto, S. Iikubo, S. Hayase and T. Ma, *J. Phys. Chem. Solids*, 2018, **117**, 117-121.
333. C. Zhang, L. Gao, S. Teo, Z. Guo, Z. Xu, S. Zhao and T. Ma, *Sustain. Energy Fuels*, 2018, **2**, 2419-2428.
334. M. T. Sirtl, F. Ebadi, B. T. Gorkom, P. Ganswindt, R. A. J. Janssen, T. Bein and W. Tress, *Adv. Opt. Mater.*, 2021, **9**, 2100202.
335. I. Turkevych, S. Kazaoui, E. Ito, T. Urano, K. Yamada, H. Tomiyasu, H. Yamagishi, M. Kondo and S. Aramaki, *ChemSusChem*, 2017, **10**, 3754-3759.
336. A. Kulkarni, F. Ünlü, N. Pant, J. Kaur, C. Bohr, A. K. Jena, S. Öz, M. Yanagida, Y. Shirai, M. Ikegami, K. Miyano, Y. Tachibana, S. Chakraborty, S. Mathur and T. Miyasaka, *Sol. RRL*, 2021, **5**, 2100077.
337. B. Ghosh, B. Wu, X. Guo, P. C. Harikesh, R. A. John, T. Baikie, A. T. Wee, C. Guet, T. C. Sum and S. Mhaisalkar, *Adv. Energy Mater.*, 2018, **8**, 1802051.
338. Y. Kim, Z. Yang, A. Jain, O. Voznyy, G. H. Kim, M. Liu, L. N. Quan, F. P. García de Arquer, R. Comin and J. Z. Fan, *Angew. Chem. Int. Ed.*, 2016, **55**, 9586-9590.
339. M. Khazaee, K. Sardashti, J.-P. Sun, H. Zhou, C. Clegg, I. G. Hill, J. L.

- Jones, D. C. Lupascu and D. B. Mitzi, *Chem. Mater.*, 2018, **30**, 3538-3544.
340. A. Kulkarni, A. K. Jena, M. Ikegami and T. Miyasaka, *Chem. Commun.*, 2019, **55**, 4031-4034.
341. M. Khazaee, K. Sardashti, C.-C. Chung, J.-P. Sun, H. Zhou, E. Bergmann, W. A. Dunlap-Shohl, Q. Han, I. G. Hill, Jacob, D. C. Lupascu and D. B. Mitzi, *J. Mater. Chem. A*, 2019, **7**, 2095-2105.
342. Q. Zhang, C. Wu, X. Qi, F. Lv, Z. Zhang, Y. Liu, S. Wang, B. Qu, Z. Chen and L. Xiao, *ACS Appl. Energy Mater.*, 2019, **2**, 3651-3656.
343. Y. Peng, T. N. Huq, J. Mei, L. Portilla, R. A. Jagt, L. G. Occhipinti, J. L. Macmanus-Driscoll, R. L. Z. Hoye and V. Pecunia, *Adv. Energy Mater.*, 2021, **11**, 2002761.
344. N. Pai, J. Lu, T. R. Gengenbach, A. Seeber, A. S. R. Chesman, L. Jiang, D. C. Senevirathna, P. C. Andrews, U. Bach, Y. B. Cheng and A. N. Simonov, *Adv. Energy Mater.*, 2019, **9**, 1803396.
345. M. Yang, D. H. Kim, T. R. Klein, Z. Li, M. O. Reese, B. J. Tremolet de Villers, J. J. Berry, M. F. Van Hest and K. Zhu, *ACS Energy Lett.*, 2018, **3**, 322-328.
346. N.-G. Park and K. Zhu, *Nat. Rev. Mater.*, 2020, **5**, 333-350.
347. L. Qiu, S. He, L. K. Ono, S. Liu and Y. Qi, *ACS Energy Lett.*, 2019, **4**, 2147-2167.